5-2018

An Investigation of Micro-Surface Shaping on the Piston/Cylinder Interface of Axial Piston Machines

Ashley Busquets
Purdue University

Recommended Citation

Busquets, Ashley, "An Investigation of Micro-Surface Shaping on the Piston/Cylinder Interface of Axial Piston Machines" (2018). *Open Access Dissertations*. 1794.
https://docs.lib.purdue.edu/open_access_dissertations/1794

AN INVESTIGATION OF MICRO-SURFACE SHAPING ON THE PISTON/CYLINDER INTERFACE OF AXIAL PISTON MACHINES

by

Ashley Busquets

A Dissertation

Submitted to the Faculty of Purdue University
In Partial Fulfillment of the Requirements for the degree of

Doctor of Philosophy

School of Agricultural & Biological Engineering
West Lafayette, Indiana
May 2018

THE PURDUE UNIVERSITY GRADUATE SCHOOL
STATEMENT OF COMMITTEE APPROVAL

Dr. Monika Ivantysynova, Chair
    School of Agriculture and Biological Engineering
Dr. Andrea Vacca
    School of Agriculture and Biological Engineering
Dr. Sadegh Dabiri
    School of Mechanical Engineering
Dr. Dennis Buckmaster
    School of Agriculture and Biological Engineering

Approved by:
    Dr. Bernard Engel
        Head of the Graduate Program

To my family

ACKNOWLEDGEMENTS

First, I would like to thank my advisor Dr. Monika Ivantysynova for the chance to pursue my doctorate’s degree and further my knowledge in fluid power here at the Maha Fluid Power Research Center. Under your guidance I was able to challenge myself and achieve goals that may have not been possible elsewhere. I thank you greatly for that.

I must also thank my parents, Kerwin and Penny, along with my husband, Enrique. Without their unconditional support, love, and encouragement to continue on I would never have made it as far as I have and none of this would be possible.

Likewise, I am thankful all of my colleagues which have become friends throughout my studies here at Maha. A special thank you to Dan and Lizhi for their collaboration on the piston/cylinder interface. Thanks to the entire Maha team who have not only helped me over the past years, but have made this experience that much more enjoyable.. I will never forget the experiences and memories made.

Of course, I would also like to thank the staff here at Maha. Connie, thank you for all the help that you have given me when it comes to traveling. To Anthony for all the help in the lab, including the work with the steady state test rig and EHD. Finally, a special thanks to Susan who has helped me so much in not only my professional career but also in some difficult personal times; you are such a beautiful and caring person and I will forever be grateful for you.

TABLE OF CONTENTS

LIST OF TABLES

LIST OF FIGURES

NOMENCLATURE

Symbol	Description	Units
a	Acceleration	[m/s^2]
A	Area	[m^2]
C	Constant	[-]
c_p	Fluid heat capacity	[J/kgK]
d	Diameter	[m]
E	Young's Modulus	[Pa]
E'	Effective stiffness	[Pa]
F	Force	[N]
F_{ak}	Piston axial inertia force	[N]
F_{Ak}	Piston total force	[N]
F_{ck}	Piston correction force	[N]
F_{Dk}	Displacement chamber pressure force	[N]
F_{Sk}	Swash plate reaction force	[N]
F_{TG}	Slipper friction force	[N]
F_{Tk}	Piston viscous friction force	[N]
F_{Sk}	Swash plate reaction force	[N]
$F_{\omega k}$	Piston/slipper centrifugal force	[N]
H_K	Piston stroke	[m]
h	Gap height	[m]
i	Axial index	[-]
$\bar{\imath}$	Unit vector in x direction	[-]
j	Circumferential index	[-]
$\bar{\jmath}$	Unit vector in y direction	[-]
k	Friction coefficient	[-]
l	Length	[m]
m	Mass	[kg]

Symbol	Description	Units
M	Torque	[Nm]
$\boldsymbol{M}$	Columns in fluid film length	[-]
M_{cK}	Piston correction moment	[Nm]
MRC	Minimum radial clearance	[m]
n	Rotational speed	[rpm]
$\bar{n}$	Surface normal unit vector	[-]
$\boldsymbol{N}$	Volumes in fluid film circumference	[-]
p	Pressure	[bar]
P	Power	[W]
Q	Flow rate	[m^3/s]
q_s	Surface thermal flux	[J/m^2]
R	Radius	[m]
s_K	Piston stroke	[m]
s_K	Piston stroke	[m]
T	Temperature	[°C]
t	Time	[s]
u	Fluid velocity	[m/s]
V	Volume	[m^3]
$\boldsymbol{V}$	Fluid velocity vector	[m/s]
v	Velocity	[m/s]
(x,y,z)	Cartesian coordinate system	[-]
$(\hat{x},\hat{y},\hat{z})$	Piston unwrapped Cartesian coordinate system	[m]
$\{e_1,e_2,e_3,e_4\}$	Piston eccentricities	[m]
α	Convection Coefficient	[W/m^2K]
β	Swash plate angle	[°]
λ	Thermal conductivity	[W/mK]
μ	Dynamic viscosity	[Pa s]
ρ	Oil density	[kg/m^3]
σ	Contact stress	[Pa]
τ	Viscous sheer stress	[Pa]

Symbol	Description	Units
Φ_D	Viscous dissipation	[W]
φ	Shaft angular position	[°]
ω	Angular velocity	[rad/s]

LIST OF ABBREVIATIONS

Abbreviation	Description
B	Cylinder block
DC	Displacement chamber
FEM	Finite element method
FSTI	Fluid structure thermal interaction model
G	Slipper
HP	High pressure
IDC	Inner dead center
k	Piston
LP	Low pressure
MRC	Minimum radial clearance
OC	Operating condition
ODC	Outer dead center
RR	Relative rotation of piston
VP	Valve plate
Z	Cylinder bore
Δ	Change or difference

ABSTRACT

Author: Busquets, Ashley. Ph.D.
Institution: Purdue University
Degree Received: May 2018
Title: An Investigation of Micro-Surface Shaping on the Piston/Cylinder Interface of Axial Piston Machines
Committee Chair: Monika Ivantysynova.

Presently, axial piston machines of the swash plate type are commonly used in industry due to their many benefits. However, with recent technological advancements in hydraulic hybrid powertrains and displacement-controlled actuation, the application of such machines has been broadened demanding a more cost-effective reliable and efficient, yet versatile machine. The fluid film geometry of the lubricating interfaces is a very complex and sensitive phenomena that must simultaneously fulfill a competing bearing and sealing function. Therefore, the design process of such machines is a difficult process while tightly constrained manufacturing tolerances are essential thereby increasing the initial production costs. Accordingly, virtual prototyping through analytical simulation in this field has emerged as an ideal tool not only to improve the performance of existing units, but to also design new and innovative axial piston machines that fulfill the demands of advanced technology.

The aim of this dissertation is to investigate more efficient and reliable designs of the piston/cylinder interface of an axial piston machine over a broad range of operating conditions. Primarily, an extensive simulation study was conducted in which the design of a commercially available machine was modified to accommodate piston micro-surface shaping where the relative improvements were then quantified in comparison. This study utilizes a novel fully-coupled fluid structure interaction model considering both thermal and pressure deformations of the solid bodies to accurately predict the dynamic behavior of the lubricating interface. Having analyzed the phenomena of the lubricating gap and the effects of micro-surface shaping, an optimization technique was utilized to design this interface. The optimization scheme determines the best balance between improving the sealing function while maintaining or even improving the bearing function. A surface shaped piston was then measured and compared back to the simulation results realizing the capabilities of such a novel methodology. Ultimately, this cost-effective design process demonstrated that micro-surface shaping is beneficial as it allows for reduced clearances, achieving a reduction in volumetric losses, while increasing fluid film support, resulting in superior efficiency as well as enhanced reliability and overall performance.

CHAPTER 1. INTRODUCTION

Positive displacement machines are often used in a diversity of industrial fields such as aerospace, automotive, agriculture, construction, heavy machinery, robotics, etc. due to their compactness and superior power density. Hydrostatic machines operate converting mechanical to hydraulic energy in pumping mode and hydraulic to mechanical energy in motoring mode. Several basic designs exist that accomplish the displacement principle such as axial piston, gear, vane, and screw types. Specifically, swashplate type axial piston machines are commonly chosen in high pressure applications while capable of maintaining a high overall efficiency and relative ease of control. However, the features and capabilities of these machines are counteracted by the cost of design complexity. Due to the already wide use and broadening necessity of such machines with recent developments in areas such as displacement control, it is essential for the units to be cost-effective and highly efficient. Such improvements require a revolutionary methodology in development: virtual prototyping. This advancement in development could lead to a better understanding of the physical phenomena occurring within the units in turn using this knowledge to design a more efficient and reliable unit in a cost effective and time-saving manner.

1.1 Background

The main contribution of energy dissipation in axial piston machines originates from the rotating group comprised of three main tribological interfaces: the piston/cylinder, the slipper/swash plate, and the cylinder block/valve plate shown in Figure 1.1. These lubricating interfaces are crucial design elements in determining the fundamental performance of the machine over a wide range of operating conditions. Difficulties arise as the thin fluid film of each interface is subject to fulfill simultaneously both a bearing and a sealing function. The lubricating film is paramount to support the dynamic external loads, preventing metal to metal contact between the solid bodies that could lead to wear and eventually failure of the unit. A full film lubrication during operation also generates significantly less viscous friction. In order to have a full film lubrication, the external forces must be equally reacted by the fluid pressure force, entirely supporting the load. This pressure force in the fluid film can develop under two methods: hydrostatic or hydrodynamic. Hydrostatic fluid film pressure is generated as a higher external fluid pressure is transmitted into lubricating gap area. Conversely, hydrodynamic pressure is built up due to the relative motion between two bodies at inclined positions. This same fluid film is also responsible for sealing the high pressure regions becoming subject to leakages. Consequently each interface represents the main source of overall energy dissipation due to the associated leakage flows and viscous friction in which an important balance must be concluded. The lubricating fluid film must be sufficiently large enough to fully support the load preventing contact under full film lubrication in order to minimize the friction forces, while minimal enough to prevent excessive leakage. Considering the long-term and efficient operation of an axial piston machine strongly relies on the behavior of the fluid film, although exceptionally complex, it is crucial to understand leading to improved designs in both performance and reliability.

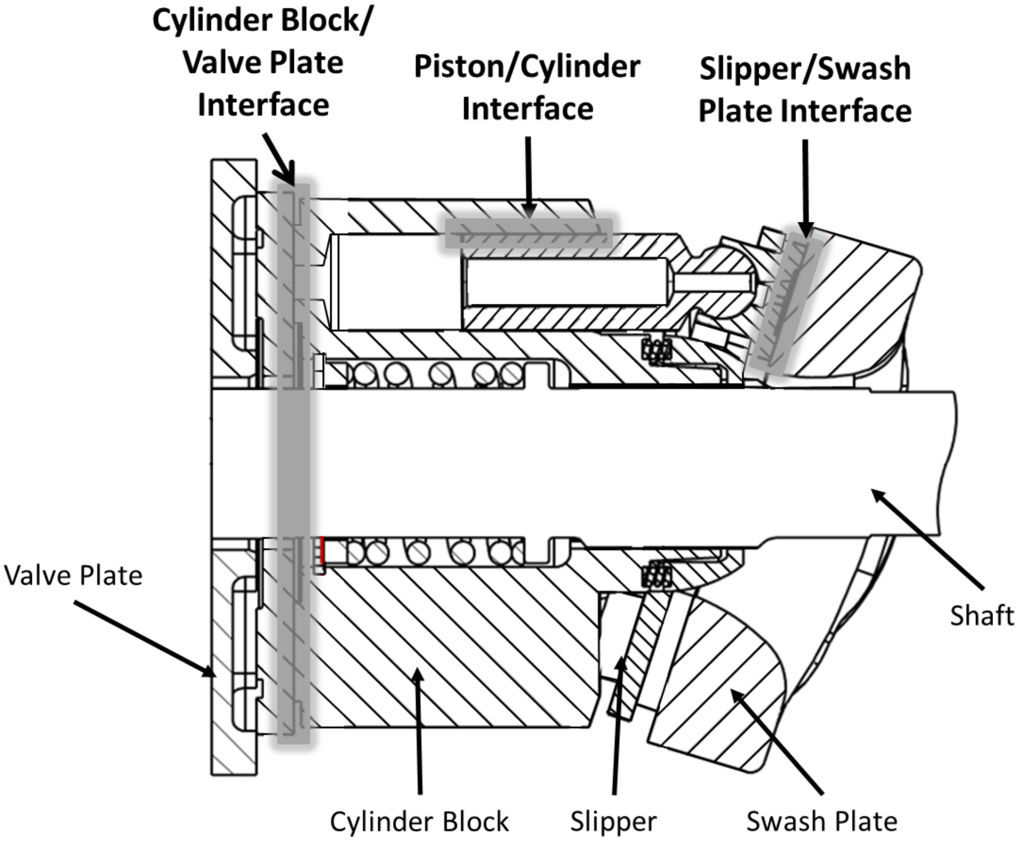

Figure 1.1. Axial piston machine.

1.2 State of the Art

1.2.1 Experimental Research

In order to get a better understanding of the phenomena occurring between the piston and the cylinder, a significant amount of experimental investigation has been conducted by numerous researchers using various simplified versions of the interface over the years. As early as 1972, Van der Kolk constructed a test rig to measure friction forces utilizing a single piston constrained in the axial direction in which an external side force was applied. Later in 1974, Renius took this a step further and built a single piston test rig utilizing inverse kinematics accounting for a more complex motion of the piston including both axial and spin motion measuring the axial and circumferential piston friction forces. Dowd and Barwell (1975) also used a simplified, inverse kinematics test rig to study the effects of material properties and surface roughness on the performance of the interface. Shortly after in 1976, Yamaguchi designed a test rig to study the piston motion and measure the gap heights between the piston and cylinder under low operating pressures. Ivantysynova (1983) later measured the pressure and temperature distribution within the fluid film using a modified swashplate type axial piston machine with inverse kinematics. Following in 1998, Donders again focused on measuring the piston friction forces by attaching a force sensor directly to the piston and using a hydraulic cylinder to apply a side force. Oberem (2002) subsequently used this same test rig to conduct a clearance study on the axial piston friction forces. Shortly after, Ivantysynova and Lasaar (2000) created a test rig that for the first time measured both axial and circumferential friction forces on a swashplate type axial piston machine under conditions comparable to normal operation. This test rig was utilized by Lasaar (2002) to study the impact of piston surface roughness along with a barrel shaped piston. Attention was again aimed back to the measuring the temperature field in 2001 when Olems measured the temperature distribution in the fluid film and in the cylinder block of a stock axial piston machine. Later in 2005, a specialized test rig was utilized to measure the elastohydrodynamic pressure field and temperature field in the gap between the piston and cylinder.

1.2.2 Analytical Models

In many cases, experimental research was conducted in order to advance and validate the development of analytical models. The very first analytical model was developed as early as 1968 which calculated a simple gap flow and friction forces neglecting the hydrodynamic pressure. In conjunction with his experimental work in 1972, Van der Kolk also created a simple analytical model to calculate the pressure field in the gap solving for the Reynolds equation but neglecting any axial piston motion. Although these early models were extremely simplified and provided only general information and basic guidelines in the design process due to the limited computational power, they proved a desire for such tools. To further the analytical study of the piston/cylinder interface, Yamaguchi (1976) investigated piston motion solving for the Reynolds equation considering hydrodynamic lubrication as well as the change in gap height over time due the dynamic pressure in the displacement chamber over a complete shaft revolution. In 1983 and 1985, Ivantysynova progressed a non-isothermal model that not only accounted for the Reynolds equation, but also considered the energy equation as the fluid properties change due to the dynamic temperature and pressure for an assumed piston inclination. Then in 1995 Fang and Shiraskashi for the first time proposed a method to determine the location of the piston based on a force balance between the external and fluid forces neglecting the squeeze effect on the pressure build up. Soon after, Kleist (1995) proposed a similar model in which the effect of piston micro-motion has on the hydrodynamic pressure build up was accounted for. In 2002, Olems combined a non-isothermal model with a Newton Raphson's approach solving for the force balance to determine the micro motion of the piston and the resulting load support. Wieczorek (2002) then integrated this piston/cylinder gap model into a comprehensive simulation model for all three lubricating interfaces. Around this time as well, Ivantysynova and Huang (2002) proposed including an EHL model assuming that pressure peaks in the fluid film could lead to localized elastic deformations in turn leading to a change in the fluid film. Most recently Pelosi (2008, 2011, 2012) presented a novel fully coupled fluid-structure thermal and multi-body dynamics simulation model considering elastic deformations due to both thermal and pressure loading for the piston cylinder interface for axial piston machines. The accuracy of this model was verified through comparison of measurements taken on specialized test rigs measuring the friction forces (Lasaar, 2000), the temperature field (Olems, 2001), and the elastohydrodynamic pressure field (Ivantysynova, Huang, & Behr, 2005) between the piston and the cylinder. The results proved that is it crucial to not only consider the thermal effects in order to correctly estimate the viscosity of the fluid and in turn the load carrying ability, but to also consider the solid body elastic deformations as the deflections could be on the same order of magnitude as the fluid film thickness (Pelosi, 2001, 2012), largely effecting the behavior.

1.2.3 Piston Surface Shaping

Throughout both the experimental and analytical research, it has been demonstrated that altering the shape, configuration, and material of the piston/cylinder interface can be beneficial leading to improved efficiency and load carrying ability. Based on the experimental research of Renius in 1974, it was demonstrated that a barrel-like piston introduces additional hydrodynamic fluid film support. Similarly, the analytical investigation performed by Yamaguchi (1976) concluded that micro-surface shaping of the piston is beneficial to the load carrying capacity of the fluid film. Following in 1983, Ivantysynova proposed a barrel-like piston with a large curvature radius resulting in a diameter reduction at both ends. Later in 1997, Kleist concluded through a simulation study, that different shaped pistons resulted in lower friction and comparable leakage to a common, cylindrical piston. Further studying the proposal of Ivantysynova, Lasaar (2003) detailed a barrel-like shaped piston, shown in Figure 1.2, resulting in a minimized overall energy dissipation of up to 20% analytically, later measuring a reduction in friction forces experimentally. As surface shaping of the piston showed promising improvements, Ivantysynova and Garrett (2009) studied and filed a patent for a sine waved (Figure 1.3) piston simulating up to a 60% decrease in total power loss. Based on these designs, Ivantysynova and Fredrickson (2008) studied a combined sine waved barrel micro-surface piston shape that demonstrated results similar to that of the barrel-like design. Most recently, Gels and Murrenhoff (2010) researched a contoured piston with a varying gap height and guide length in order to reduce the losses of the piston/cylinder interface. Throughout the studies presented on surface shaping of the piston/cylinder interface it was found that the performance is strongly dependent on the operating conditions under which it is tested.

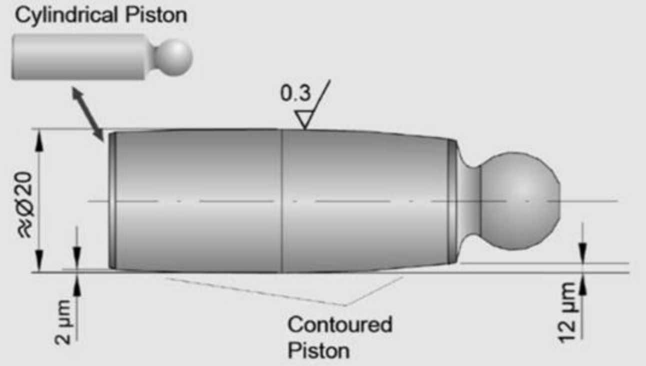

Figure 1.2. Barrel like piston surface shape (Lasaar, 2003).

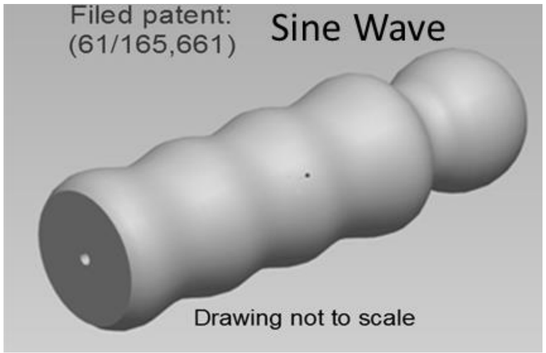

Figure 1.3. Sine wave piston surface shape (Garrett, 2009).

1.3 Research Aims and Objectives

The motivation behind this research was driven by the promising results of the previous research on surface shaping of the piston along with the advances in the numerical model for the piston/cylinder interface. The aim was to not only reach a better understanding of the physical phenomena occurring in the fluid film of the lubricating gap, but furthermore comprehensively investigate the effects of micro-surface shaping on the piston through virtual prototyping utilizing the novel fluid structure interaction model developed by Pelosi (2012) over a wider range of operating conditions.

Consequently, the main goal of this research was to investigate how to reduce energy dissipation and increase load carrying capacity in an axial piston machine between the piston and the cylinder through surface shaping of the piston. The more specific goal was to understand the effects of the design principles on the lubricating film and not only the impact on the efficiency of the unit, but also the load carrying ability as well as the performance and reliability. This was conducted through a thorough simulation study ultimately utilizing optimization schemes to conclude designs in which to manufacture and experimentally validate. Virtual prototyping is proved to be significantly cost effective and less time consuming as opposed to the traditional physical experimental prototype testing. Furthermore, the design trends established in this work will be useful for future design of this lubricating interface.

CHAPTER 2. THE PISTON / CYLINDER INTERFACE

The piston/cylinder interface represents a key design element contributing to the overall performance an axial piston machine. More specifically, the lubricating film can strongly influence the effective and efficient operation while fulfilling the function of transferring forces to cylinder block.

2.1 Axial Piston Machine Kinematics

In regards to studying and understanding the behavior of the piston/cylinder interface of a swashplate type variable displacement axial piston machine, it is fundamental to characterize correctly the kinematics of the entire unit defining the macro motion of the piston.

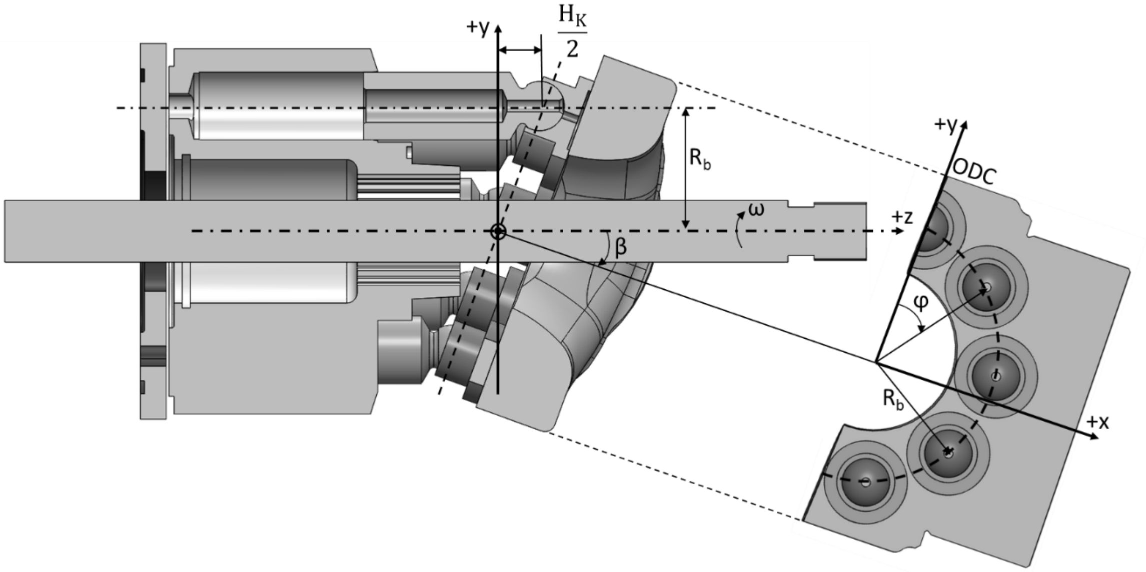

Figure 2.1. Axial piston machine and reference system.

The primary element of an axial piston machine is the rotating group of which the main components as well as the assigned, corresponding global reference system are illustrated in Figure

2.1. The rotating kit is comprised of a cylinder block coupled to the rotating shaft via a mechanical spline. The cylinder block rotates with the shaft relative to a stationary valve plate opening the displacement chamber (DC) kidneys to the high and low pressure ports. The piston/slipper assemblies rotate along the pitch diameter centered at the shaft axis with the slippers pressed to a stationary swashplate. An inclination of the swashplate causes an axially reciprocating motion of each piston within their corresponding bores. The stroke of each piston depends on inclination angle of the swashplate, β, as well as the pitch radius of the block, R_b, which they rotate along (Ivantysyn and Ivantysynova, 2001):

$$H_k = 2R_b \tan\beta. \tag{2.1}$$

As such, a larger swashplate angle corresponds to a larger stroke of the piston and therefore a higher displacement. The instantaneous position of the piston during the stroke is defined along the z-axis as:

$$s_k = -z. \tag{2.2}$$

Where according to Figure 2.1 it follows that

$$z = (R_b - y)\tan\beta \quad \text{and} \tag{2.3}$$

$$y = R_b \cos\varphi. \tag{2.4}$$

Therefore the instantaneous piston position is not only dependent on the swashplate angle, but also the angular position of the piston, φ:

$$s_k = -R_b \tan\beta\,(1 - \cos\varphi). \tag{2.5}$$

Based on this motion of the piston, the piston velocity and acceleration can be calculated as:

$$v_k = \frac{ds_k}{d\phi}\omega = -\frac{1}{2}\omega H_k \sin\varphi, \tag{2.6}$$

$$a_k = \frac{dv_k}{d\phi}\omega = -\frac{1}{2}\omega^2 H_k \cos\varphi. \tag{2.7}$$

Radial relative motion occurs as well between the piston and the cylinder under the assumption that the ball joint connection between the piston and the slipper is rigid resulting in piston circumferential velocity and radial acceleration:

$$v_u = R\omega \tag{2.8}$$

$$a_u = R\omega^2 \tag{2.9}$$

Due to the velocity, v_k, and size of the piston, A_k, the fluid volume in the displacement chamber changes over a revolution

$$\frac{dV_i}{dt} = v_k A_k = -\frac{1}{2}\omega H_k \sin\varphi\, A_k \tag{2.10}$$

Where the instantaneous volume is defined based on the initial volume with the piston at ODC, V_0, as well as the area, A_k, and location, s_k, of the piston:

$$V_i = V_0 - V = V_0 - s_k A_k = V_0 + R_b \tan\beta\,(1-\cos\varphi)A_k \tag{2.11}$$

An axial piston machine is capable of operating in either pumping or motoring mode. In pumping mode, mechanical power is converted into fluid power as the axial motion of the piston causes fluid to be drawn in at a low pressure from the inlet and discharged at a high pressure to the outlet port. In the suction stroke, the piston starts at inner dead center (IDC) and moves out of the bore increasing the volume. Subsequently, during the discharge stroke, the piston is now at outer dead center (ODC) and begins to move back into the bore, decreasing the volume. On the contrary, in motoring mode, fluid power is converted into mechanical power as high pressure fluid enters through the inlet consequently generating high forces on each piston leading to available torque on the shaft.

2.2 Dynamic Loading Conditions of the Piston

Considering the kinematics and geometry of an axial piston machine, the piston is loaded with various external forces. These forces are imperative to define correctly in order to gain a better understanding of the challenges that the lubricating film between the piston and the cylinder presents.

Since the pistons rotate around the shaft with the cylinder block it is first necessary to define a separate coordinate system for the piston/cylinder interface that rotates along with it on which the forces interact with the piston. A Cartesian coordinate system (x_k, y_k, z_k) is chosen such that the positive x_k-axis points in the direction of rotation, perpendicular to the y_k-axis that is defined as pointing outward in the radial direction in which the z_k-axis always lies on the center axis of the cylinder bore toward the case. The origin of this coordinate systems lies on the DC end of the gap between the piston and cylinder, the beginning of the fluid film interface. In the case of a variable gap length in which the piston end enters the bore, the origin will shift with respect to the piston positing within the bore. The external forces acting on the piston in respect to these coordinates can be seen in Figure 2.2.

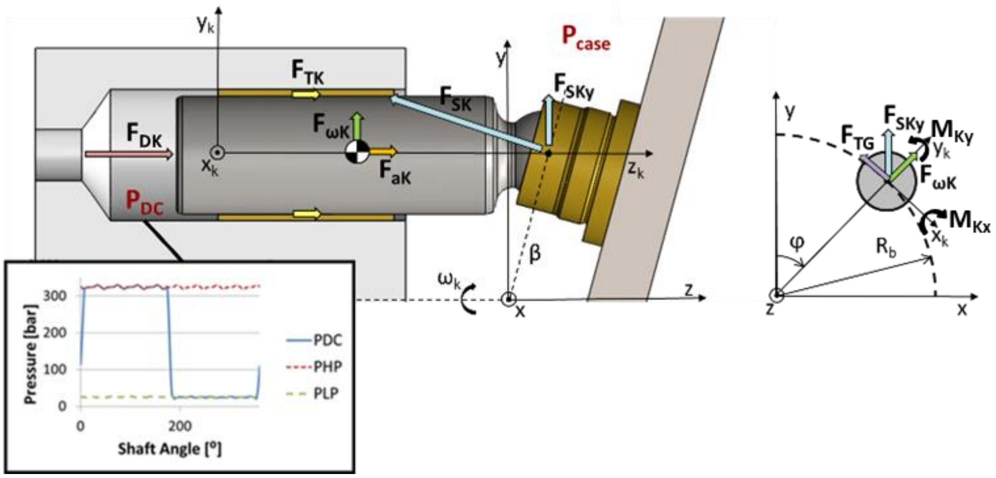

Figure 2.2. Forces acting on the piston/cylinder interface.

One of the major forces acting axially on the piston, dependent on the operating condition, is the pressure force from the displacement chamber pressure, F_{Dk}:

$$F_{DK} = \frac{\pi d_k^2}{4}(p_{DC} - p_{Case}). \tag{2.12}$$

Due to the acceleration of the mass of the piston in the axial direction, there is also a piston inertial force, F_{ak}, to take into consideration:

$$F_{ak} = -m_k a_k = m_k \omega^2 R_b \tan\beta \cos\varphi. \tag{2.13}$$

Additionally, as the piston reciprocates within the bore through a fluid, a viscous friction force, F_{Tk}, is generated in the axial direction:

$$F_{Tk}(\varphi) = \int_A \tau(\varphi) dA. \tag{2.14}$$

The comprehensive external forces loading the piston in the axial direction, F_{Ak}, becomes the sum of these three forces:

$$F_{Ak} = F_{DK} + F_{ak} + F_{Tk}. \tag{2.15}$$

This comprehensive force is transferred through the body of the piston and attached slipper in which it is reacted by the swashplate perpendicularly, F_{Sk}:

$$F_{Sk} = -\frac{F_{Ak}}{\cos\beta} \tag{2.16}$$

Since the swashplate is inclined, this force induces a side load on the piston, F_{Sky}:

$$F_{SK_y} = F_{Ak}\tan\beta. \tag{2.17}$$

Also acting in the circumferential direction, adding to the side load exerted on the piston, is a centrifugal force, $F_{\omega k}$, introduced as the mass of the piston/slipper assembly rotates around the shaft with the block:

$$F_{\omega k} = (m_k + m_G)\omega^2 R_b. \tag{2.18}$$

Although a minor circumferential external force acting on the piston, the viscous friction force between the slipper and the swash plate, F_{TG}, is also to be considered:

$$F_{TG} = \mu\frac{\omega R_b}{h_G}\left[\frac{\pi}{4}\left(d_{Gout}^2 - d_{Gin}^2\right)\right]. \tag{2.19}$$

In the case that the piston/cylinder interface is numerically analyzed coupled with the slipper/swashplate interface, the estimated film thickness between the slipper and swashplate is used to accurately calculate this viscous friction force. Often times though this is not the case and the piston/slipper interface is analyzed independently in which a simplified parallel gap assumption is made to predict a constant fluid film thickness in order to calculate the viscous friction force between the slipper and the swashplate that is transferred as an external force to the piston.

By summing the external forces acting on the piston/cylinder interface, the overall forces can be reduced to:

$$F_{Kx} = -F_{sKy} \sin \varphi + F_{TG} \tag{2.20}$$

$$F_{Ky} = F_{sKy} \cos \varphi + F_{\omega K}$$

With external moments of:

$$M_{Kx} = -z_{RK} F_{sKy} \cos \varphi - (z_{RK} - l_{SK}) F_{\omega K} \tag{2.21}$$

$$M_{Ky} = z_{RK} F_{Kx}$$

Under the assumption of full film lubrication, these external forces and moments acting on the piston are balanced hydrodynamically by the pressure field built up in the fluid film between the piston and cylinder.

2.3 Function of the Piston / Cylinder Interface

The primary role of the piston/cylinder interface is to bear the load from external forces through the pressure field in the fluid film, ideally under full film lubrication minimizing the viscous friction forces. Different from the cylinder block/valve plate and slipper/swashplate interfaces, the piston must be balanced hydrodynamically rather than hydrostatically. The hydrodynamic fluid support is built up due to various phenomena that occurs concerning the piston/cylinder interface. A main contribution is from the sliding and rotational macro motion as well as micro motion of the inclined piston in relation to the stationary bore creating a squeeze effect. The deformations of the solid bodies due to the localized pressure spikes in the fluid film also play a role. Furthermore, the heat generated from the energy dissipation in the gap creates a temperature distribution that not only has an effect on the fluid properties, but also results in an additional deformation of the solid bodies due to the subjected internal thermal stresses. However, the piston must also seal the pressurized fluid in the displacement chamber through a thin film reducing leakage losses.

The overall performance of the interface is ultimately dependent on the dynamic geometry of the lubricating fluid film, changing as the loading on the piston oscillates due to the pressure in the displacement chamber over a single revolution as shown in Figure 2.3. Conclusively, the same fluid film that must bear the external loads exerted on the piston, also produces the main source of energy dissipation, from both volumetric and mechanical losses. Consequently, the design of the interface does not only effect the performance of the interface, but it can also greatly alter the efficiency in which a compromise between the competing functions must be found.

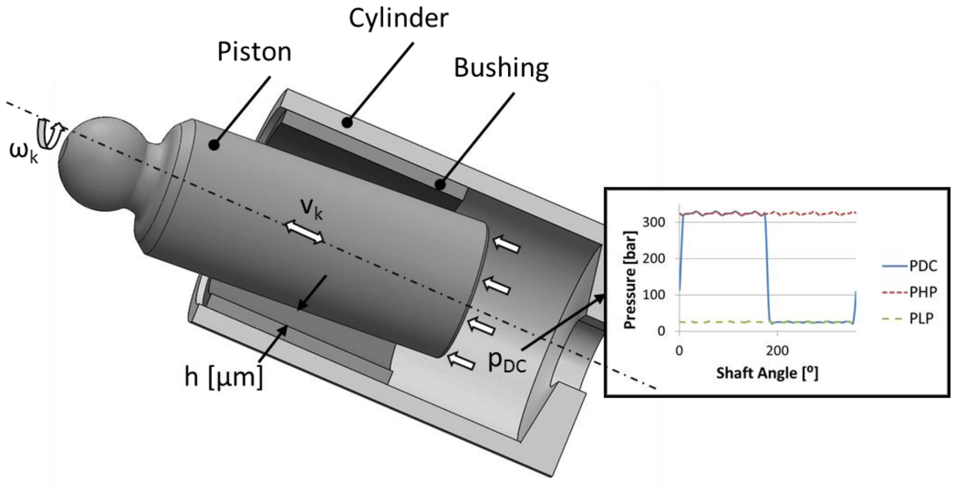

Figure 2.3. Piston/Cylinder showing DC pressure change.

2.4 Fluid Film Geometry of the Piston/Cylinder Interface

In order to gain a better understanding of the phenomena occurring within the gap between the moving piston and the cylinder bore, it is crucial to examine the fluid film geometry as a result of the position of the piston throughout an entire revolution based on the dynamic forces and machine kinematics. As developed by Wieczorek and Ivantysynova (2002) an eccentric position $\{e_1,e_2,e_3,e_4\}$, of the piston within bore, shown in Figure 2.4, is defined. The location of the piston with respect to the piston Cartesian coordinate system becomes:

$$x_m(z_k) = \frac{e_3 - e_1}{l_F} z_k + e_1 \text{ and} \tag{2.22}$$

$$y_m(z_k) = \frac{e_4 - e_2}{l_F} z_k + e_2. \tag{2.23}$$

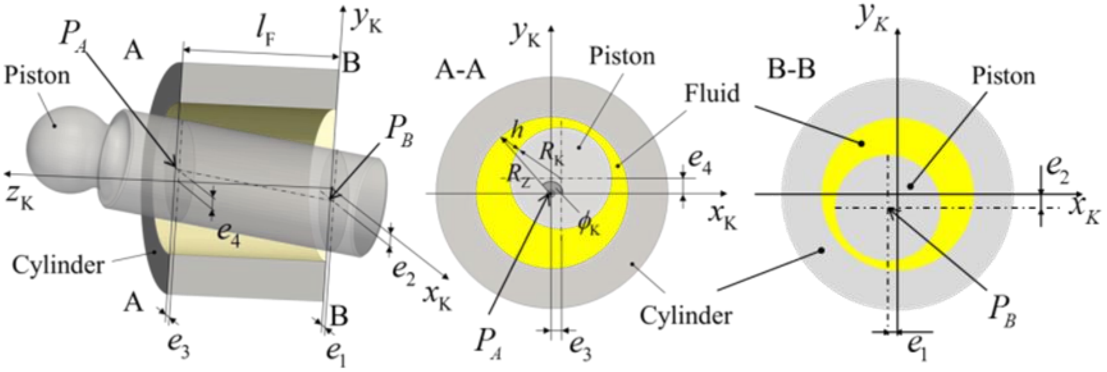

Figure 2.4. Eccentric position of the piston in the cylinder bore (Pelosi, 2012).

As a result of the position of the piston within the bore, the fluid film geometry separating the solid bodies, h, can be defined at any shaft position as:

$$h(z_k, \varphi_k) = \sqrt{\left(R_Z \cos\varphi_k - x_m(z_k)\right)^2 + \left(R_Z \sin\varphi_k - y_m(z_k)\right)^2} - R_k + \Delta h. \tag{2.24}$$

The effect of the surface elastic deformations of the piston and the cylinder due to pressure and thermal effects are captured in the Δh term.

Another distinct Cartesian coordinate system is introduced to define fluid film thickness for the gap of the piston/cylinder interface:

Piston Circumference ($2\pi R_k$): $\hat{x} = \varphi_k R_k$ (2.25)

Gap length (l_F): $\hat{y} = z_k$ (2.26)

Fluid film thickness: $\hat{z} = h(\varphi_k, z_k)$ (2.27)

Based on this coordinate system, the fluid film can be unwrapped and viewed at a single shaft position as a surface with a varying fluid film thickness over the length and circumference of the gap. Figure 2.5 shows a typical unwrapped fluid film geometry on the right based on the depicted piston position on the left.

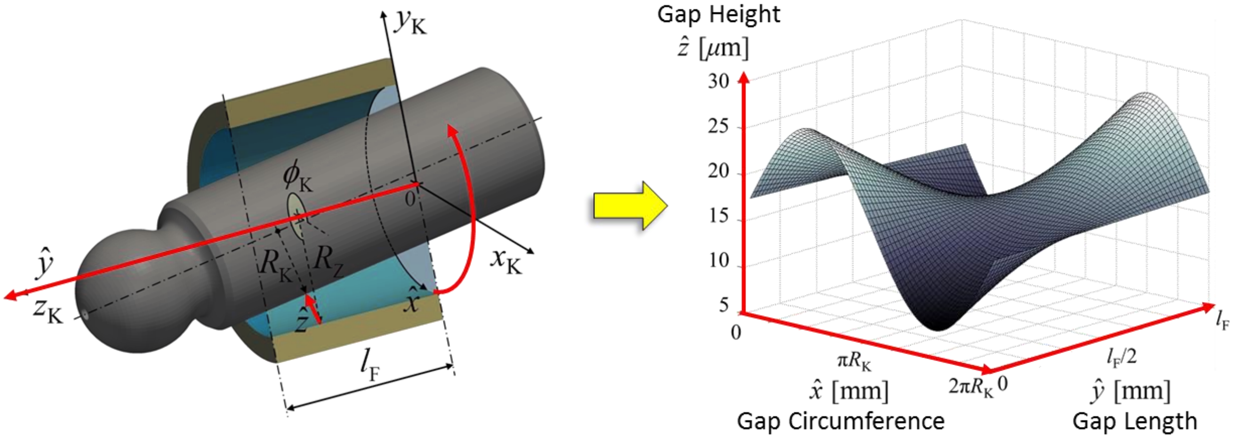

Figure 2.5. Unwrapped fluid film geometry (Pelosi, 2012).

CHAPTER 3. FLUID STRUCTURE THERMAL INTERACTION MODEL OF THE PISTON/CYLINDER INTERFACE

3.1 Overview of the Numerical Model

Advancements in numerical modeling and computer speed has realized the possibility of the virtual prototyping as a method of axial piston machine design. This research is specifically focused on improving unit reliability, performance, and efficiency at the piston/cylinder interface utilizing a novel fluid structure thermal interaction model considering the physical phenomena occurring in the fluid film gap as proposed by Pelosi (2012). The non-isothermal fluid film is calculated using the Reynolds and energy equation as a basis for the model encompassing the dynamic fluid-structure interaction problem as the pressure and temperature field within the fluid changes over each shaft revolution.

3.1.1 Reynolds Equation

In order to capture a more accurate portrayal of the complex fluid film dynamics a more complete version of Reynolds equation specific to the piston/cylinder interface must be considered. Simplified models can compromise the validity of the results by predicting inaccurate fluid film geometry. In 2009 Ivantysynova and Pelosi proposed a numerical model with a comprehensive Reynolds equation particular to the piston/cylinder interface. The equation is derived from the Navier-Stokes, expressing the fluid velocity in the gap that is then applied into the continuity equation and integrated over the fluid film thickness. Assuming steady state, negligible inertial forces, and a uniform pressure through the thickness of the fluid film for the Navier-Stokes equation in a Cartesian coordinate system, the fluid velocities between the piston and cylinder become:

$$\begin{cases} u = \frac{1}{2\mu}\frac{\partial p}{\partial x}(z^2 + zh + h_t h_b) + z\frac{u_t - u_b}{h} + \frac{u_b h_t - u_t h_b}{h} \\ v = \frac{1}{2\mu}\frac{\partial p}{\partial y}(z^2 + zh + h_t h_b) + z\frac{v_t - v_b}{h} + \frac{v_b h_t - v_t h_b}{h} \end{cases} \quad (3.1)$$

Accounting for the relative inclination between the two surfaces through the distances from the top surface signifying the cylinder, and bottom surface, the piston, to the reference plane, h_t and h_b respectively as shown in Figure 3.1. Similarly, the velocities of the surfaces in both the circumferential, v_t and v_b, and axial direction, u_t and u_b are also accounted for. The Poiseuille component of the velocity is relative to the pressure gradient across length of fluid film creating fluid flow while the Couette component is relative to the circumferential and axial motion of piston resulting in fluid drag. The fluid flow is continuously changing over a revolution as the piston position adjusts due to the variable external loads.

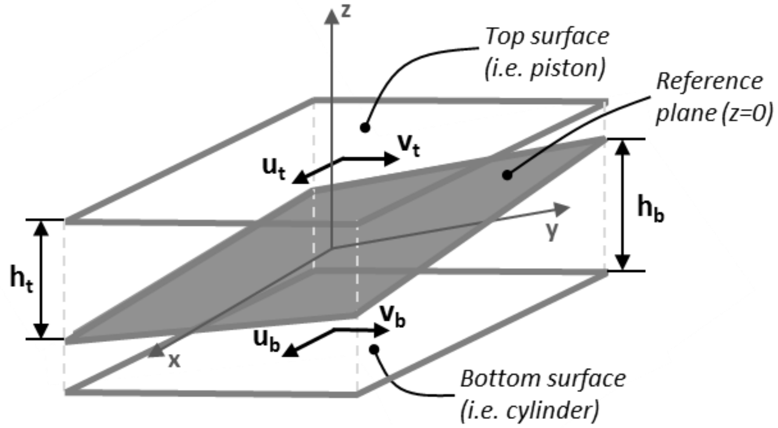

Figure 3.1. Surfaces relative to reference plane (gray).

These velocities are substitute into the incompressible equation and integrated over the fluid film in which the distinct Reynolds equation becomes:

$$\frac{\partial}{\partial \hat{x}}\left(h^3 \frac{\partial p}{\partial \hat{x}}\right) + \frac{\partial}{\partial \hat{x}}\left(h^3 \frac{\partial p}{\partial \hat{x}}\right) + \frac{\partial}{\partial \hat{y}}\left(h^3 \frac{\partial p}{\partial \hat{y}}\right) + 6\mu \left[\hat{u}_k \left(2 \frac{\partial |h_b|}{\partial \hat{x}} - \frac{\partial h}{\partial \hat{x}}\right) + \hat{v}_k \left(2 \frac{\partial |h_b|}{\partial \hat{y}} - \frac{\partial h}{\partial \hat{y}}\right) + 2 \frac{\partial h}{\partial t}\right] = 0. \tag{3.2}$$

This is under the assumption that the piston moves relative to a fixed cylinder bore at a calculated speed. Note that the updates were made such that the squeezing source terms are captured by comparing the gap height at the current time step to the gap height at the previous time step:

$$b = \left(-speed_k \cdot \omega r_k \frac{\rho_e h_e - \rho_w h_w}{dx} - \vartheta_k \cdot \frac{\rho_n h_n - \rho_s h_s}{dy} + 2\left(\rho_p \frac{h(i)_{curr} - h(i)_{pre}}{dt} + h_p \cdot expansion\right)\right) \mathrm{dxdy}. \tag{3.3}$$

As opposed to simply setting the squeeze term to zero at the minimum gap height which resulted in instabilities. More details about this update can be found in Shang, 2018.

This version of the Reynolds equation is more encompassing as it integrates crucial aspects effecting the fluid film geometry. An important aspect considered is the effect on the geometry of the fluid film due to the solid body deformations. Considering that the solid body surfaces defining the tribological interface are subject to concentrated high fluid film pressures and temperature gradients causing internal stresses, the resulting deviation of the surface can be on the same order of magnitude as the fluid film thickness, having a detrimental impact. The ability to introduce a surface shape on either of the solid body surfaces is also included. This surface shaping can either be wear profiles due to normal operation of an existing machine allowing for a more accurate prediction, or advanced intentional designs in order to improve performance. Finally, this version is also capable of predicting crucially low areas of fluid film thickness, not allowing for penetration in which the pressure is saturated to zero in order to ensure flow continuity.

3.1.2 Energy Equation

The temperature distribution within the fluid film not only effects the fluid properties, but the solid body surface deflections as well; both of which effect the overall behavior of the piston/cylinder interface. Under such circumstance, it is essential that the energy equation be used to predict this temperature distribution within the fluid film. The energy equation is expressed as (Shang, 2017):

$$hm = h_0 m_0 + (\frac{dh}{dt} m_0 + h_{in}\dot{m_{in}} - h_{out}\dot{m_{out}} + \mu \Phi_D dV + \sum_i \lambda_i (\nabla T)_i A_i)dt. \tag{3.4}$$

In which the total enthalpy of the control volume at the current time step is equal to the total enthalpy at the previous time step, the enthalpy change with the incoming and outgoing flow of mass, heat generation by the viscous shear of the lubricating fluid film, Φ_D, and the conduction occurring on each face of the three-dimensional finite volume. The specific enthalpy is a function of pressure and temperature:

$$h = h_0(T_0) + \int_{T_0}^{T} c_{p_0}\, dT + \int_{p_0}^{p} T \left(\frac{\partial v}{\partial T}\right) dp + \int_{p_0}^{p} v dp \tag{3.5}$$

This temperature distribution in the fluid film can then be used to calculate the heat flux to the solid bodies by solving a heat transfer problem giving accurate surface temperatures. Note that the heat flux is calculated using an advanced heat transfer model in which the temperature distribution is solved using a dual-body integrated linear system as opposed to solving the solid bodies separately (Shang, 2018). The solid body surface temperatures are then used as boundary condition to the fluid flow as well as for calculating the thermal strain leading to solid body deformation.

3.1.3 Energy Dissipation and Leakage

Once the behavior of the fluid film is predicted, the non-isothermal fluid flow model can be used to accurately predict the losses of the fluid film of the piston/cylinder interface in order to reach an enhanced understanding of design improvements for reliability and efficiency. The overall energy dissipation of the piston/cylinder interface is comprised of two main contributions, mechanical (torque) and volumetric (leakage) losses. The mechanical losses resulting from the shear stresses exerted on the fluid due to the circumferential and axial motion of the piston generates a viscous friction. This viscous friction can be calculated by integrating the shear stresses, τ, over the surface areas, A:

$$F_T(\varphi) = \int_A \tau(\varphi) dA. \tag{3.6}$$

Volumetric losses also occur as the fluid leaks to the case from the pressurized displacement chamber on the other end of the length of the gap. This leakage can be calculated by integrating the axial velocity distribution, $\hat{v}$, over the gap area, $(\hat{x},\hat{z})$:

$$Q_{sk}(\varphi) = \int_0^{2\pi R_k} \int_0^h \hat{v}(\varphi) d\hat{z} d\hat{x}. \tag{3.7}$$

Both the viscous friction and leakage varies over one shaft revolution, and are accordingly a function of the shaft angle, φ, due to the dynamic loading of the interface along with the machine kinematics.

Due to the viscous flow in the lubricating gap between the piston and the cylinder, heat is generated by the viscous shearing of the fluid. This heat generated is expressed as the total energy dissipated, Φ_D, calculated based on the power per unit dissipated:

$$\Phi_D = \left(\frac{\partial \hat{u}}{\partial \hat{z}}\right)^2 + \left(\frac{\partial \hat{v}}{\partial \hat{z}}\right)^2. \tag{3.8}$$

3.2 Fluid Structure Thermal Interaction Model

Pelosi (2012) presented an innovative, fully coupled fluid-structure thermal and multi-body dynamics simulation model considering elastic deformations due to both thermal and pressure loading. This model adopts the Reynolds and energy equation as a basis for predicting the fluid film behavior by solving for the motion of the piston within the cylinder bore based on the balance between the external and fluid forces while coupling the thermal and elasto-hydrodynamic effects. In order to achieve an accurate prediction of the behavior of the fluid film, the model captures the macro and micro motion of the piston within the stationary cylinder bore, the effects of the fluid and material properties, the heat transfer between the fluid film and solid bodies, and most recently, the detrimental change in the geometry of the fluid film due to surface shaping and thermal and pressure deformations of the piston and cylinder surfaces. This advanced, physics-based model will be utilized in the following piston/cylinder interface extensive virtual research study.

This model is comprised of three main, co-dependent modules as indicated in model overview shown in Figure 3.2: the fluid film finite volume non-isothermal flow module, the solids finite volume heat transfer module, and the solids finite element elastic deformation module.

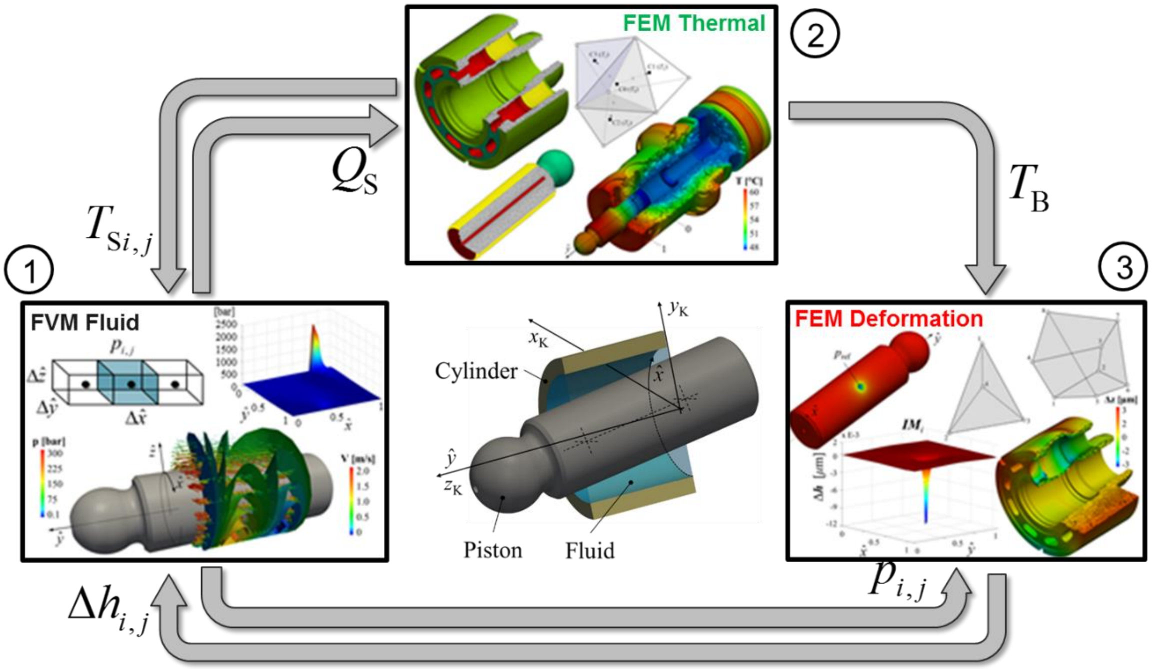

Figure 3.2. Fluid structure thermal interaction model (Pelosi, 2012).

The fluid film module, 1, is governed by the fundamental Reynolds and energy equations which are solved simultaneously through a finite volume method. A fluid structure interaction analysis is necessary at this point due to the nonlinearities of the fluid film geometry introduced by the pressure deformations. Furthermore, the effect that the dynamic pressure and temperature fields within the lubricating gap have on the fluid properties are considered in the resulting fluid film of this module. The calculated resulting surface heat flux, Q_s, are then transferred to the thermal model.

The heat transfer module, 2, utilizes the heat fluxes from the viscous dissipation of the fluid film to predict the temperature distribution, T_B, on the solid parts via a finite volume method. This temperature distribution is then used as the boundary conditions to the fluid film as well as to calculate the thermal stress conditions on the solid bodies. The calculated surface temperatures, T_s, are transferred back to the fluid model as they directly influence the fluid properties of the energy equation.

Utilizing the predicted pressure field, p, as well as the solid body temperature distribution, T_B, resulting from the fluid film and thermal modules respectively, a third module solves for the elastic deformations through a finite element method. The elastic deformations due to external pressure loading are solved every time step due to the direct effect on the dynamic pressure field. In the interest of time, the pressure deformations are solved using an influence method with offline FEM analysis. Conversely, the deformations due to internal thermal loading are solved once per revolution in which an online FEM analysis can be used in a timely manner. The resulting change in the fluid film geometry are directed back to be considered by the fluid film module. An iterative process between the three main modules is required for convergence of the results as each interacting module has an influence on the outcome of the others.

In the interest of time, the model predicts the fluid film behavior for a single reference piston and cylinder segment. Nevertheless, the entire block is analyzed in the case that the pressure and thermal loading on neighboring bores effects the reference bore. Due to the dynamic loading conditions over a complete shaft revolution, the fluid film is solved for at discrete time steps.

CHAPTER 4. NOVEL PISTON DESIGNS

Five diverse piston micro-surface shapes were extensively investigated in order to obtain a deep understanding of surface shaping and the impacts on the resulting fluid film geometry as a method of improving axial piston machine performance and increasing efficiency. Four of the micro-surface shapes include a sinusoidal wave and a flat sinusoidal wave along with a barrel and a combination of the sinusoidal wave and barrel all applied along the axial surface of the piston. Aside from the axial designs, a fifth micro-surface shape, a sinusoidal wave along the circumference of the piston, is additionally included in the study. The following sections of this chapter will detail the design parameters considered for the geometry of each of these designs; including specific normalized values concluded from a parameter study previously conducted (Wondergem, 2014). Each surface shape was implemented on the surface of a baseline, cylindrical design with the fundamental dimensions as shown in Figure 4.1.

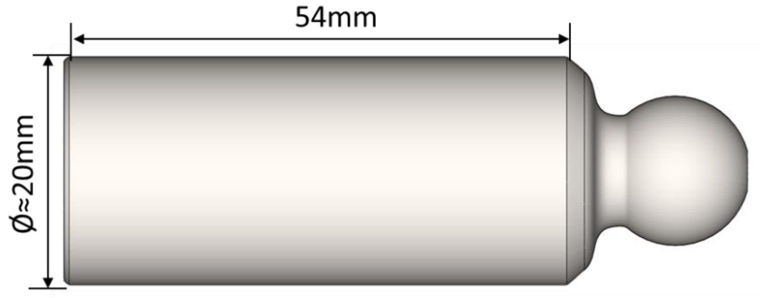

Figure 4.1. Reference cylindrical piston design.

4.1 Sinusoidal Wave Surface Profile (Sine Wave)

A sinusoidal wave along the axial length of the piston, Figure 4.2, was studied as an alternate micro-surface design as comparison to a base cylindrical design.

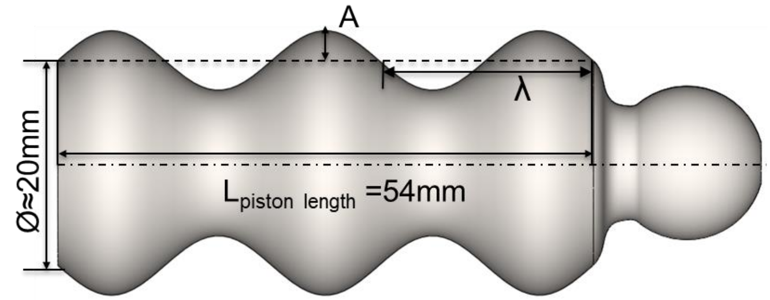

Figure 4.2. Sinusoidal wave piston surface profile.

A sinusoidal wave is a mathematical curve describing a periodic, repetitive oscillation in the form of:

$$y = A \cdot sin(\frac{2\pi}{\lambda}x) \tag{4.1}$$

The design parameters that define the sinusoidal curve consists of the amplitude, A, and the wavelength, λ.

1. The amplitude is the maximum deviation from equilibrium; in this case the equilibrium being the original cylindrical surface of the piston, R_K. The selected amplitude normalized to the radius of the piston for the following study is:

$$\frac{A\ [\mu m]}{R_K\ [mm]} = 0.29‰ \tag{4.2}$$

2. The wavelength of a sinusoidal wave is the period or in other words the length before the wave starts to repeat itself; specifically this parameter follows as:

$$\lambda_N = \frac{\lambda\ [mm]}{L_{piston\ length}\ [mm]} = 0.4 \tag{4.3}$$

From a different perspective, the number of waves can be expressed as the number of occurrences of a repeating wave. One wave is measured between every three consecutive equilibrium crossing, including one crest and one trough.

$$N = \frac{L_{piston\ lengh}\ [mm]}{\lambda[mm]} = 2.5 \tag{4.4}$$

It is important to note that the number of waves must be constrained to a half wave. This means that the sine wave must start from the equilibrium into a peak on both ends, a downward slope resulting, in order to avoid detrimental point contact at the ends of the gap as the piston tilts within bore. This condition was concluded from a previous research study.

4.2 Flat Sinusoidal Wave Surface Profile (Flat)

A flat sinusoidal wave, Figure 4.3, was also proposed in which the DC and case ends of the piston both have the slope of an amplitude of a sinusoidal wave while the peak to peak length remains a flat cylinder. The concept of this design is to study how the waves along the gap surface of the sinusoidal design effects the generation of fluid support as well as in a sense, represent a pre-manufactured wear profile as the wear tends to occur at the ends of the piston.

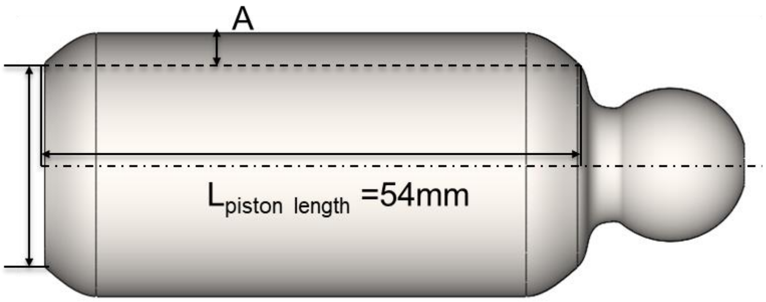

Figure 4.3. Flat sinusoidal wave piston surface profile.

The single design parameter defining geometry of the flat sinusoidal wave micro-surface shape is the amplitude.

1. The amplitude for this design remains the same as that described for the sinusoidal wave in section 4.1:

$$A_N = \frac{A\ [\mu m]}{R_K\ [mm]} = 0.29‰ \tag{4.5}$$

4.3 Barrel Surface Profile (Barrel)

A barrel micro-surface profile, Figure 4.4, along the axial length of the piston was also considered throughout the following research study as it previously had shown promising results (Lasaar, 2003) although studied with an incomplete model at relatively moderate operating conditions.

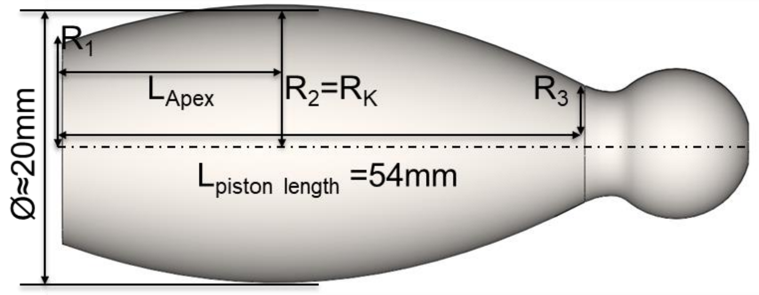

Figure 4.4. Barrel piston surface profile.

A barrel design is a cylindrical shape with a convex, outward bulge along the length. For the barrel design considered in this study, it is not necessary for the apex of the bulge to be centered resulting in different radii on the DC and case end. Therefore, the design parameters used to define such a design include the location and radius of the apex along with the radii at both the DC and case ends.

1. The apex is the highest point or peak along the length of the barrel. The radius at this point is the distance from the centerline of the original cylindrical piston, z_k-axis, to the peak. For simplicity, the apex of the barrel remains at the original radius of piston in which material would be removed from ends in order to introduce the barrel design:

$$R_2 [mm] = R_K \, [mm] \tag{4.6}$$

2. The location of the apex is defined by the length between the apex and the DC end of the piston. From the parameter study, it follows that this location in reference to total gap length of the piston is:

$$\frac{L_{Apex} \, [mm]}{L_{piston\ length} \, [mm]} = 0.4167 \tag{4.7}$$

   With the center of the gap length being at 0.5, slightly less than that reflects a minor shift to the left.

3. The radius at the DC end of the piston due to the barrel design is the width between the center line of the original, cylindrical piston, the z_k-axis, measured to the circumference of the bottom of the piston. Normalized to the radius at the apex of the barrel, this parameter is:

$$\frac{R_1 [mm]}{R_2 \, [mm]} = 0.9996 \tag{4.8}$$

   This value is close to 1 since the apex of the barrel is shifted to the left and consequently the apex is closer to the bottom of the piston in which the bottom radius does not vary much from the radius at the apex.

4. The radius at the case end of the piston due to the barrel design is the width between the center line of the original, cylindrical piston, the z_k-axis, measured to the circumference of the top of the piston. The top of the piston is delineated as the end of the effective gap surface of the original, cylindrical piston on the case side. Normalized to the radius at the apex of the barrel, this parameter is:

$$\frac{R_3[mm]}{R_2\,[mm]} = 0.9984 \tag{4.9}$$

Conversely, this value is smaller than that of the normalized value of the bottom radius as it is further from the apex resulting in a larger curvature at the case end.

4.4 Sinusoidal Waved Barrel Surface Profile (Waved Barrel)

Also analyzed is a barrel design overlaid with a sinusoidal wave in the axial direction, Figure 4.5.

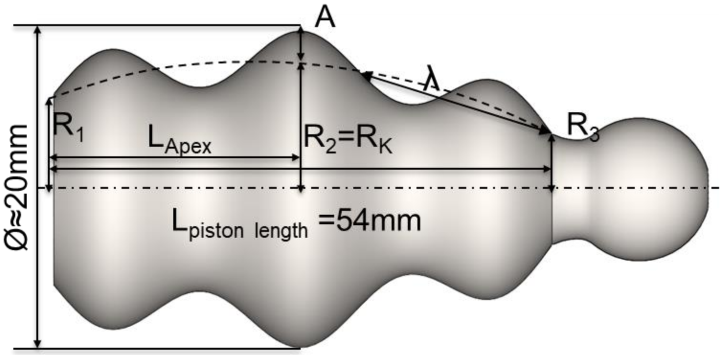

Figure 4.5. Sinusoidal wave barrel piston surface profile.

Being a combination of designs, the design parameters defining the geometry includes those of the barrel, the apex location and radius along with the radii at both ends of the gap of the piston, as well as those of the sinusoidal wave, the amplitude and wavelength. The sinusoidal waved barrel surface profile geometry simulated in this study is defined from the previously specified parameters of the two designs while maintaining the location of the apex.

1. The amplitude for this design remains the same as that described for the sinusoidal wave in section 4.1:

$$A_N = \frac{A\ [\mu m]}{R_K\ [mm]} = 0.29‰ \tag{4.10}$$

2. The number of waves for this design also remains the same as that described for the sinusoidal wave in section 4.1:

$$N = \frac{L_{piston\ lengh}\ [mm]}{\lambda [mm]} = 2.5 \tag{4.11}$$

   In order to compensate for the intersection with the left shift of the apex of the barrel, the wavelength becomes slightly compressed on the DC end and stretched on the case end as can be seen in Figure 4.6.

3. With a hard constraint on the location of the apex, this normalized parameter is again equivalent to that presented in section 4.3:

$$\frac{L_{Apex}\ [mm]}{L_{piston\ length}\ [mm]} = 0.4167 \tag{4.12}$$

   Under such conditions, the sinusoidal wave peak is forced to intersect the apex of the barrel as to not shift the location. A previous parameter study concluded that the location of the apex is the most impacting parameter; the reported value selected from this study.

4. The apex, or peak, is still defined as equivalent to the radius of the original, cylindrical piston:

$$R_{\ 2}[mm] = R_K\ [mm] \tag{4.13}$$

5. The radius at the DC end becomes:

$$\frac{R_{\ 1}[mm]}{R_2\ [mm]} = 0.9993 \tag{4.14}$$

This value is slightly smaller than the value reported in section 4.3. The combination with the sinusoidal wave results in a larger radius at the DC end since the amplitude is added to the radius of the barrel. This is due to the wave being shifted down such that the apex radius is equivalent to the original radius of the piston. This circumstance can be seen in Figure 4.6 with a comparison between the barrel and sinusoidal waved barrel designs.

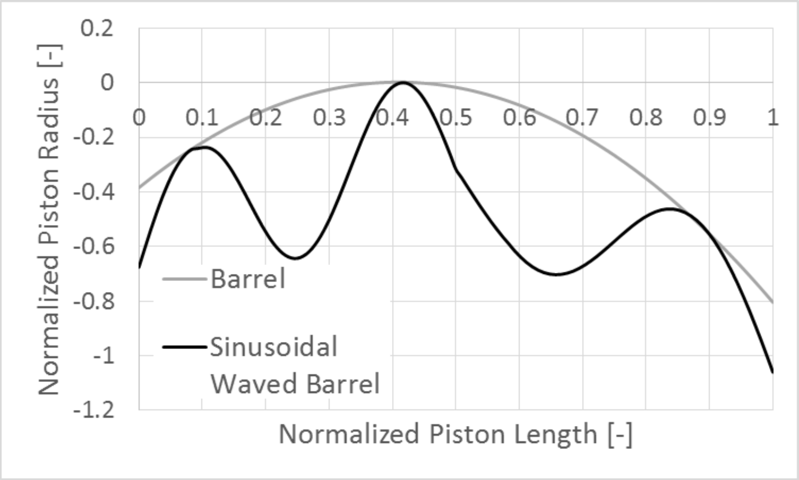

Figure 4.6. Barrel vs. sinusoidal waved barrel.

6. The radius at the case end becomes:

$$\frac{R_3[mm]}{R_2\ [mm]} = 0.9989 \tag{4.15}$$

Similarly to the DC end, this value is slightly smaller than that shown in section 4.3 again due to the combination of the sinusoidal wave with the barrel design.

4.5 Circumferential Sinusoidal Wave Surface Profile (CircSine)

A fifth and final novel design investigated in the following research study is a sinusoidal wave around the circumferential surface of the piston, Figure 4.7. This design targets the rotating motion of piston within the bore to aid in fluid pressure build up in order to support the external loads at a reduced clearance.

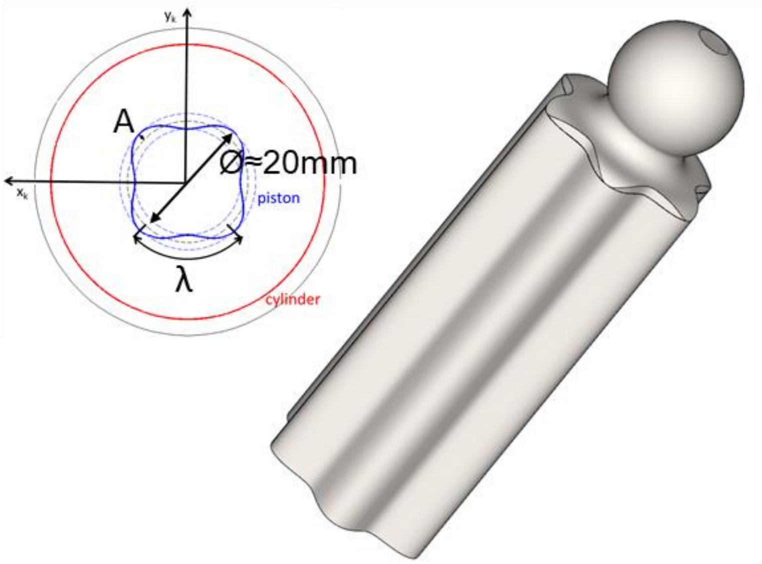

Figure 4.7. Circumferential sinusoidal wave piston surface profile.

Although in the circumferential direction, the sinusoidal wave is defined in the same way as the axial design, section 4.1, with a specific amplitude and wavelength describing the parameters of the geometry.

1. The amplitude of the sinusoidal wave, with the center line remaining at the original radius of piston, normalized to the radius of the piston is again:

$$A_N = \frac{A\ [\mu m]}{R_K\ [mm]} = 0.29‰ \tag{4.16}$$

2. With a wavelength in reference to the circumference of the piston of:

$$\lambda_N = \frac{\lambda\ [mm]}{C_K\ [mm]} = 0.167 \tag{4.17}$$

   Where the number of waves is expressed as:

$$N = \frac{C_K\ [mm]}{\lambda [mm]} = 6 \tag{4.18}$$

   For the circumferential design, the number of waves must be a whole number such that the sinusoidal wave is continuous around the circumference of piston.

4.6 Configuration of Micro-Surface Shaped Piston and Cylinder Bore

With the addition of a micro-surface shape on the piston, it becomes feasible to alter the configuration of the piston with respect to the cylinder bore. The surface shaping allows for a reduced clearance due the manipulation of the fluid film resulting in additional fluid support. Not only does this additional fluid support lead to a more reliable machine, but also increased efficiency since the possibility of a reduced clearance results in a decrease of leakage without greatly increasing torque loss.

1. The minimum radial clearance is defined as the distance from the peak point of the surface shape on the piston to the surface of the cylindrical bore, the minimum fluid film thickness under parallel gap conditions, h, normalized to the cylindrical radius of the piston. The reduced value considered throughout the micro-surface shaping investigation of the detailed designs is:

$$MRC = \frac{h\ [\mu m]}{R_K\ [mm]} = 0.96‰ \qquad (4.19)$$

CHAPTER 5. MODEL VERIFICATIONAND PRODUCTION UNIT BASELINE SIMULATION

A commercialized, standard 75cc stock unit was adopted as a baseline design. As an existing unit, this baseline can be measured and is also known to work reliably and efficiently. Foremost, the baseline was utilized to verify the simulation model as a useful tool to predict the lubricating interfaces behavior. The verification process consisted of comparing steady state measured losses to the overall predicted losses of the model over a wide range of operating conditions. Furthermore, the measured outlet and case temperatures can be used as accurate boundary conditions as an input to the simulation tool. Once a thorough baseline was established, the simulation results of a single interface can then be used to quantify improvements in operation as well as efficiency of various design possibilities tested through virtual prototyping. A deeper understanding of the impact of surface shaping has on fluid film geometry at reduced clearances can be reached in a more cost and time effective manner.

5.1 Steady State Measurements

Steady state measurements according to the ISO 4409 standard of testing, signifying a constant inlet fluid temperature to maintain a constant fluid viscosity, were conducted. The permissible systematic errors of the measurements were within the class B accuracy category as delineated in Table 5.1.

Table 5.1. ISO 4409 measurement accuracy class B.

Parameter	**Permissible error**	**Units**
Rotational frequency	± 1.0	%
Torque	± 1.0	%
Volumetric flow rate	± 1.5	%
Pressure < 2 bar gauge	± 0.03	bar
Pressure ≥2 bar pressure gauge	± 1.5	%
Temperature	± 1.0	°C

For the measurements, a standard, 75cc stock unit was tested with a common hydraulic fluid of viscosity grade 32. Accordingly, the temperature at the inlet was recorded in order to maintain the standard. Also recorded were the corresponding case and outlet temperatures to be later used as accurate boundary conditions in simulation. The pressure at the case, inlet, control, and outlet were measured and set according to the required and desired operating condition, sustaining a supply pressure of 25 bar throughout. Also, according to the desired operating condition, the rotational speed was set through the integrated controls of the electric motor. In order to quantify the losses of the unit, the leakage flow was determined based on the flow through the drain line minus the measured control flow that is additionally added to the case. The torque and outlet flow were also recorded in order to calculate the overall power loss of the unit calculated as:

$$\Phi_D = nM - Q_{HP}\Delta p \qquad (5.1)$$

The test set up is shown in Figure 5.1 for pumping mode of the measured 75cc unit where the inlet (blue lines) is at low pressure and outlet (red) is high pressure.

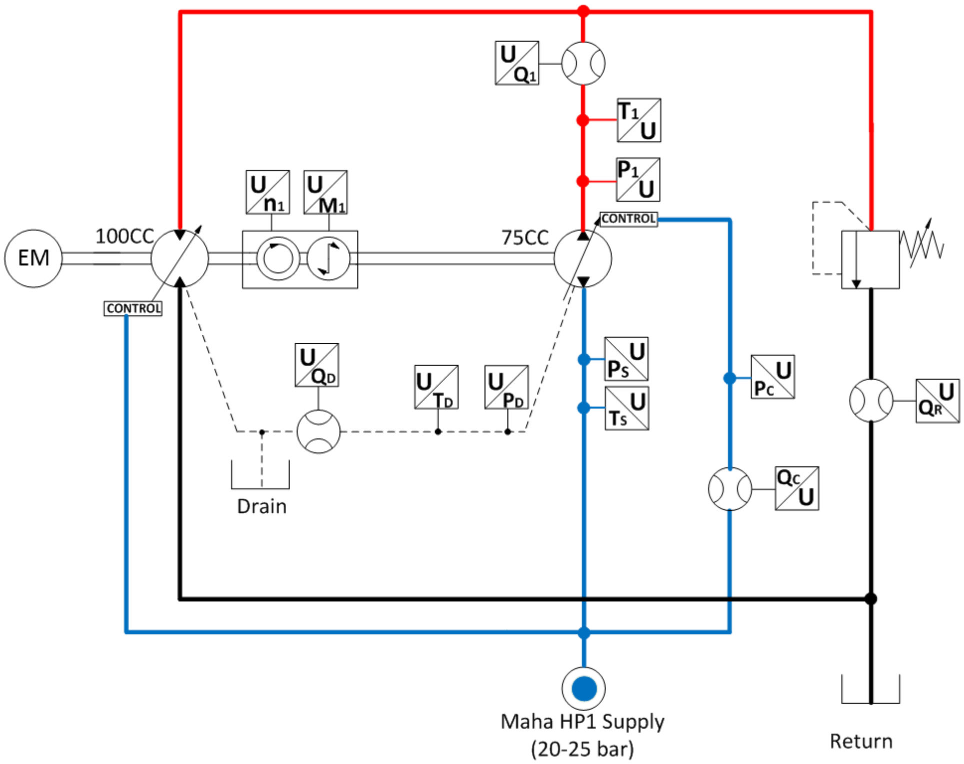

Figure 5.1. Baseline pumping mode test set up.

The data acquisition system used to record the measurements along with the implemented sensors are further detailed in Table 5.2 and Table 5.3 respectively.

Table 5.2. Steady-state measurement data acquisition.

Instrument	**Specifications/Functions**
NI cDAQ	• Data acquisition • Timing resolution of 12.5 ms
NI 9205	• 8-channel analog input module • Input range: ±10 VDC • Maximum sampling rate: 500 KS/s • Resolution: 12-bit`
NI 9211	• 8-channel thermocouple module • Input range: ±80mVDC • Maximum sampling rate: 14 KS/s • Resolution: 24-bit

Table 5.3. Steady-state measurement sensors.

Sensor	Measurement	Principle	Range	Output	Accuracy
Wika S-10	High Pressure	Piezoresistive and thin-film technology	0 - 600 [bar]	1-10 VDC	< 0.25 %
Wika S-10	Control Pressure	Piezoresistive and thin-film technology	1 - 100 [bar]	1-10 VDC	< 0.25 %
Wika S-10	Case/Low Pressure	Piezoresistive and thin-film technology	0 - 30 [bar]	1-10 VDC	< 0.25 %
VSE	Case/Return/ Control Flow	Gear flow meter with magnetic pick-up	0.02 - 18 [l/min]	V_{supp} - 1 VDC	± 0.3 % @ >20cP Repeatability ± 0.05 %
Kracht VC	HP Flow	Gear flow meter with magnetic pick-up	1 - 250 [l/min]	$0.8{*}V_{supp}$ VDC	± 3 % Linearity ± 1.5 %
Kistler	Torque	Strain gage	1 - 1000 [Nm]	± 0 to 10 VDC	0.5% Linearity ± 0.5 %
Omega Type K	Temperature	junction end thermoelements	180 - 1300 [°C]	N/A	±1.5 (−40 - 375 °C) ±0.004·T (375 - 1000 °C)

A wide range of operating conditions were measured in regards to capturing the speed, pressure, and displacement dependency of the resulting behavior of the unit. The displacement of the unit is set by controlling the inclination angle of the swashplate. Then the designated speed and pressure are adjusted. Once the operating condition is established, the cooling system is adjusted in order to achieve a constant inlet temperature of 52°C equivalent to a fluid viscosity of 20cSt. According to the measurement standard, the temperature must be within ±1°C for 10 minutes to be considered at steady state. Once steady state conditions are reached, the measurement data is recorded over a time frame; in this case 30 seconds at 0.1 second intervals. The measured operating conditions are shown below in Table 5.4.

Table 5.4. Baseline steady state measured operating conditions in pumping mode.

Operating Conditions						
n [rpm]	**Δp [bar]**	**T_{in} [°C] (lp)**	**T_{out} [°C] (hp)**	**T_{case} [°C]**	**Φ_D [W]**	**Q_{lk} [l/min]**
Pumping 100% beta						
500	5	51.91	52.41	52.22	419.2	0.54
500	50	51.89	53.28	52.89	690.3	0.69
500	100	51.86	54.25	53.5	1173.6	0.39
500	200	51.92	56.65	55.18	2583.5	0.70
500	300	52.05	69.48	58.46	4607.4	1.21
1000	5	51.93	52.58	54.24	967.7	1.07
1000	50	51.95	53.31	55.07	1300.7	0.68
1000	100	51.99	54.24	55.93	1932.1	0.49
1000	200	51.95	56.03	57.84	3607.9	0.82
1000	300	51.81	57.81	60.94	5976.3	1.30
2000	5	51.94	52.77	60.35	2892.7	0.88
2000	50	51.95	53.48	61.16	3470.3	0.94
2000	100	51.94	54.25	62.41	4306.0	0.76
2000	200	52.03	55.94	64.11	6302.3	1.08
2000	300	52.11	57.75	66.98	9857.8	1.90
2600	5	52.06	53.04	63.35	4694.3	1.60
2600	50	52.06	53.68	64.3	5321.8	1.61
2600	100	51.91	54.35	65.57	6308.3	1.50
2600	200	51.92	55.86	67.64	9110.8	1.73
2600	300	51.91	57.49	69.45	13474.5	2.54
3200	5	52.3	53.31	67.68	7260.3	2.52
3200	50	52.1	53.85	68.34	7684.5	2.56
3200	100	52.1	54.58	69.5	8859.5	2.57
3200	200	51.98	56.13	71.73	12348.7	2.70
3200	300	51.71	57.43	73.29	17054.7	3.33
3200	400	51.5	58.89	79.81	25582.6	6.67

Table 5.4 continued

n [rpm]	Δp [bar]	T_{in} [°C] (lp)	T_{out} [°C] (hp)	T_{case} [°C]	Φ_D [W]	Q_{lk} [l/min]
Pumping 20% beta						
1000	100	52.19	55.14	60.09	1575.3	2.40
1000	300	52.05	64.09	70.87	5881.1	5.07
2000	100	52.33	54.75	59.99	3028.6	2.63
2000	300	52.28	59.88	68.23	7771.4	5.45
2800	300	52.56	61.53	71.39	9765.6	6.76

5.2 Surface Wear Measurements

Considering that the geometry of the lubricating film directly effects the resulting pressure field and overall losses, the wear on the solid bodies that occurs during run in operation of the unit must be accounted for as it can be on the same order of magnitude as the lubricating film. Utilizing a profilometer, a surface measuring system similar to that shown in Figure 5.2 with specification as shown in Table 5.5, the resulting wear developed along the surfaces of the solid bodies after run in operation can be measured and used as accurate inputs to the model.

Figure 5.2. Mitutoyo profilometer.

Table 5.5. Profilometer specifications.

Manufacturer	Model	Measuring Range	Resolution
Mitutoyo	SJ - 500	±40µm (z-axis) ±50µm (x-axis)	0.001µm (z-axis) 0.05µm (x-axis)

5.2.1 Piston Surface Wear Measurement

Manufacturing error along the straight surface length of the piston and bushing as well as wear on the solid bodies during start-up and under certain operating conditions of the machine tends to occur. The resulting surface deviations can have an effect on the fluid film geometry and are therefore essential to evaluate in order to compare measurements to simulation. Since the effective gap length of the piston is longer than the trace length of the stylus of the profilometer, a trace must be made from both the case and the DC end along the same circumferential line around the piston as depicted in Figure 5.3 (right). To then ensure symmetry in the circumferential direction, this same technique is repeated several times around the surface of the piston, Figure 5.3 (left), for all nine pistons.

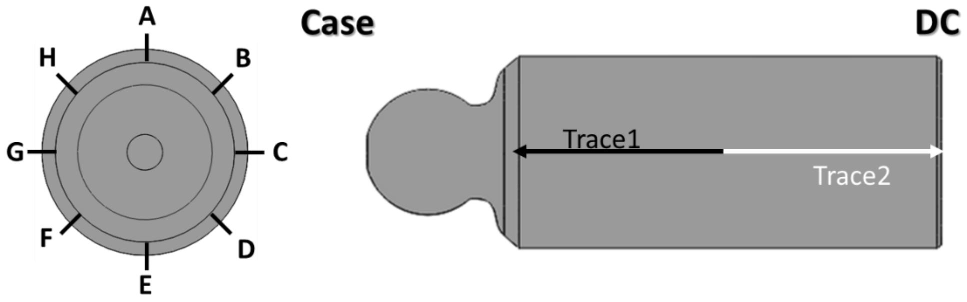

Figure 5.3. Piston wear profile measurement procedure.

A post-processing method was then applied to the raw data in which the trace is straightened, correcting for any misalignment of the piston in the measurement. The two circumferentially corresponding traces are then smoothed via a polyfit method to eliminate any noise or surface roughness measured and then combined at the center along a defined gap length of the piston. Since there is little wear that occurs on the steel piston against a more ductile bronze bushing, the wear on all nine pistons is very similar. Also, since the piston is free to rotate within the bore, the wear tends to be symmetric around the circumference. Therefore, an averaged two-dimensional macrogeometry representing the actual worn-in surface of the piston is sufficient to consider; the wear profile macrogeometry shown in Figure 5.6.

5.2.2 Cylinder Bore Surface Wear Measurement

On the contrary, the bushing is short enough to be captured in a single trace in which multiple traces are then made around the circumference of each bushing. For repeatability and accuracy, a measurement procedure depicted in Figure 5.4 was conducted. This method consists of rotating the block every 40° (9 bores over 360°) and measuring along the length of each bore sequentially (bores 1-9, traces A-I respectively for the block rotation shown). Utilizing this method ensures that each trace is in same location around each bore, i.e. trace A is always at the outer of bore. This is important to maintain as the wear is not symmetric around the circumference of the bore and must correspond to the coordinate system of the simulation.

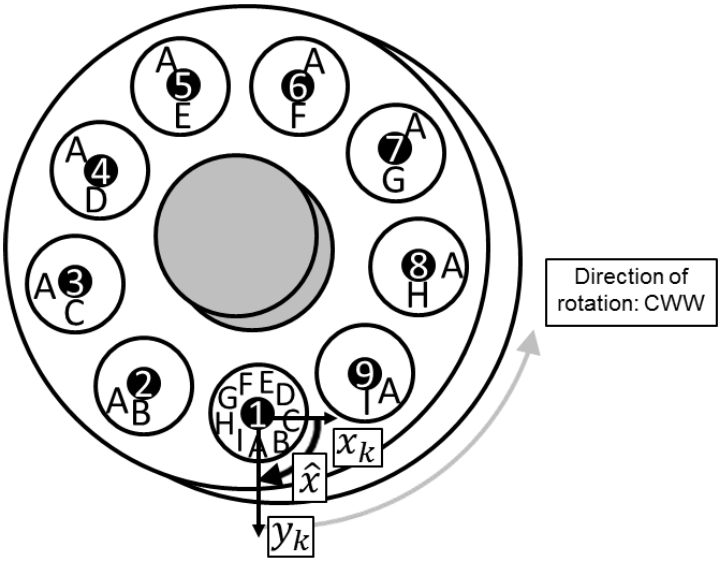

Figure 5.4. Bushing wear profile measurement procedure.

The raw data of the profilometer is then post-processed similar to that of the piston. The trace is straightened and then smoothed along the length of the bushing. Since the bushing does not wear symmetrically along the circumference depending on the operating conditions the machine was subjected to, a 3D representation of the bushing on the correctly correlated coordinate system, measurement shown in Figure 5.4 transformed to the simulation shown in Figure 5.5, must be considered. Since only one reference bore is investigated in the simulation model an average was taken of the axial traces of all 9 bores resulting in the actual wear profile macrogeometry as shown in Figure 5.6.

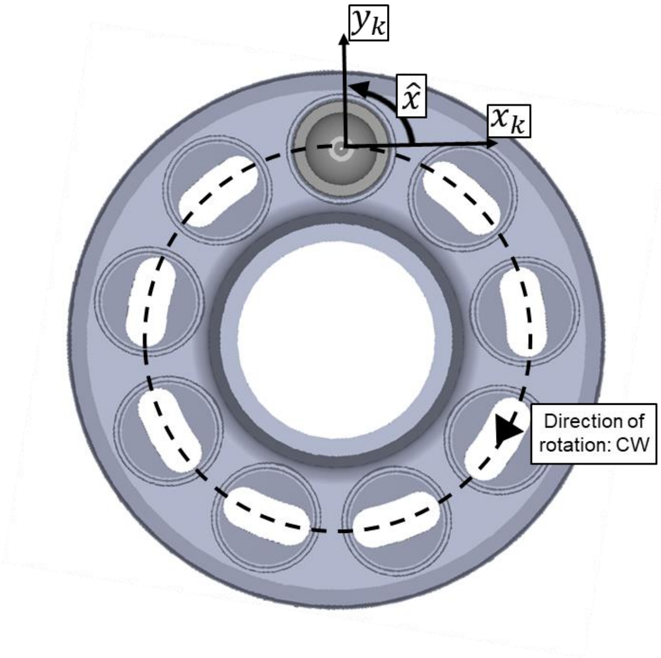

Figure 5.5. Bushing wear profile simulation coordinate system.

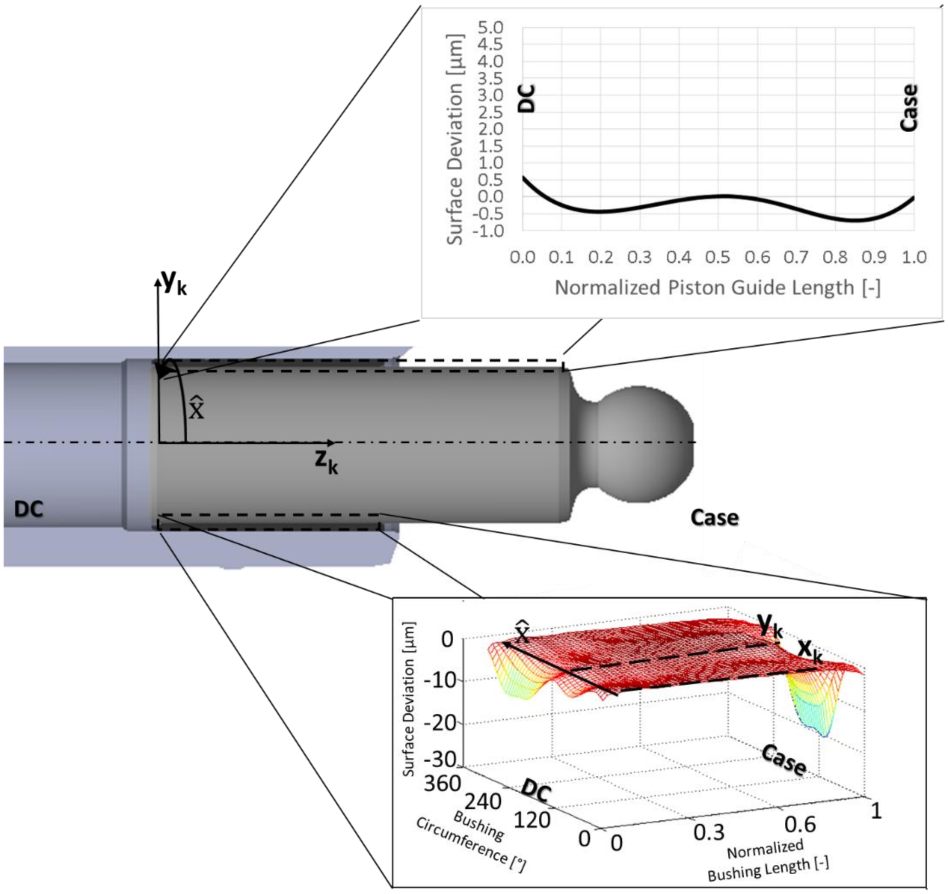

Figure 5.6. Piston/bushing measured wear profiles.

5.2.3 Slipper Surface Wear Measurement

Wear-in can also occur on the gap surface of the ductile bronze slipper against a steel swashplate. In this case, four traces were measured with the profilometer across the top surface of all nine slippers, as shown in Figure 5.7.

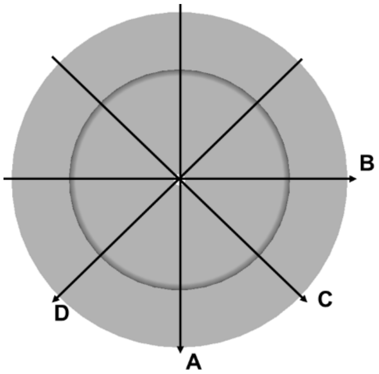

Figure 5.7. Slipper wear profile measurement procedure.

To post-process the wear profile of the slipper gap surface, the raw measurement data is plotted in which control points are then chosen to define the beginning and end of the two sealing lands over a known length from a single trace. Again to correct for any misalignment in the measurement, the trace is and then smoothed using a spline least squares method. The traces are then averaged, first between the inner and outer sealing land of a single trace, then of all four traces of a single slipper, and finally over all nine slippers. Again since the slipper is free to rotate, the wear is assumed to be symmetric around the circumference of the sealing land in which a two-dimensional macrogeometry is considered as shown in Figure 5.8.

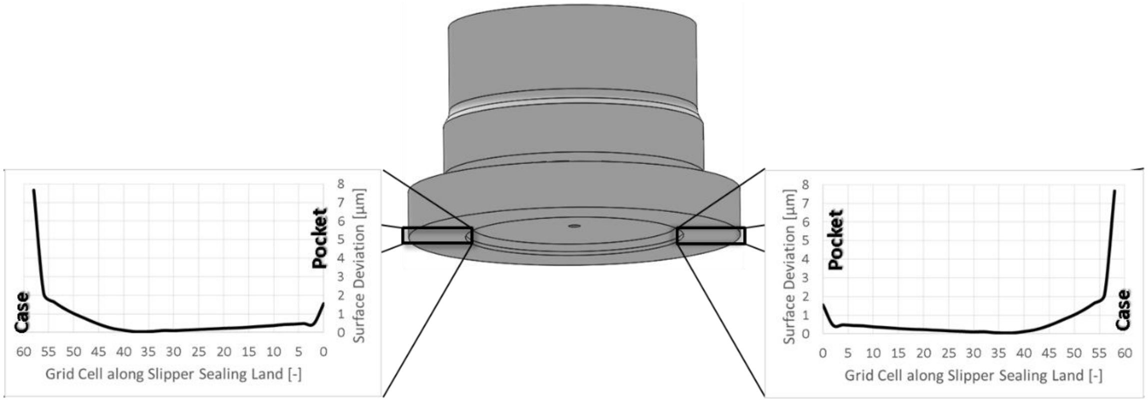

Figure 5.8. Slipper measured wear profile.

5.3 Piston/Cylinder Interface

For the baseline unit, a cylindrical, male piston and cylindrical bushing with wear profiles are considered. The diameter of each, d_k and d_z respectively, were also measured in order to accurately define the parallel gap height, h, resulting in a minimum radial clearance of:

$$MRC = \frac{h\ [\mu m]}{R_K\ [mm]} = 1.64‰ \tag{5.2}$$

The other important geometrical features of the interface are defined as shown in Figure 5.9 and were directly taken from drawings of the existing unit. In Figure 5.9, the piston is at outer dead center (ODC) and such the furthest out of the block throughout an entire revolution. As shown in Figure 5.10 the piston is 180° advanced in the revolution and at inner dead center (IDC), the furthest that the piston will be in the cylinder block over an entire revolution. Note that with this design in particular, the top end of the piston enters into the bushing. In this case, the gap is no longer defined by the length of the bushing; it becomes a variable gap length defined between the end of the bushing and the top of the piston that has passed into the bushing.

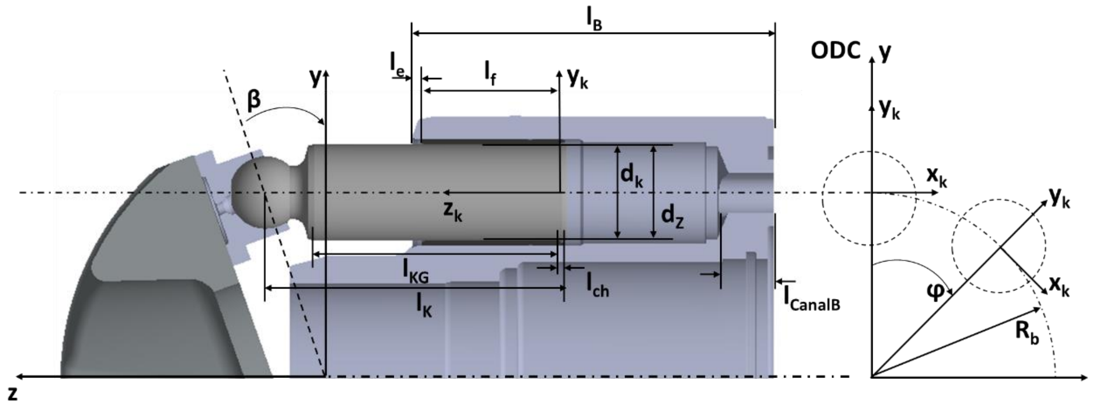

Figure 5.9. Piston/cylinder geometry; piston at ODC.

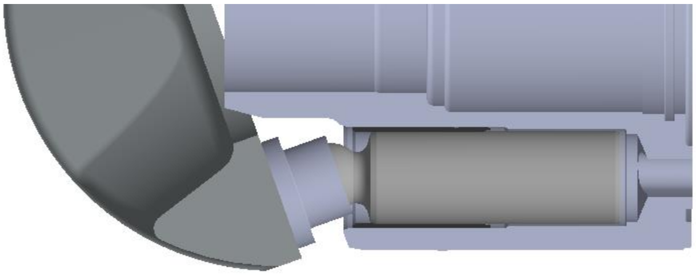

Figure 5.10. Piston/cylinder interface; piston at IDC.

The boundary conditions of the components of the piston/cylinder interface are important to define as representative of the physical real world as possible. These boundary conditions are utilized in not only solving for the Reynolds and energy equations of the fluid film module, but also for the pressure and thermal elastic deformations of the solid bodies.

Specifically the dynamic solution of the Reynolds equation results in a pressure field with concentrated areas of high pressure spikes due to the hydrodynamic wedge effect and squeeze motion in order to balance the external forces. Such pressure spikes in the fluid film can cause a deflection of the solid bodies that must be accounted for as they can be on order of magnitude as the fluid film thickness. Considering the dynamic pressure field and the effect of the resulting solid body deformations on the geometry of the fluid film, the deformation must be calculated each iterative step. Therefore, in order to conserve time, an influence method scheme is integrated into the FEM model and solved offline. The influence matrices created for the model are based on a tetrahedral mesh of the solid bodies with defined boundary conditions as shown in Figure 5.11. The lubricating interface of the cylinder bore and piston, labeled as “Gap”, are loaded with the calculated dynamic pressure field while the neighboring bores, “Cylinder”, are an average of the corresponding DC pressure and case pressure. The surfaces experiencing displacement chamber pressure, “DC”, are loaded with a uniform pressure that is applied based on the shaft angle defining either a high or low pressure. Finally, the “Case” is also a uniform pressure based on the operating condition.

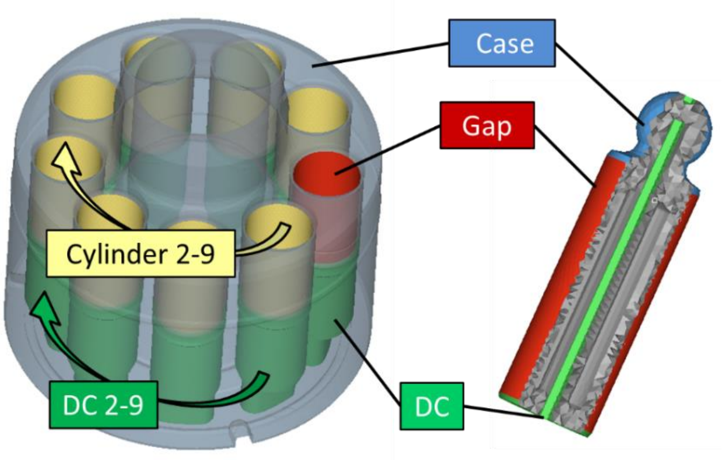

Figure 5.11. Piston/cylinder interface pressure boundary conditions.

The thermal problem of the solid bodies arises from the energy dissipation that is transferred from the fluid film to the solid bodies generating a gradient temperature field. This temperature distribution is not only considered in the fluid properties, but also in how the fluid film geometry is altered due to the thermal expansion of the solid bodies from the internal thermal stresses. The heat fluxes do not largely vary with the rotation of the block, therefore it is computationally and time affordable to calculate the complete FEM analysis online once per shaft revolution. The solid body temperatures are solved utilizing a tetrahedral mesh with user assigned boundary conditions, as defined in Figure 5.12. Neumann boundary conditions are considered for the “Gap” solid boundary surface since the heat flux at the face is calculated:

$$q_s = \frac{\lambda_{oil}}{\Delta \hat{z}_{fluid}} (T_{fluid} - T_s) \tag{5.3}$$

A mixed boundary is considered for the other solid surfaces, the “DC” and “Case”, since the operating temperatures are known and the convection coefficients can be well estimated from available literature:

$$q_s = \eta (T_{fluid} - T_s) \tag{5.4}$$

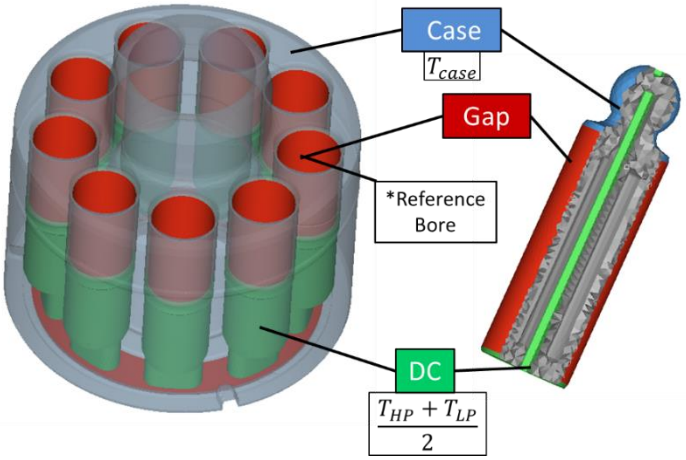

Figure 5.12. Piston/cylinder interface thermal boundaries conditions.

Both the cylinder block and the piston are not arbitrarily constrained in the real world and therefore adopt an inertia relief method in the model. This method balances the applied loads that are not in equilibrium with a generated translational and rotational accelerations attached to the center of mass of the structures.

Also, by defining the volumes of the meshes independently, the material properties of the steel piston and cylinder block with bronze bushings are considered in the determination of the solid body deflections.

5.4 Slipper/Swashplate Interface

The forces acting on the slipper/swashplate interface are essential to correctly define in order to gain a better understanding of the resulting lubricating film between the slipper and the swashplate. Considering that the slipper is connected to the piston, it too follows in rotation around the shaft in which a local coordinate system is defined. The origin of the slipper coordinate system is located at the center of the slipper along the face of the swashplate with the positive x_G-axis pointing outward in the direction of rotation, the positive y_G-axis pointing radially outward, and the positive z_G- axis normal to and pointing away from the swashplate as depicted in Figure 5.13.

Among the numerous forces acting on the slipper, as displayed in Figure 5.13, the primary force is a resultant force, F_{kS}, acting on the slipper transmitted from the piston through the ball joint; typically pressing the slipper toward swashplate acting along the z_G-axis:

$$F_{kS} = -F_{Sk} \tag{5.5}$$

The counteracting force from the piston, F_{Sk}, was defined previously in Eq. (2.16).

The slipper hold down force, F_{HD}, is a constant spring force pressing the slippers toward the swashplate if a spring is present in the design. On the contrary, if the design consists rather of a fixed hold down, the force is applied via a contact penalty method if the fluid film thickness exceeds the design clearance.

The rotation of the mass of the piston-slipper body also causes a centrifugal external force, $F_{\omega G}$, also acting on the slipper body:

$$F_{\omega G} = m_G R_B \omega^2 \tag{5.6}$$

This force tends to cause the slipper to tip about the x_G-axis:

$$M_{\omega G} = F_{\omega G} l_{SG} \tag{5.7}$$

A viscous friction force, F_{TG}, due to viscosity of fluid causes the slipper to drag against its motion:

$$F_{TG} = \int_A \tau dA \tag{5.8}$$

Additionally causing the slipper to tip about the y_G-axis as the force is reacted at the center of the piston head:

$$M_{TG} = F_{TG} l_G \tag{5.9}$$

The final moment introduced on the slipper is due to the friction between the piston/slipper ball-joint connection:

$$M_{TJ} = F_{frict} r_{sock} \tag{5.10}$$

Where $$F_{frict} = (k_p p_{ball} + k_v v_{tilt}) F_{KS} \tag{5.11}$$

The friction force dependent on the pressure as well as the speed.

Reacting the total axial external forces acting on the slipper body is the lubricating fluid force:

$$F_{fz} = \frac{\pi}{4}(d_{inG}^2 - d_{dG}^2) + \int pdA \tag{5.12}$$

Since the gap pressure is not likely to be radially symmetric, fluid moments about the x_G-axis as well as the y_G-axis occur:

$$M_{fx} = \int (p \cdot x_G) dA$$
$$M_{fy} = \int (-p \cdot y_G) dA \tag{5.13}$$

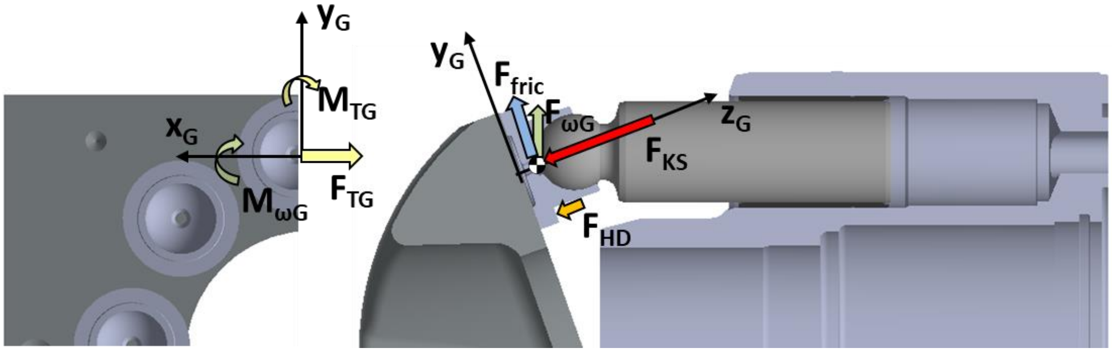

Figure 5.13. Forces acting on the slipper/swashplate interface.

The model in which to simulate the behavior of the lubricating fluid film between the slipper and swashplate is similar to that of the piston/cylinder interface (Section 5.3). This model is comprised of four co-dependent modules as illustrated in Figure 5.14. The first module solves for the lubricating film adopting the Reynolds equation, specifically considering the viscosity at each cell face rather than an average at cell centroid (full μ), and the energy equations as the basis. This modules solves for the fluid pressure field and slipper micro-motion in order to balance external force as well as the viscous friction heat flux. The second module, the heat transfer module, utilizes the predicted viscous friction heat flux to solve for the solid body surface temperatures and resulting internal thermal strain while predicting a more accurate temperature boundary for the previous module. The final two modules solve for the deformations of the solid bodies due to the internal thermal loading as well as the dynamic pressure field. The resulting change in the fluid film is utilized in the first module predicting the lubricating fluid. For further details reference (Schenk, 2104).

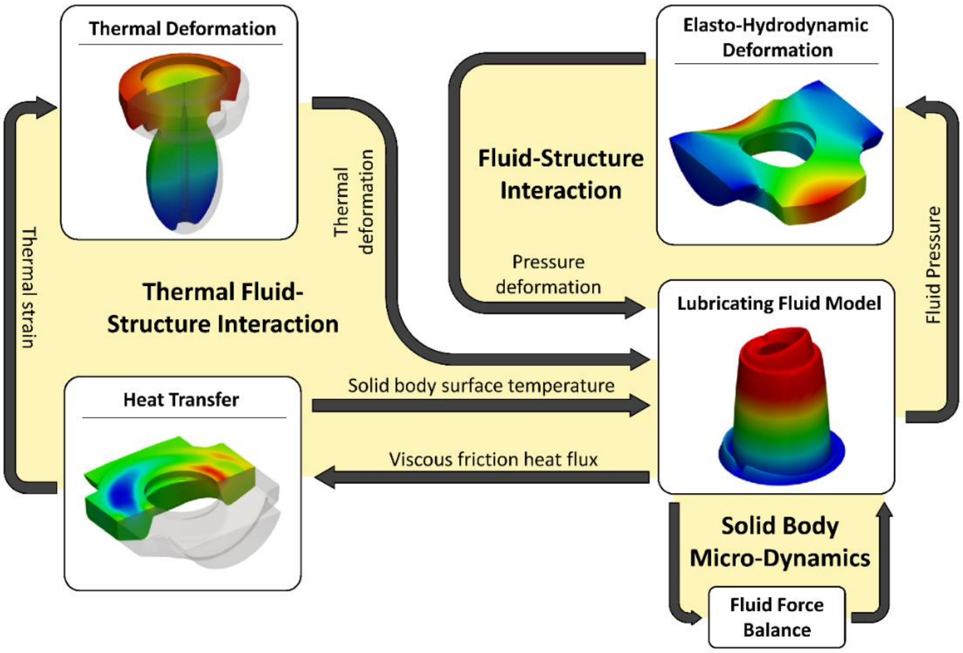

Figure 5.14. Slipper/swashplate lubrication model overview (Schenk, 2014).

For the baseline unit, a female slipper with a single sealing land design and a measured wear profile is considered. This particular unit has a fixed hold down to prevent lift off of the slipper in the low pressure stroke. The important geometrical features of the slipper are defined as shown in Figure 5.15 and were directly taken from drawings of the existing unit.

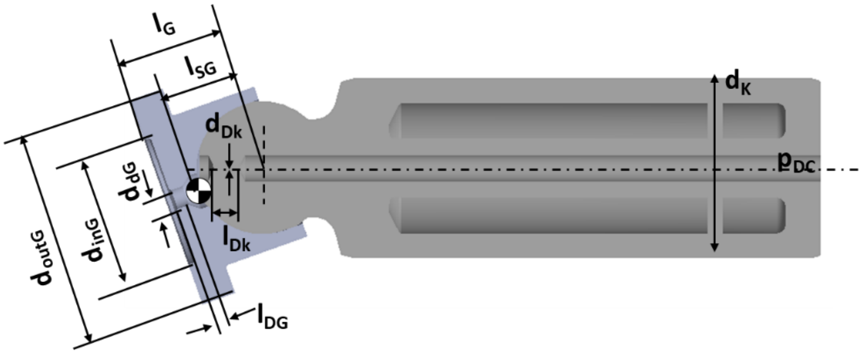

Figure 5.15. Slipper/swashplate geometry.

The defined boundary conditions of the components of the slipper/swashplate interface are influential in the solution of the first module of the model solving for the Reynolds and energy equations as well as the final two modules solving for the pressure and thermal elastic deformations of the solid bodies.

The resulting pressure field present in the fluid film in order to balance the external loads acting on the slipper causes deflections of the solid bodies in turn effecting the geometry of the fluid film. In this case, similarly to the piston/cylinder interface (Section 5.3), an influence matrix method is adopted and evaluated offline in the interest of time due to the dynamic pressure field over a shaft revolution. The actual loading conditions for simulation purposes are shown in Figure 5.16. The slipper sealing land, “Gap”, is loaded with an interpolated gap pressure while the running surface of the swashplate, “Gap”, is loaded with the fluid pressure from each slipper. The surface of the solid bodies subject to the “Case” pressure is loaded with a constant pressure based on the operating condition. The “Pocket” of the slipper is loaded with a uniform pocket pressure calculated over a shaft revolution via an internal pocket pressure model assuming turbulent flow of the pressure drop across the orifice restriction. Finally, the pressure in the slipper/piston ball joint connection, “Socket”, is simplified based on the reaction force to the piston, F_{KS}, and the projected ball area, A_{ball}:

$$p_{ball} = \frac{F_{KS}}{A_{ball}} \tag{5.14}$$

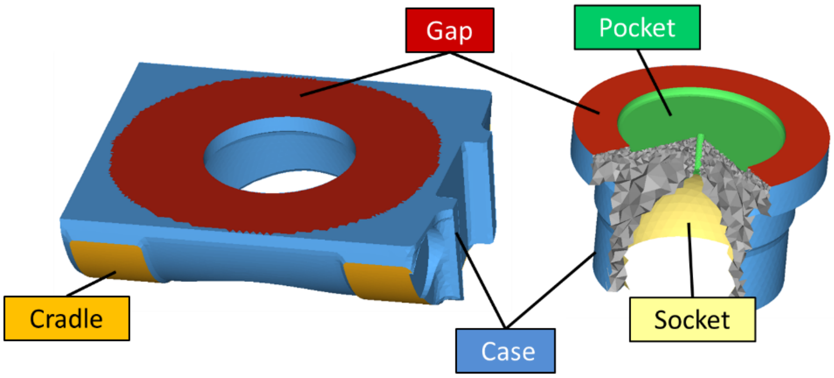

Figure 5.16. Slipper/swashplate interface pressure boundary conditions.

The viscous dissipation resulting from the thin fluid film is transferred as heat to the solid bodies through conduction. This temperature field causes an internal thermal stress on the solid bodies resulting in another source of deformation. The deflections largely effect the geometry of the fluid film and the resulting fluid film pressure generation becoming crucial to consider. Again, an FEM analysis is utilized to solve for the solid body temperature distribution once every shaft revolution. Predicting the solid body temperatures and the resulting deformations utilizes a tetrahedral mesh in which the bronze slipper and steel swashplate material properties are considered. The solid body meshes utilize user defined boundary conditions as shown in Figure 5.17; the same sets as for the pressure boundaries. For the “Gap” surfaces, it again follows that a Neumann boundary condition is considered, applying a specified heat flux. For the other solid surfaces, including the “Case”, “Pocket”, and “Socket”, a mixed boundary condition is considered in which a heat flux is indirectly applied through known temperatures and estimated convection coefficients from Newton’s law of cooling.

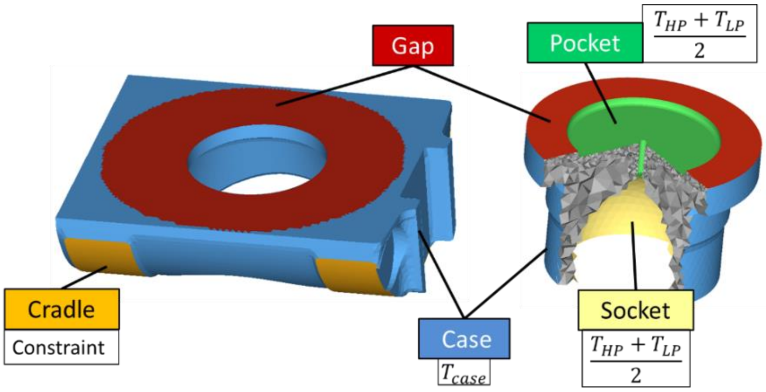

Figure 5.17. Slipper/swashplate interface thermal boundaries conditions.

It is typical to constrain the slipper via an inertia relief and the swashplate on the cradle mimicking the real world constraints.

5.5 Cylinder Block/Valve Plate Interface

Likewise to the other two interfaces, in order to correctly predict the behavior of the lubricating film between the cylinder block and the valve plate, the external forces acting on the solid bodies must first be defined appropriately. The global coordinate system previously defined for the unit in Section 2.1 is appropriate to define the forces acting on the cylinder block. Although nine pistons load the block, the forces are only described and shown for one in Figure 5.18.

The main load acting on the interface is directly applied to the cylinder block, on the surface of A_D, due to the pressurized fluid on each displacement chamber pressing the block toward the valve plate:

$$F_{DBi} = \int_{A_D} dF_{DB} = \int_{A_D} d(pda)n \cdot k \tag{5.15}$$

With an associated moment generated about the y-axis since high pressure fluid only acts on half the displacement chamber with low pressure on the other side:

$$M_{DB} \int_{A_D} dM_{DB} = \int_{A_D} r \times (pda)n \tag{5.16}$$

Also acting directly on the block is a constant axial thrust due to the spring force, F_{FB}, pressing the cylinder block toward the valve plate in order to ensure the block does not lift away. A viscous friction force, F_{TBi}, due to viscosity of fluid between piston and cylinder bore is transferred directly to the cylinder block in the opposing direction as well as a centrifugal force, $F_{\omega Bi}$, due to acceleration of piston/slipper mass in the radial direction. Finally, the external loads acting on the piston are also transferred to the block through the lubricating fluid, F_{RBi}, and also contribute to a bending moment mainly about the x-axis. The resulting external forces and moments must be balanced by the forces generated from the pressure field of the fluid; hydrostatically generated through the pressurized volume of the DC with the remaining hydrodyanmically generated from the relative micro motion of the surfaces.

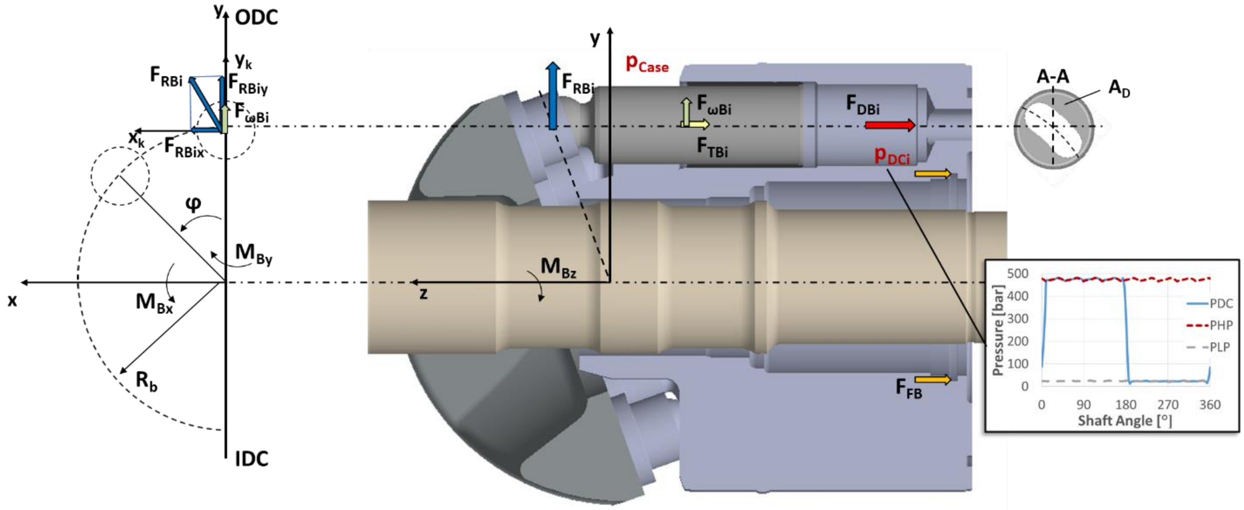

Figure 5.18. Forces acting on the cylinder block/valve plate interface.

Furthermore, the cylinder block/valve plate interface is modeled similar to the other two interfaces, comprised of four interdependent modules as detailed in Figure 5.19. The first module again solves for the non-isothermal fluid flow of the lubricating gap utilizing the Reynolds and energy equation yielding the dynamic pressure, temperature, and resulting heat flux field of the fluid film. The oil properties are updated based on the estimated pressure and temperature fields of the fluid to more precisely calculate the load carrying capacity and energy dissipation. The second module, the heat transfer module, utilizes the heat flux to solve for the solid body temperature distribution. The final two modules solve for the deflection of the solid bodies due to internal thermal loading and external pressure loading, updating the fluid film geometry. For further detail reference (Zecchi, 2013).

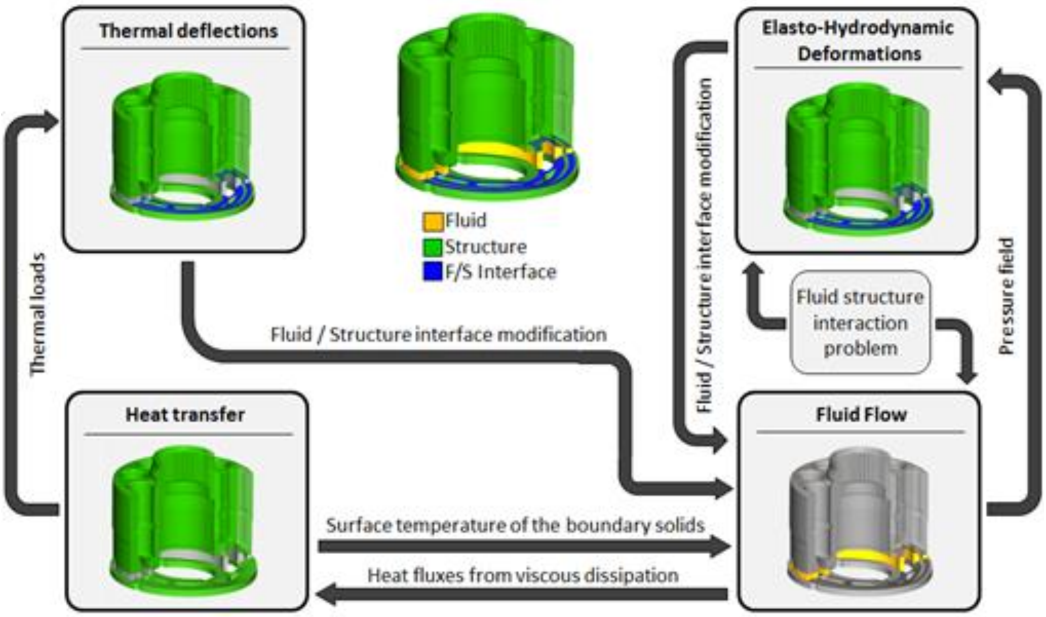

Figure 5.19. Cylinder block/valve plate lubrication model overview (Zecchi, 2013).

For the baseline unit, a flat cylinder block and valve plate surface is present. This particular unit also has a spring force hold down to prevent lift off of the cylinder block. The important geometrical features of the cylinder block, specifically the lubricating gap surface and the displacement chamber port openings, are defined as shown in Figure 5.15 and were directly taken from drawings of the existing unit. The interaction between the displacement chamber openings of the cylinder block and the high and low pressure ports through the valve plate is accounted for in the displacement chamber pressures detailed in Section 5.7. The forces from the displacement chamber pressure act on the surface defined in Figure 5.21.

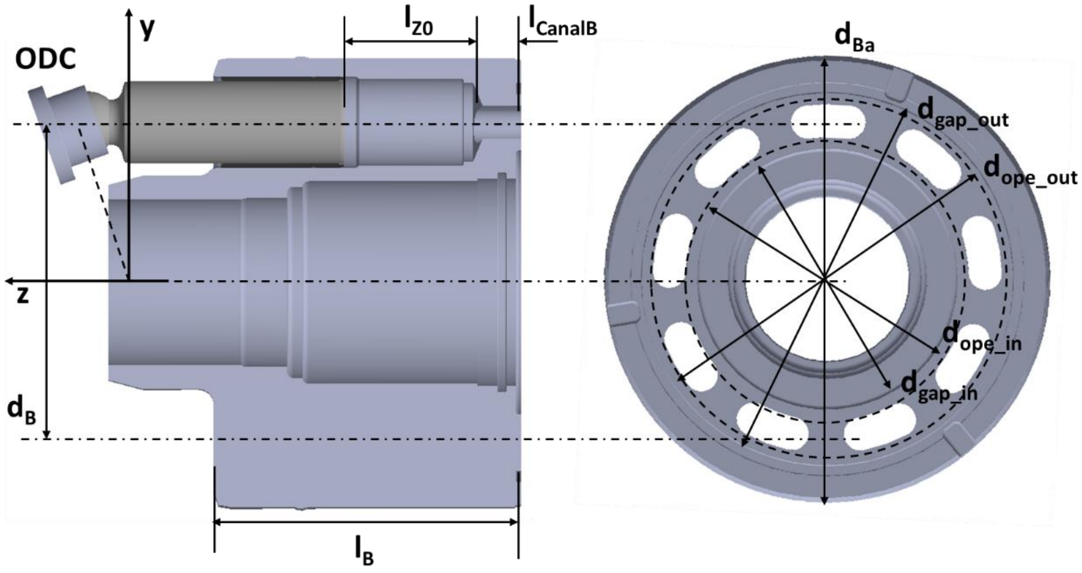

Figure 5.20. Cylinder block/valve plate geometry.

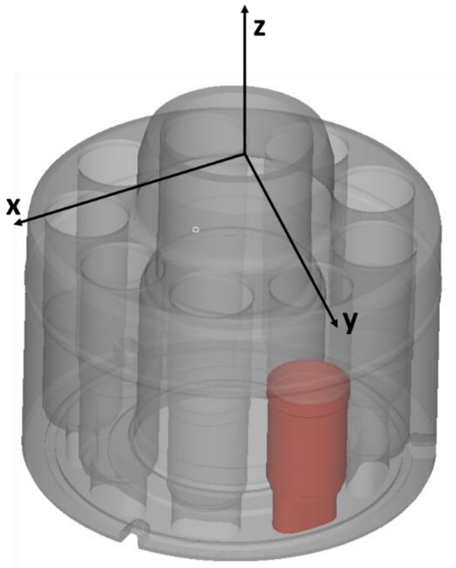

Figure 5.21. Displacement chamber surface.

Likewise for the cylinder block/valve plate interface, the deflection of the solid bodies due to external pressure and internal thermal loading are crucial to consider. Again for the pressure loading, Figure 5.22, an influence matrix method is adopted and run offline due to the time consuming calculations based on the dynamic, non-uniform pressure field applied to the "Gap" surfaces. The nine displacement chambers, "DC", of the cylinder block are uniformly loaded by the instantaneous cylinder pressure while the ports of the endcase, "HP" and "LP", are loaded with the corresponding high and low pressures.

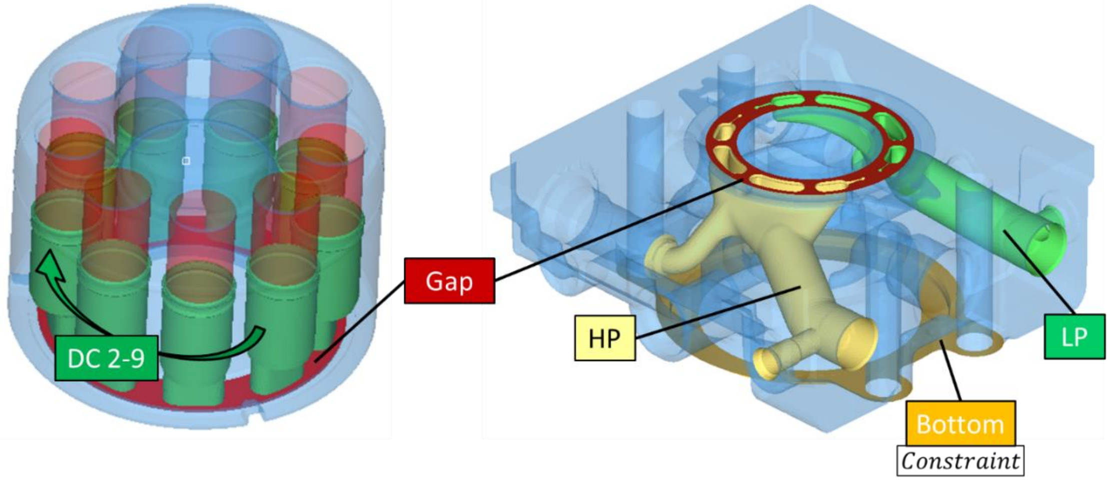

Figure 5.22. Cylinder block/valve plate interface pressure boundary conditions.

As for the thermal problem of the solid bodies, an FEM analysis solves for the solid body deformations due to the temperature distribution of a single shaft revolution online according to a tetrahedral mesh of the bodies with user defined boundary conditions as shown in Figure 5.23. The thermal deflections are limited to the volume of the valve plate, not allowing the endcase to deform underneath. The calculated heat flux is applied to the "Gap" surface under Neumann boundary conditions while a mixed boundary condition is considered for the other surfaces, the "Case" and "Air", the "HP" and "LP" ports of the endcase, and the "DC" of the cylinder block. Note that the thermal cylinder block mesh is equivalent to that of the piston/cylinder interface.

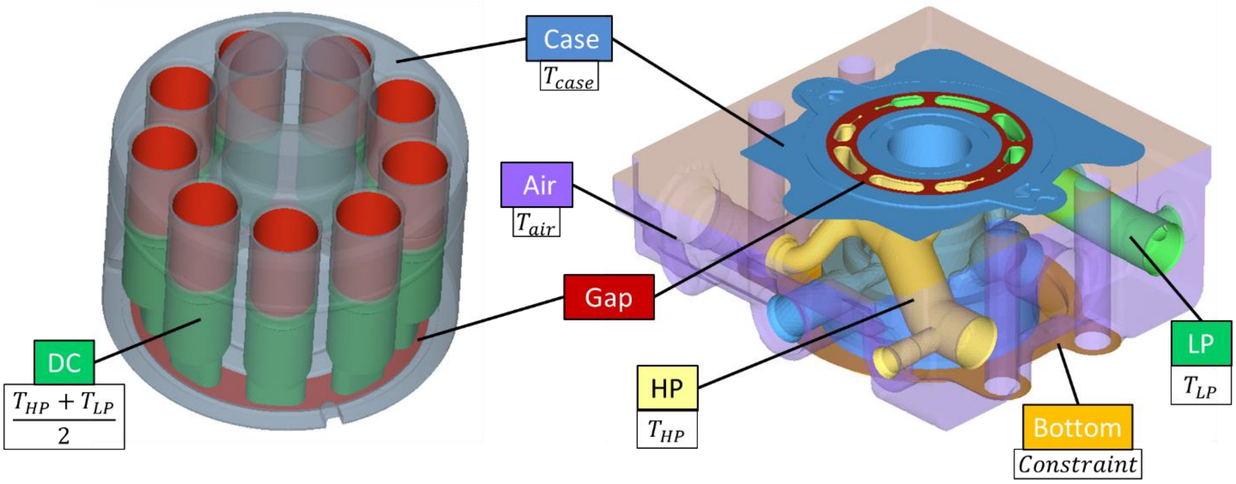

Figure 5.23. Cylinder block/valve plate interface thermal boundaries conditions.

The block is arbitrarily constrained via inertial relief while the endcase is constrained on the “Bottom” where it would be physically bolted metal-to-metal in the real world application. The steel endcase and valve plate are assumed to be welded together.

5.6 Operating Conditions

First, in order to verify the fluid structure interaction model that will then be utilized to investigate piston/cylinder surface shaping, a wide variety of measured steady state operating conditions must be considered to capture an overall picture of the phenomena occurring within the fluid film. With a constant inlet temperature of 52°C, the measured outlet and case temperature were applied as accurate thermal boundary conditions in the model, as previously listed in Table 5.4. The simulated results could then be compared to the measured losses of the machine.

Subsequently, once the capabilities of the model were confirmed, the corner operating conditions of the unit were taken into consideration encompassing the extremes. The corner operating conditions consisted of a combination of minimum and maximum speed, pressure, and displacement, as exhibited in Figure 5.24, for both pumping and motoring mode. Note that at partial displacement, the low speed, high pressure operating condition is actually at 1500rpm, 350bar due to the limitation of the displacement chamber pressure build-up under such conditions.

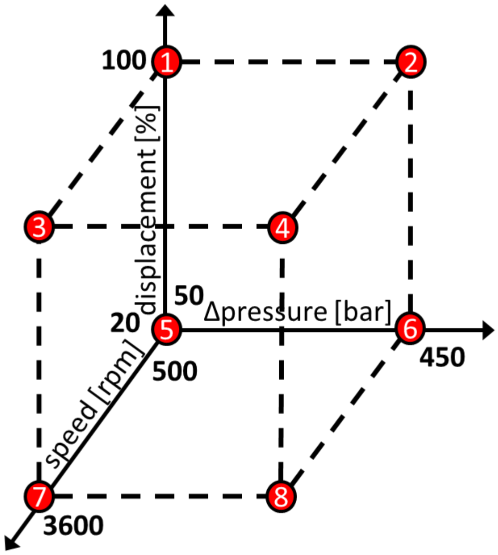

Figure 5.24. Corner operating conditions.

Since the corner operating conditions were not measured under steady state conditions, a thermal model (Shang and Ivantysynova, 2015) was iterated with the simulated losses of the unit resulting from the fluid structure interaction model until convergence for an accurate prediction of the thermal boundary conditions. The operating conditions at an inlet temperature of 52°C, corresponding to an oil viscosity of 20cSt, are listed in Appendix A in Table A.1 and Table A.2 for pumping and motoring mode respectively. Likewise, the operating conditions for an increased inlet temperature of 75°C, corresponding to a lower oil viscosity of 10cSt, are listed in Table A.3 and Table A.4.

5.7 Displacement Chamber Pressure

The instantaneous displacement chamber pressure is fundamental to predicting the performance of the unit overall. This dynamic pressure effects the forces acting on solid bodies over a shaft revolution along with the solid body deformations effecting the fluid film geometry for all three interfaces. The displacement chamber pressure also has a strong influence on the moment to overcome in order to change the displacement angle of the swashplate. Additionally, the rise and fall of the pressure within the displacement chamber significantly impacts the noise emission.

The displacement chamber pressure is determined based on the geometry of the valve plate connecting the cylinder block displacement chambers to the high and low pressure ports of the endcase; the normalized area file expressing the openings of the valve plate as shown in Figure 5.26. In order to calculate the pressure profile, it is assumed that the instantons pressure is uniform in the chamber in which a lumped parameter approach can then be applied to the control volume of the displacement chamber, Figure 5.25, to solve for the pressure build-up equation:

$$\frac{dp_i}{dt} = \frac{K}{V_i}\left(Q_{ri} - Q_{SKi} - Q_{SBi} - Q_{SGi} - \frac{dV_i}{dt}\right) \tag{5.17}$$

Where K is the bulk modulus fluid property, referring to Eq. (2.10) and Eq.(2.11) regarding the instantaneous volume, and the various Q terms are the flow in and out of the volume as illustrated in Figure 5.25.

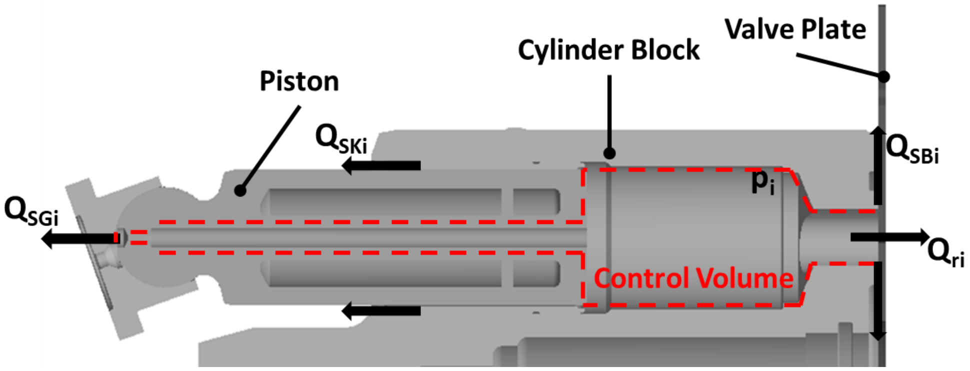

Figure 5.25. Displacement chamber control volume.

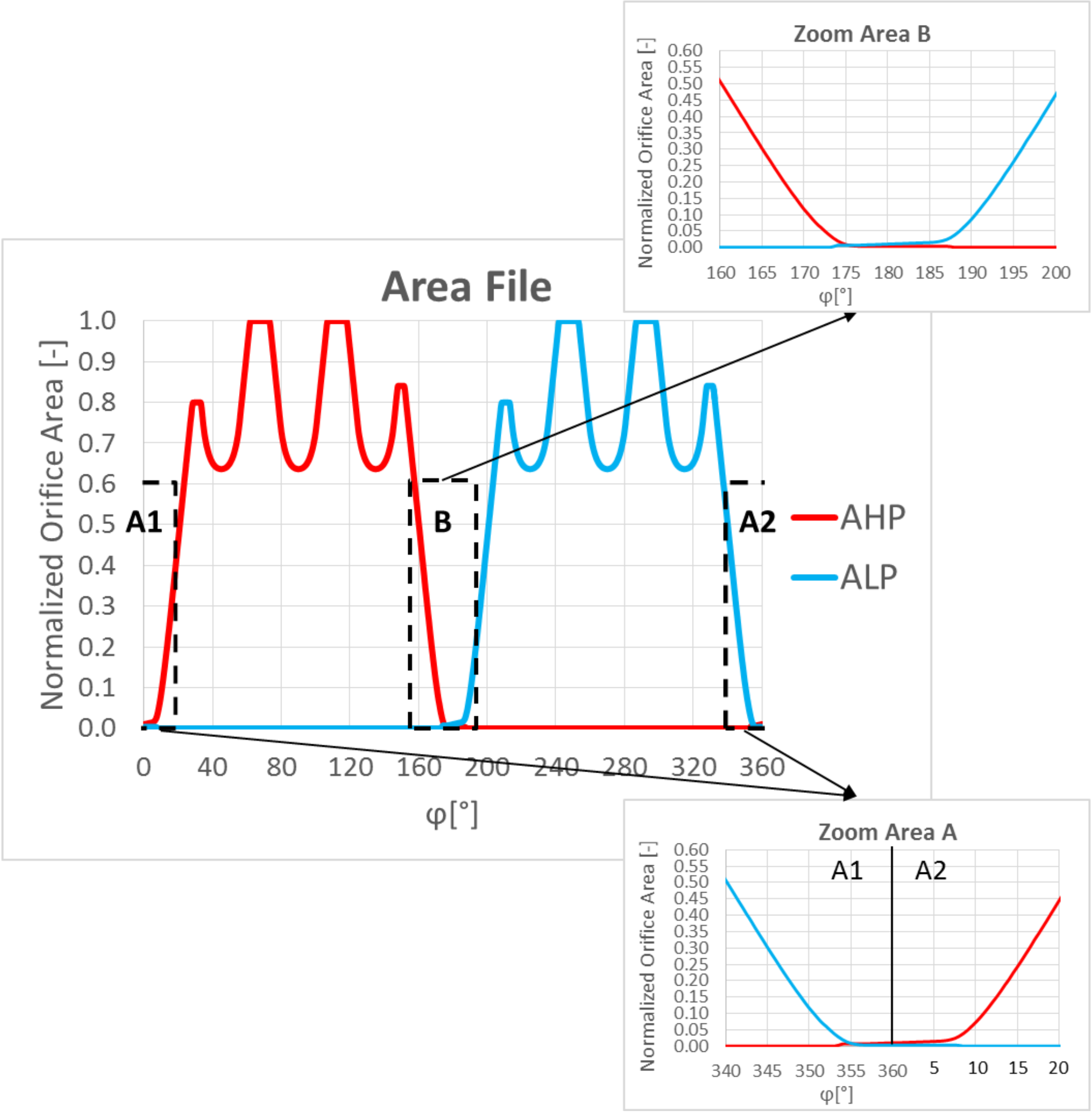

Figure 5.26. Area file of the valve plate.

According to the area file in Figure 5.26, the displacement chamber kidney opens to the high pressure port via the relief groove in the valve plate at 353°(zoom area A1) in which it then overlaps the relief groove of the low pressure port that closes completely at 8° (A2). The low pressure port opens again to the displacement chamber kidney at 173° via a relief groove overlapping the relief groove for the high pressure port that closes completely at 188° (B). The wave that is seen while the ports are open to the displacement chamber is due to the supporting bridges of the valve plate. Below are the resulting displacement chamber pressures over a single revolution for various operating conditions.

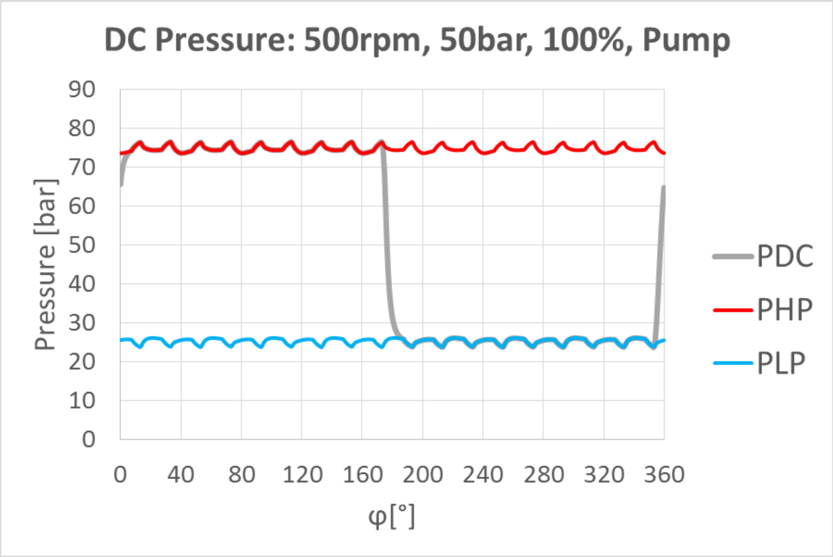

Figure 5.27. Simulated displacement chamber pressure over a shaft revolution for 500rpm, 50bar, 100% in pumping mode.

For an operating condition of a low speed of 500 rpm and a low differential pressure of 50 bar at full displacement in pumping mode, the resulting pressure profile is shown in Figure 5.27. The low pressure (blue line) remains around 25 bar and the high pressure (red line) remains around 75 bar over the complete revolution. The fluctuations that appear in the pressures is due to the kinematic flow ripple influenced by the fluid properties as well as the volumes of the low and high pressure ports. The pressure starts to increase at 353° as the kidney opens to the high pressure port via the relief groove. Since this is still in the suction stroke, the DC volume is increasing, increasing dV/dt term, counteracting the rapid increase in pressure. Transition into the discharge stroke at 0°, the DC volume decreases, dV/dt term decreases, in which the pressure then increases much faster. The DC pressure equalizes to high pressure as the low pressure port completely closes near 8° and the high pressure port fully opens past the groove. The pressure then starts to decrease at 173° as the relief groove to the low pressure port opens to the DC kidney and starts to close off to the high pressure port. Again since the DC volume is still decreasing in the discharge stroke, dV/dt term decreasing, the decrease in pressure is counteracted. By 180° the transition back to suction stroke occurs and volume increases resulting in a faster decrease in pressure. Finally, the DC pressure stabilizes to the low pressure as the low pressure port completely opens and the high pressure port is closed at 188°.

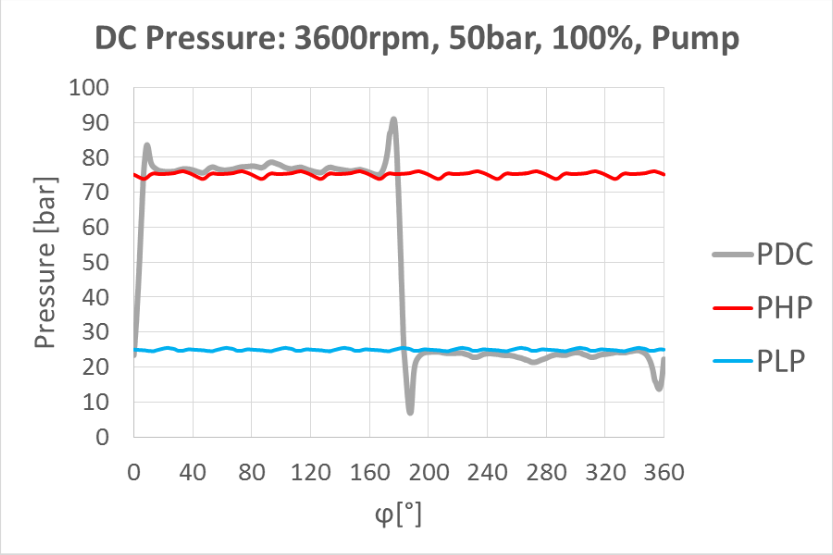

Figure 5.28. Simulated displacement chamber pressure over a shaft revolution for 3600rpm, 50bar, 100% in pumping mode.

Increasing the speed to 3600 rpm, while maintaining a low differential pressure of 50 bar at full displacement in pumping mode, the resulting pressure profile is shown in Figure 5.28. Since the operating pressure remains the same, similar phenomena of the high pressure and low pressure occurs. The difference arises with the increase in speed, decreasing the dt term, causing the dV/dt term to increase having a larger impact on the resulting DC pressure. For this reason, the pressure spikes at the transitions between the discharge and the suction stroke become apparent; the DC pressure rising and falling faster overshooting the set high and low pressures.

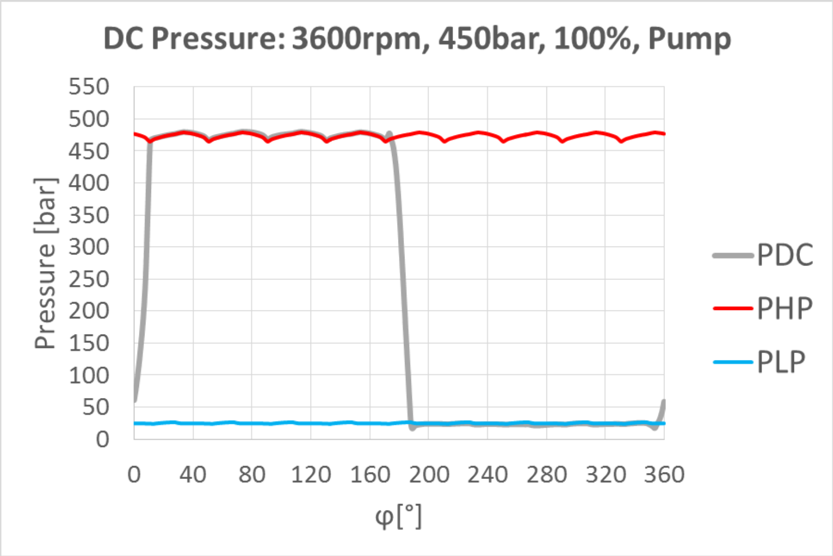

Figure 5.29. Simulated displacement chamber pressure over a shaft revolution for 3600rpm, 450bar, 100% in pumping mode.

Retaining a speed of 3600 rpm, while successively increasing the differential pressure to 450 bar (maintaining a low pressure of 25 bar) at full displacement in pumping mode, the resulting pressure profile is shown in Figure 5.29. In comparison to a lower pressure operating condition, the spikes at the transitions are significantly minor. The explanation for this is due to the change in timing. As the high pressure increases, it takes a longer period of time to reach the high or low pressure as the kidney opens to the port. This allows that the groove opens to the port completely by the time the pressure is reached equalizing more immediately in which no spikes occur.

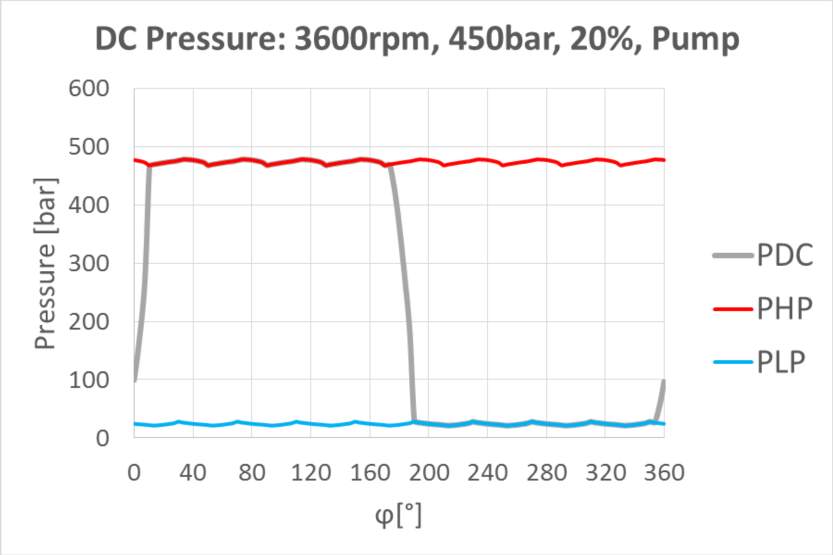

Figure 5.30. Simulated displacement chamber pressure over a shaft revolution for 3600rpm, 450bar, 20% in pumping mode.

By reducing the displacement of the unit to 20% in the case of high speed, 3600 rpm, and low differential pressure, 50bar, in pumping mode, the spikes at the transitions are no longer evident as can be seen in Figure 5.30. This decrease in displacement produces a smaller stroke of the piston, therefore a smaller dV term, resulting in less of an impact on the rise in pressure in which the overshoot in pressure is no longer experienced.

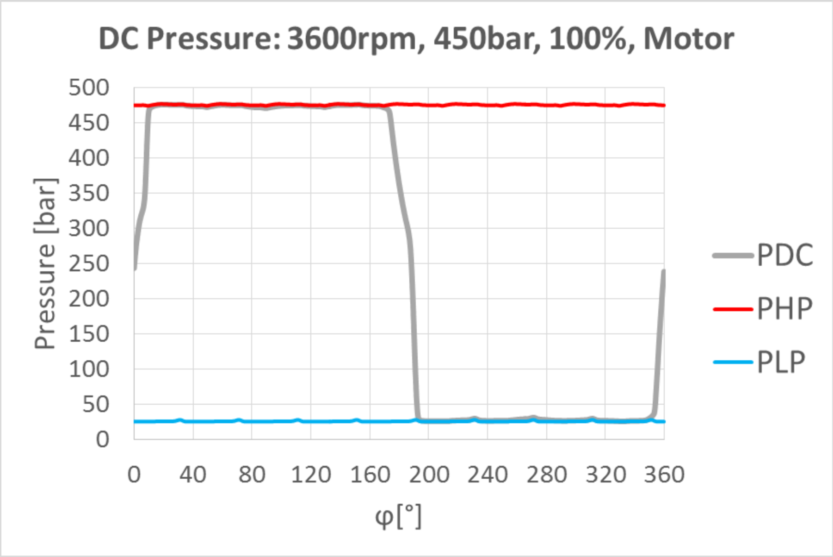

Figure 5.31. Simulated displacement chamber pressure over a shaft revolution for 3600rpm, 450bar, 100% in motoring mode.

Comparing motoring mode with the same high speed of 3600 rpm and high pressure of 450 bar at full displacement in Figure 5.31 to that of pumping mode in Figure 5.29, it can be seen that similar displacement chamber pressure results as expected. It remains that in simulation for motoring mode, the high pressure stroke is from 0° - 180°. The difference that arises with the reverse motion of the piston. For motoring mode, the piston is exiting the bore in the suction stroke at high pressure. This means that the DC volume is increasing, increasing the dV/dt term, in which the DC pressure is in turn not as rapidly increasing; vice versa for the discharge stroke at low pressure. This phenomenon is opposite that seen in the rise and fall of the DC pressure in pumping mode.

5.8 Model Verification

In order to verify the model used to predict the behavior of the lubricating interfaces, all three interfaces were simulated and compared to standard, baseline measurements at steady state performance. Since leakage of the machine was directly measured, measurement test set up shown in Figure 5.1, and a direct output of each interface of the simulation model, a comparison between this overall resulting loss is the preferred method of model verification. In order to portray the trends, the leakage dependency on the operating speed and pressure is presented.

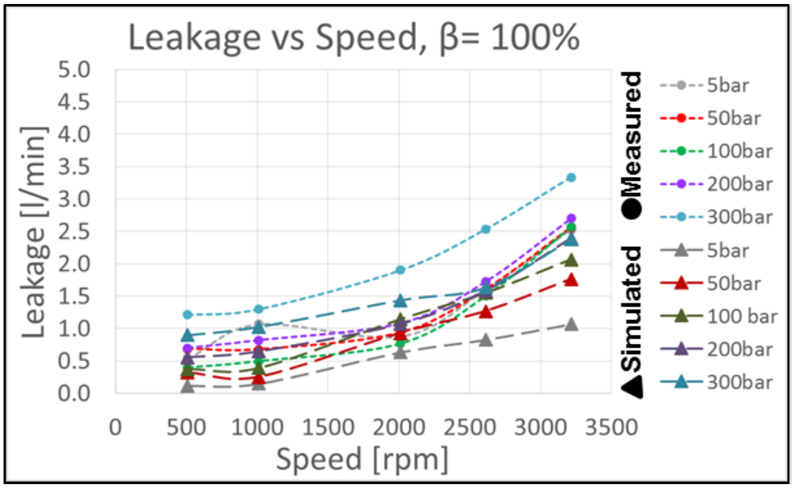

Figure 5.32. Leakage speed dependency; measured (●) compared to simulated (▲). Full displacement.

Figure 5.32 displays the dependency of the resulting leakage on the operating speed. It is shown that the leakage increases as the speed increases under full displacement operating conditions; the simulation (▲) following the measurement (●) trends. According to measurements, the leakage increases on average by about 2 l/min from 500 to 3200 rpm for all operating pressures. The resulting leakages predicted by the model slightly under-predict the magnitude of increase by about 0.5 l/min at the higher speeds.

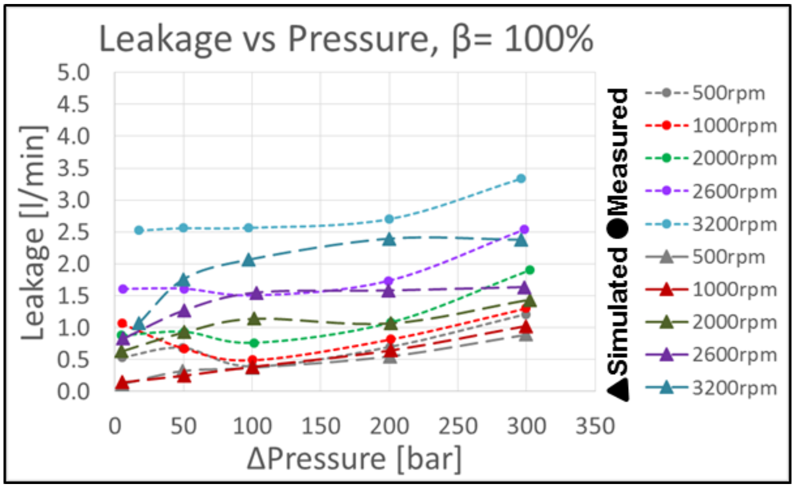

Figure 5.33. Leakage pressure dependency; measured (●) compared to simulated (▲). Full displacement.

At full displacement, the resulting volumetric losses are pressure dependent as well as shown in Figure 5.33. It follows that the leakage increases with the increase in operating pressure for both measurements (●) and simulation (▲). At the minimum operating pressure of 5 bar, the simulations slightly under predicts the magnitude of the measured leakage as well with the speed and pressure increase; the measured leakage increases much more than that of the simulation.

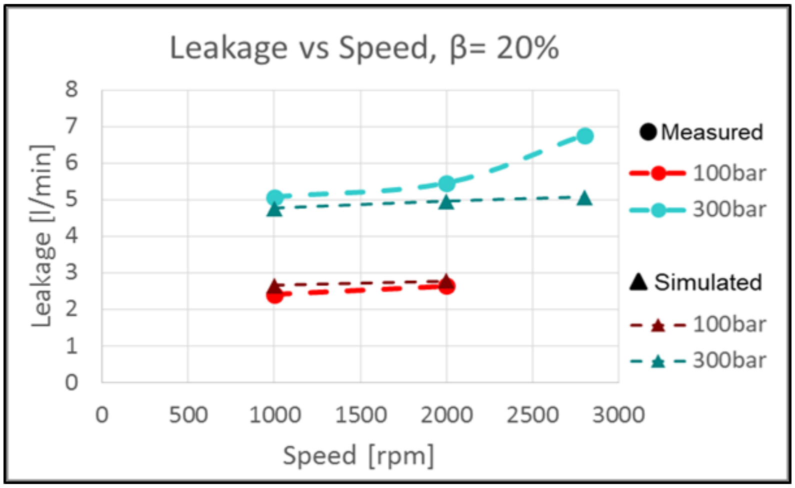

Figure 5.34. Leakage speed dependency; measured (●) compared to simulated (▲). Partial displacement.

For partial displacements, the leakages are similarly speed dependent, Figure 5.34, increasing with an increase in operating speed. According to the measured data for 300 bar, there is nearly a 2 l/min increase over the broadest range of increasing operating speed from 1000rpm to 2800 rpm. The predicted leakages resulting from the model are not as speed dependent, but do tend to slightly increase with speed. The intermediate pressure operating conditions, for 100 and 300 bar, the magnitude of the leakage actually matches quite well. As the speed and pressure increases, the simulation under-predicts the leakages again. The significant dependency on the pressure and displacement shown here signify major force dependency.

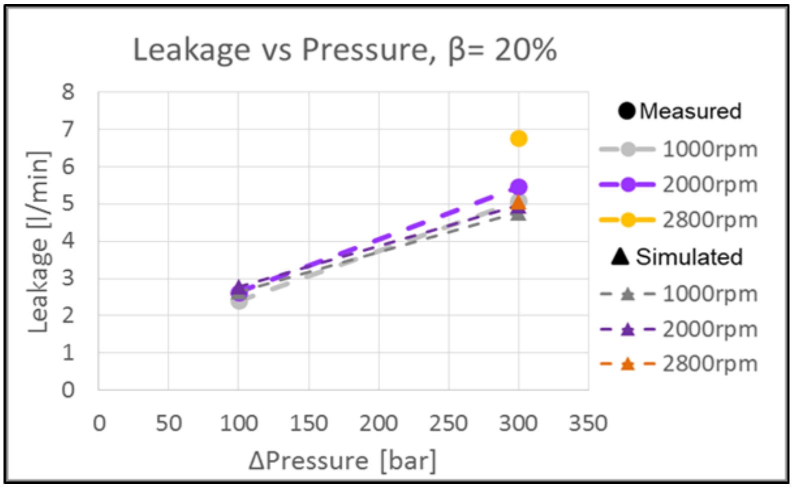

Figure 5.35. Leakage pressure dependency; measured (●) compared to simulated (▲). Partial displacement.

Figure 5.35 displays a trend of a much larger leakage dependency on operating pressure at partial displacements. The measured data reflects an increase of 3 l/min from 100 bar to 300 bar. At partial displacements, the leakages are much higher as the pressures increases in comparison to full displacement. Again, the simulations very well predict the trend, but under-predicts the magnitude of change at the higher pressures.

Overall, the trends of the measured leakage compared to that predicted by the model are very similar, although some differences arise in directly comparing the magnitude. The magnitude becomes under-predicted by the simulation at higher pressures and speeds, but this is acceptable since the combined volumetric losses are very sensitive to the fluid film thickness of all three interfaces. By simulating similar trends to that of the measured data, the capabilities of the model is validated.

A break-down of the overall simulated leakage for each interface is shown in Table B.1 in the Appendix in order to get a better understanding of the overall trends shown.

5.9 Simulation Results

Once the code was verified, the focus could be shifted specifically to the piston/cylinder interface at the corner operating conditions of the unit in order to test the capabilities of the machine under extreme conditions and over a broad range. Note that the simulations were run decoupled from the slipper/swashplate interface in which a parallel gap assumption is made in order to estimate the slipper viscous friction force. The simulations were also run decoupled from the cylinder block/valve plate interface in which an estimated constant heat flux is utilized. The simulated results of the baseline can then be used as a comparison to quantify the improvements of an extensive piston micro-surface shaping study via virtual prototyping.

The simulated energy dissipation and the corresponding volumetric losses, for the baseline at the range of corner operating conditions investigated in both pumping and motoring mode for T_{in} = 52°C, as listed in Table A.1 and Table A.2, are shown below in Figure 5.36 and Figure 5.37 respectively. The bar plots shown are an average of the losses over a complete revolution through the suction and delivery stroke for all nine pistons.

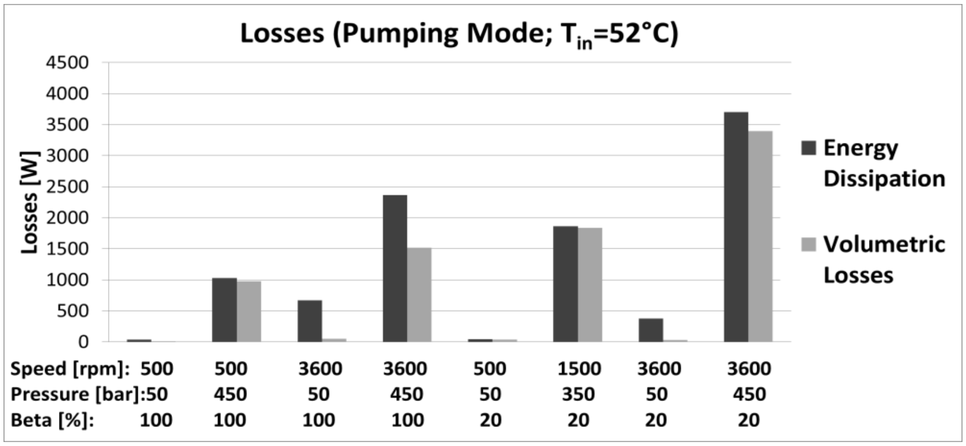

Figure 5.36. Baseline losses, pumping mode, T_{in}=52°C; piston/cylinder interface.

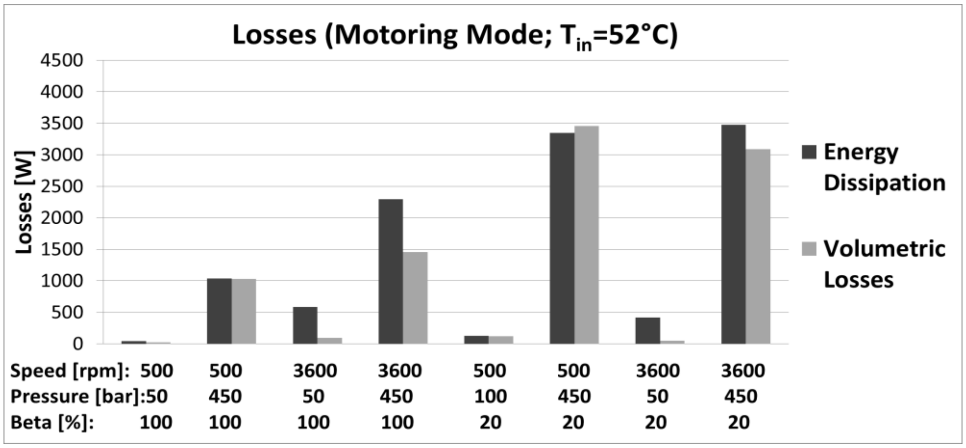

Figure 5.37. Baseline losses, motoring mode, T_{in}=52°C; piston/cylinder interface.

By increasing the operating speed, the volumetric losses are slightly increased while the mechanical losses become much more considerable as the side load and viscous shear of the fluid increases resulting in an overall increase in the total energy dissipation. As expected, by increasing the operating pressure, the volumetric losses are largely increased as fluid is forced from the gap due to the increase in differential pressure between the DC and case. The mechanical losses are also marginally increased with the pressure, consequently resulting in a comprehensive increase in the total energy dissipation. Decreasing the displacement decreases the mechanical shearing of the fluid but for the most part increases the volumetric losses enough to produce and overall increase in the total energy dissipation. Under partial displacement conditions, the stroke as well as the load on the piston is reduced resulting in a more centered piston within the bore. The one exception to this phenomenon is the high speed, 3600rpm, and the low pressure, 50bar, operating condition in which the overall energy dissipation is actually reduced. At this condition, the mechanical losses are significantly reduced additional to a slight decrease in the volumetric losses.

Although the trends between the operating conditions follow in both pumping, Figure 5.36, and motoring mode, Figure 5.37, the magnitudes vary. The differences arise as the motion of the piston is reversed for motoring mode and moves out of the bore during the high pressure stroke. Since the Couette component of the friction force opposes the motion of the piston, the Poiseuille component then opposes the Couette component generating a lower total friction force. As can be seen in the simulation results, at full displacements the volumetric losses tend to be slightly higher with similar mechanical losses resulting in a slightly larger total energy dissipation. However, for partial displacements, the mechanical losses are even larger in motoring mode resulting in a significant increase in energy dissipation in comparison to pumping mode as the piston tends to slide along the bushing, not tilting to build up the required fluid support.

Since the unit is expected to operate at higher temperatures resulting in a lower viscosity working fluid, the simulated energy dissipation and the corresponding volumetric losses for the baseline at the range of corner operating conditions is also investigated in both pumping and motoring mode for Tin = 75°C, as listed in Table A.3 and Table A.4, are shown below in Figure 5.38 and Figure 5.39 respectively.

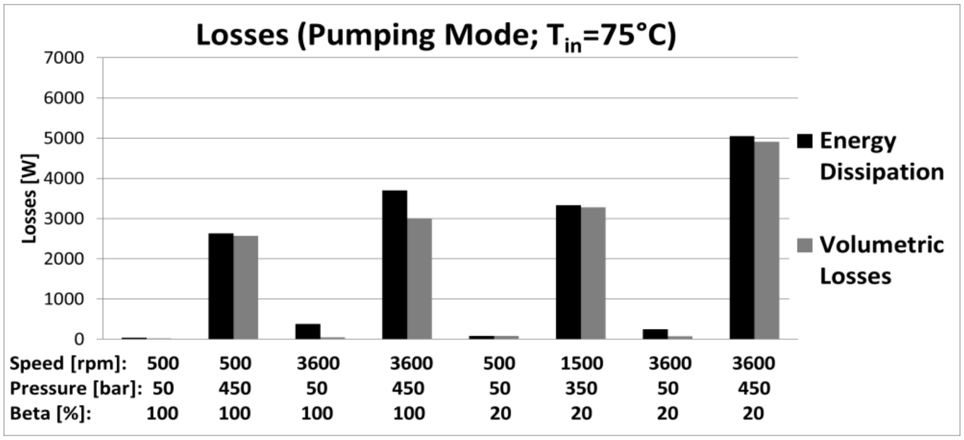

Figure 5.38. Baseline losses, pumping mode, T_{in}=75°C; piston/cylinder interface.

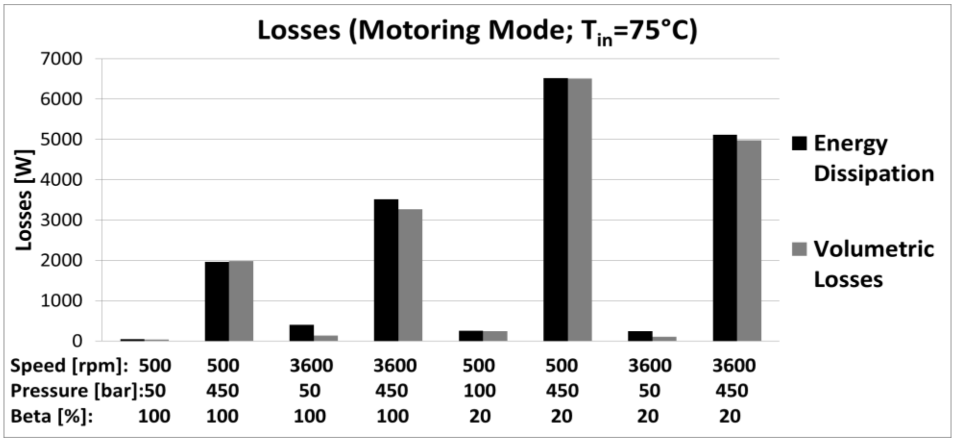

Figure 5.39. Baseline losses, motoring mode, T_{in}=75°C; piston/cylinder interface.

As far as the trends between the operating speed, operating pressures, and operating mode as described above, they continue to hold for a lower viscosity fluid at T_{in}=75°C. However, it can be noted that the losses are largely increased as the fluid viscosity is decreased. This phenomenon strongly relies on the volumetric losses, especially so at higher pressure operating conditions, as the fluid is able to flow more easily from the gap.

To further understand the phenomena occurring in the fluid film between the piston and cylinder producing the losses, multi-plots are presented. These plots display the fluid film thickness and fluid pressure over an entire revolution of the reference piston/cylinder segment. The individual plots over the revolution show the fluid film thickness in white contour lines and the corresponding fluid film pressure in the colored contour for an unwrapped gap of a single shaft angle. For the unwrapped gap the x-axis (ŷ) is the gap length that can vary with the motion of the piston, the y-axis (x̂) is the circumference around the gap. The rotating angle, φ, is measured from ODC in pumping mode and IDC in motoring mode where 0° to 180° is always shown as the high pressure stroke.

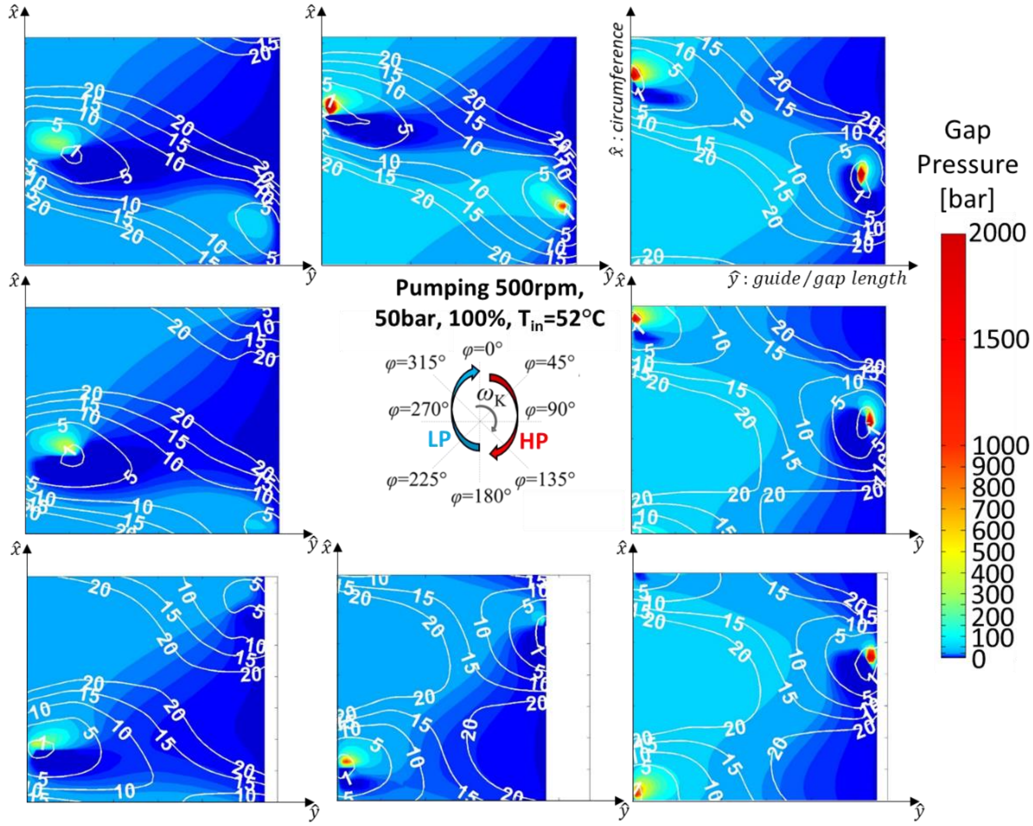

Figure 5.40. Baseline simulated multi-plots for pumping mode 500rpm, 50bar, 100%, T_{in}=52°C.

Figure 5.40 shows a low speed, 500rpm, and low pressure, 50bar, operating condition at full displacement in pumping mode. Since the side load on the piston is relatively small at the low speed and pressure, the piston is rather centered within the bore. Only meager areas of reduced film thickness occurs throughout the high pressure stroke requiring very minor pressure peaks in the fluid film. Note the variable gap length defined by the case end of the piston entering the bore near IDC at 180° as previously explained in Figure 5.9 and Figure 5.10.

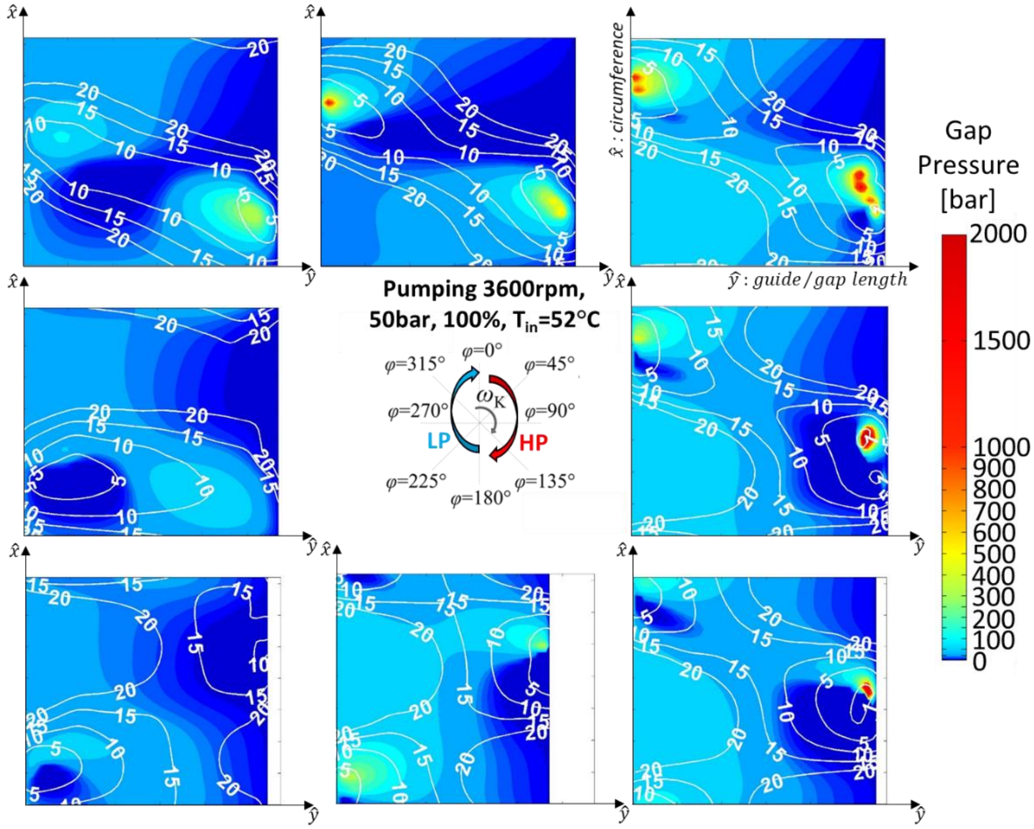

Figure 5.41. Baseline simulated multi-plots for pumping mode 3600rpm, 50bar, 100%, T_{in}=52°C.

The effect on the fluid film is shown in Figure 5.41 as the speed is increased to 3600 rpm while maintaining the low pressure of 50 bar at full displacement in pumping mode. Increasing the speed does not have a large effect on the motion of piston. The load on the piston is only slightly increased and therefore the areas of reduced film thickness on the ends become slightly more apparent in which an increase in fluid pressure is required to support the load. Along with the additional viscous shearing of the fluid, the resulting mechanical losses are increased. Although it can be seen that the piston tilts to create a good seal under such conditions, the increase in volumetric losses is mainly due to the fluid flowing out of the gap with the motion of the piston since the pressure remains rather low.

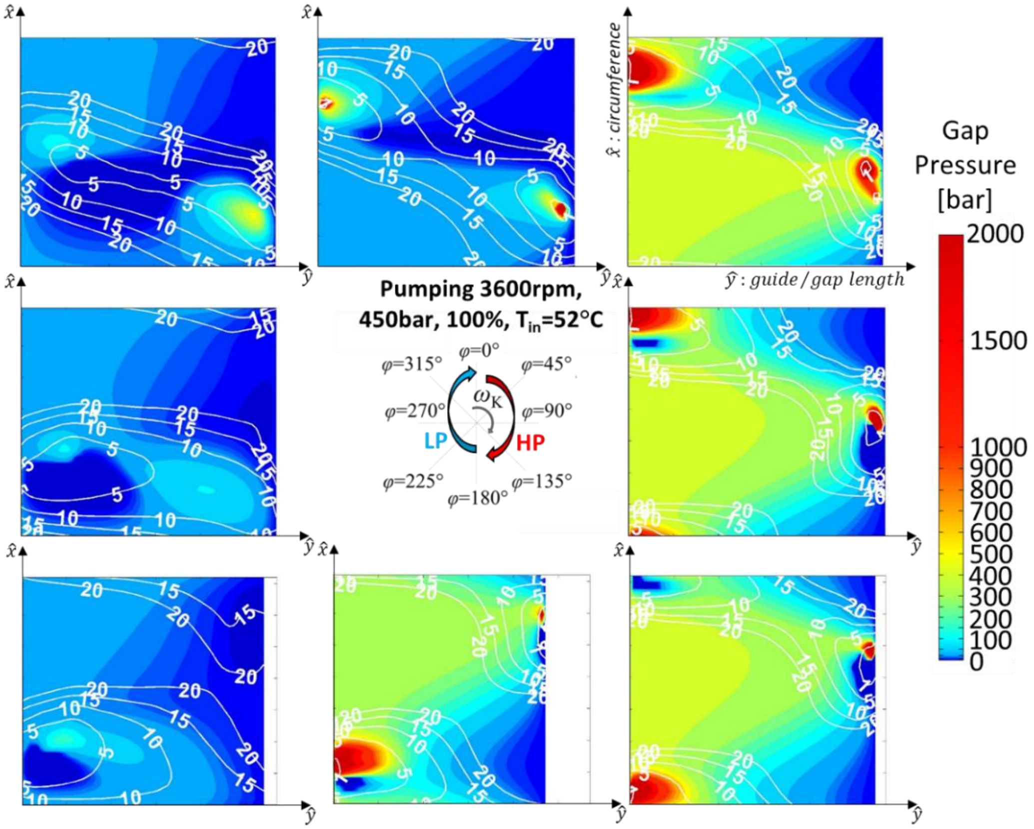

Figure 5.42. Baseline simulated multi-plots for pumping mode 3600rpm, 450bar, 100%, T_{in}=52°C.

The resulting phenomena of the fluid film from increasing the pressure to 450bar at a high speed of 3600rpm while still at full displacement in pumping mode is shown in Figure 5.42. Increasing the high pressure has a large effect on the external forces acting on piston causing the piston to tilt within the bore. This can be seen as the pressure in the fluid film spikes near the edges of the gap in order to support the additional load. Furthermore, with the high pressure, fluid is forced from the DC end to the case end flowing from the high pressure side to the low pressure side out of the gap through the channels of larger fluid film thickness created on the opposing circumference.

During the low pressure stroke, the forces are reduced and the piston tends to center itself as it moves out of the bore until the transition back to the high pressure stroke at φ=360°. As can be seen in Figure 5.43, the rise of the pressure in the DC chamber around φ=0° and the fall around φ=180° varies between the two operating condition. This can be seen in comparing the multiplots of Figure 5.41 and Figure 5.42 at these points. At φ=0° the pressure field is quite similar as the DC pressures are within 20bar at this point, but the pressure for 3600rpm, 450bar, 100% quickly rises in which a large difference is then seen at φ=45° in the pressure and fluid film thickness. At φ=180°the DC pressure for 3600rpm, 50bar, 100% falls much more gradually reaching the same pressure in the low pressure stroke at about φ=190°. Therefore, there is a large difference still at φ=180°.in the pressure and fluid film thickness as the DC pressure is largely different.

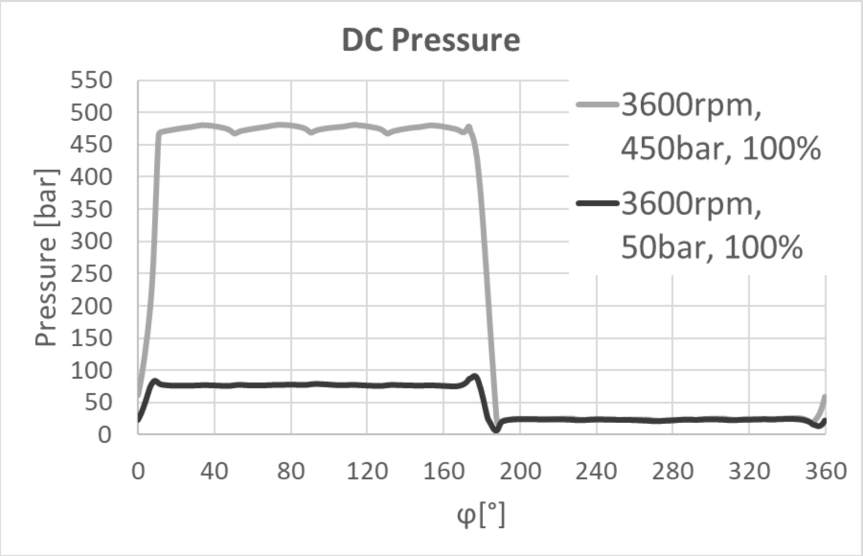

Figure 5.43. Baseline simulated multi-plots for pumping mode 3600rpm, 450bar, 20%, T_{in}=52°C.

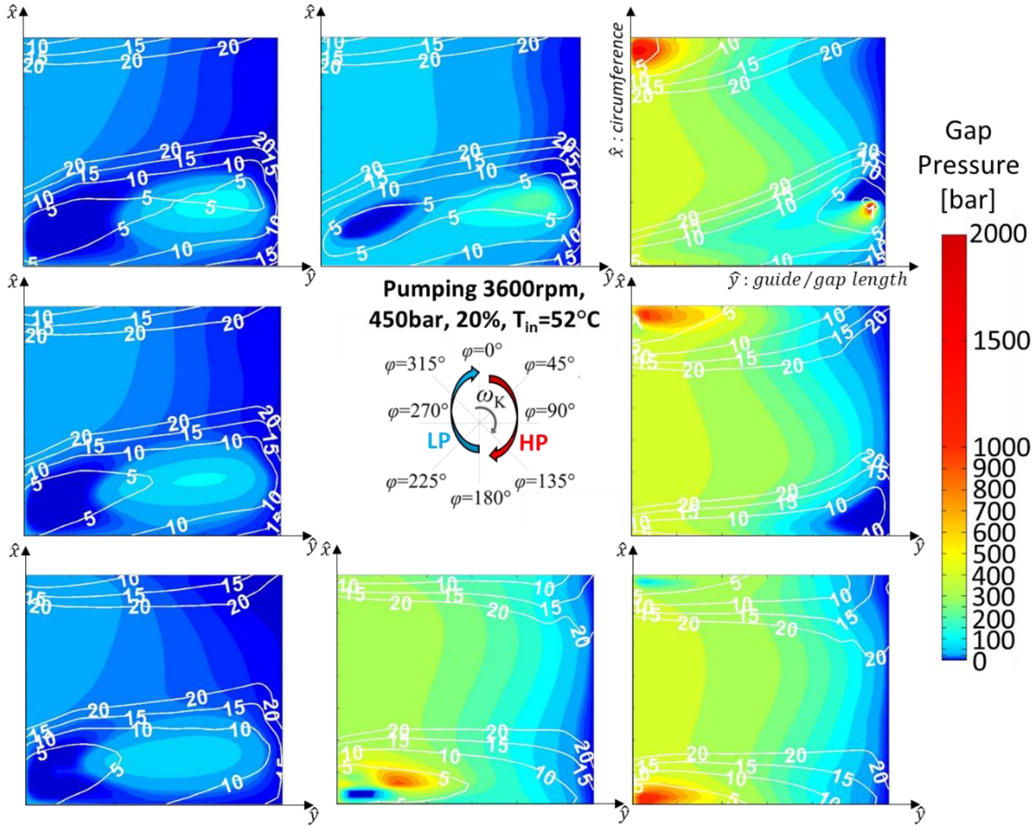

Figure 5.44. Baseline simulated multi-plots for pumping mode 3600rpm, 450bar, 20%, T_{in}=52°C.

Figure 5.44 depicts the fluid film for the case in which the operating displacement is decreased at a high speed, 3600rpm, and high pressure, 450bar, in pumping mode. It is clear that the stroke of the piston is reduced in which the gap is no longer variable near IDC. The resulting external load on the piston are decreased under such conditions which causes the piston to be less inclined in turn reducing the mechanical losses. However, this then results in the increase in volumetric losses as an abundant fluid film is created around the centered piston within the cylinder in which the fluid can easily flow out of the gap especially so at the high pressure.

From an overall perspective, as the operating pressure increases, increasing the external loads on the piston, the areas of critical minimum film in turn increase. Although the baseline unit is an existing machine known to operate, especially after run-in, the simulation shows slight occurrences of critical areas of minimum film thickness due to a coarse fluid grid chosen in the interest of computational expense. It is nevertheless crucial to analyze this phenomenon and ensure that these areas remain minimal; considerable critical areas could reveal a bad design that generates an insufficient fluid film leading to contact of the solid bodies resulting in wear or even catastrophic failure of the unit.

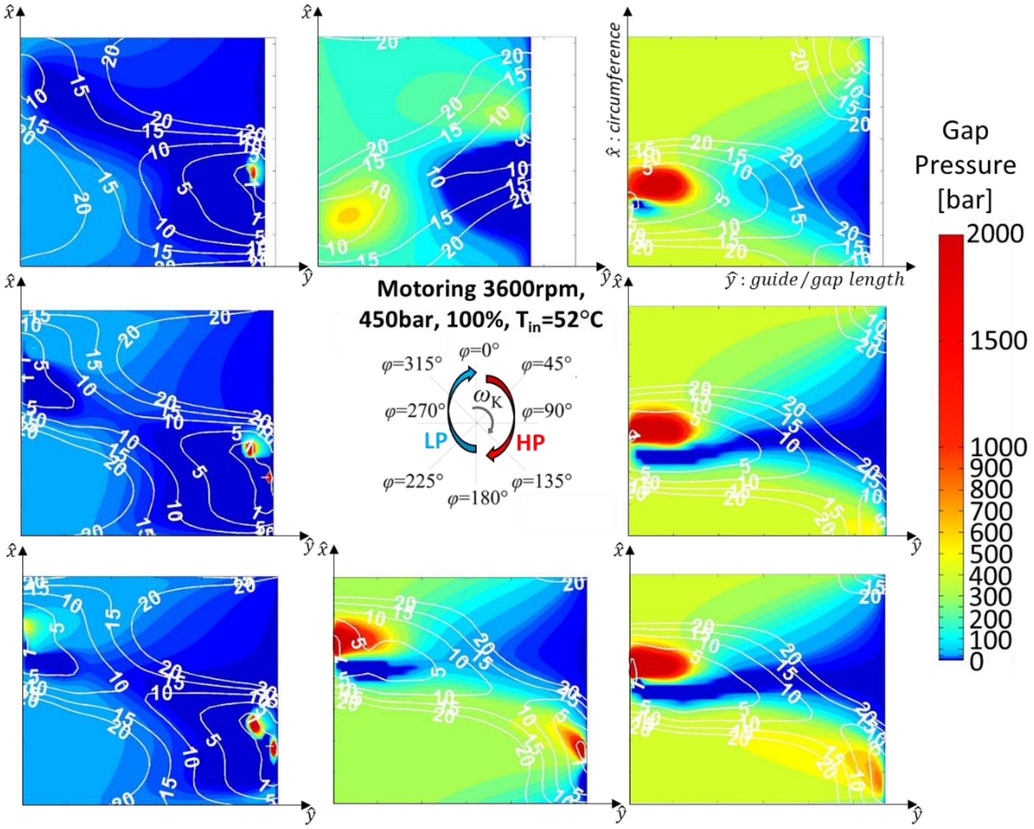

Figure 5.45. Baseline simulated multi-plots for motoring mode 3600rpm, 450bar, 100%, T_{in}=52°C.

A comparison to motoring mode is also made at the corner power operating condition of 3600rpm, 450bar, at full displacement as shown in Figure 5.45. Fundamentally the reversed motion of the piston is shown; the reduced gap length due to the piston at IDC occurs rather at 0° as the piston starts to move out of the bore during the high pressure stroke from 0° to 180°. At this operating condition, the resulting gap pressure field and fluid film thickness is comparable to pumping mode. The main difference that arises is eminent in the minimum fluid film thickness that occurs on the DC end as it obstructs the fluid required to build up the pressure to counteract the external loads on the piston leading to a tilted piston throughout the low pressure stroke. This results in a minor increase in mechanical losses as well volumetric losses occurring on the opposing circumference of the gap.

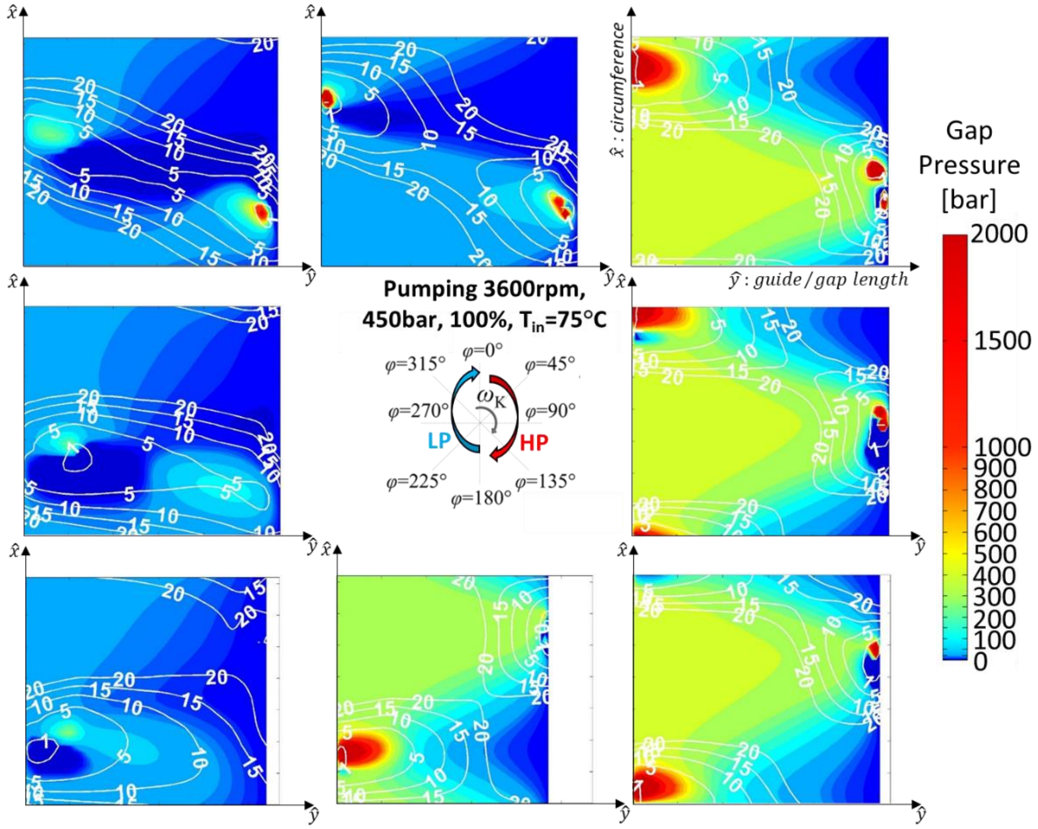

Figure 5.46. Baseline simulated multi-plots for pumping mode 3600rpm, 450bar, 100%, T_{in}=75°C.

Conclusively, a comparison to an increased inlet temperature of 75°C is made at the corner power operating condition of 3600rpm, 450bar, at full displacement, Figure 5.48, the difference between

52°C and 75°C inlet temperature shown in Figure 5.47. As the viscosity of the fluid is decreased as well as the gap temperature increased, the fluid film thickness as well as the areas of pressure build up slightly shifted. With this, a similar mechanical losses results. The variation occurs in the volumetric losses as they greatly increase with the decrease in fluid viscosity.

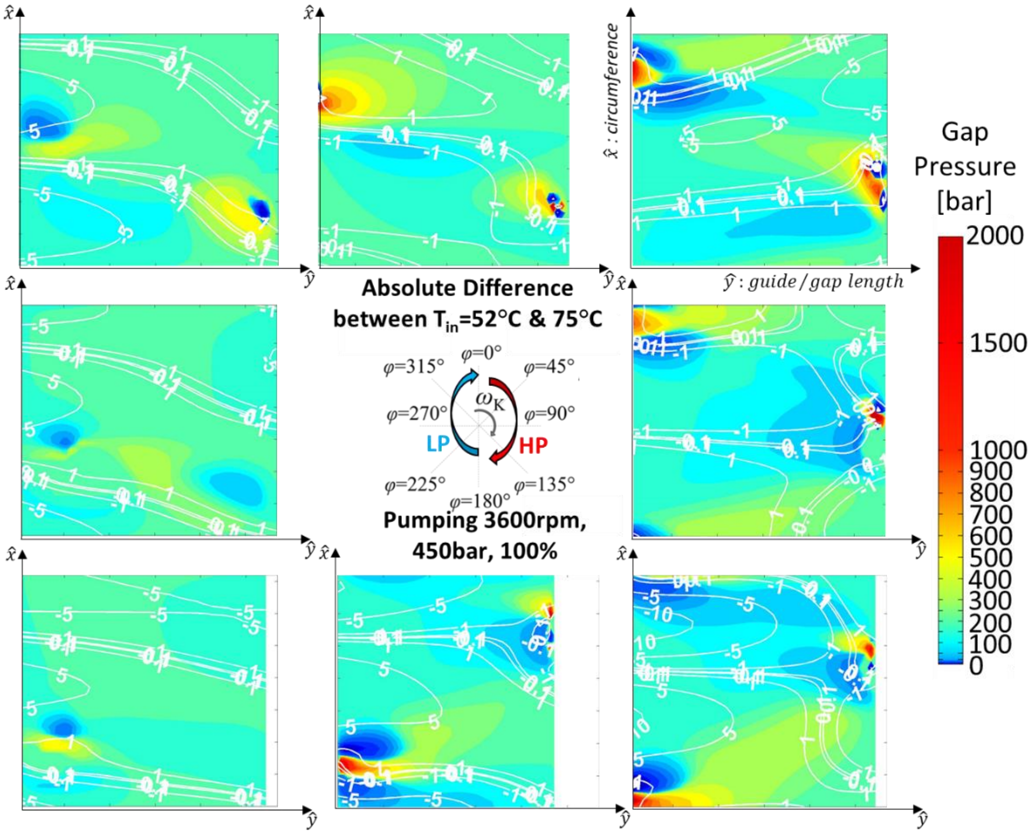

Figure 5.47. Baseline simulated multi-plots difference for pumping mode 3600rpm, 450bar, 100%, between T_{in}=52°C and T_{in}=75°C.

Multi-plots are also shown of the deformations for the most extreme operating condition effecting the fluid film, 3600rpm, 450bar, at full displacement in pumping mode. These plots show the magnitude of the combined deformations of the solid bodies due to pressure loading, Figure 5.48, and internal thermal stresses, Figure 5.49 and Figure 5.50, in the white contour lines with the corresponding pressure distribution and temperature field respectively underlying for 45°

increments over an entire revolution. A total positive deformation correlates to an increase in the fluid film thickness; a combination of the expansion of the bore and a contraction of the piston.

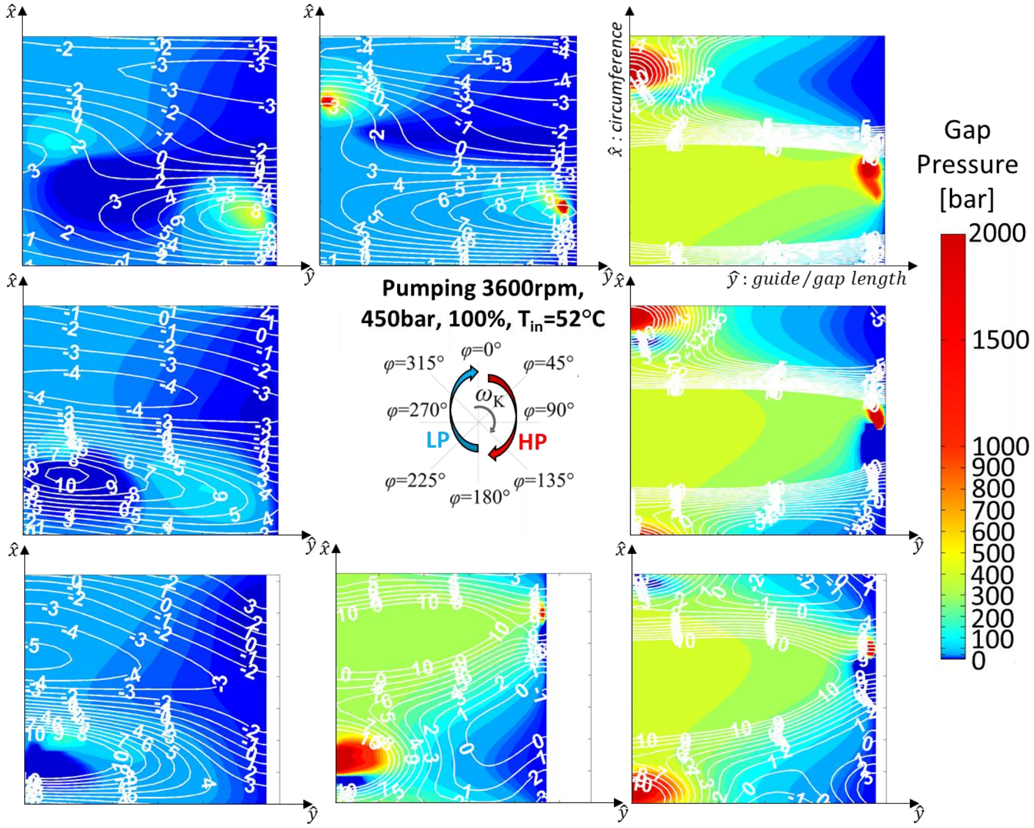

Figure 5.48. Baseline simulated pressure deformations for pumping mode 3600rpm, 450bar, 100%, T_{in}=52°C.

As can be seen in Figure 5.48, it follows that the large increases in the fluid film thickness due to the expansion of the bore and contraction of the piston occurs around the concentrated areas of increased pressure spikes that are necessary to support load; a maximum change in the fluid film of up to 10μm. Considerable deformation of the solid bodies also has an effect on the fluid film thickness along the circumferential channels of high pressure from the displacement chamber end created as the piston tilts within the bore. The deformations emanate out resulting in a decrease (negative contours) in the fluid film thickness in the areas of minimal pressure on the opposing circumferential side where the case pressure is present.

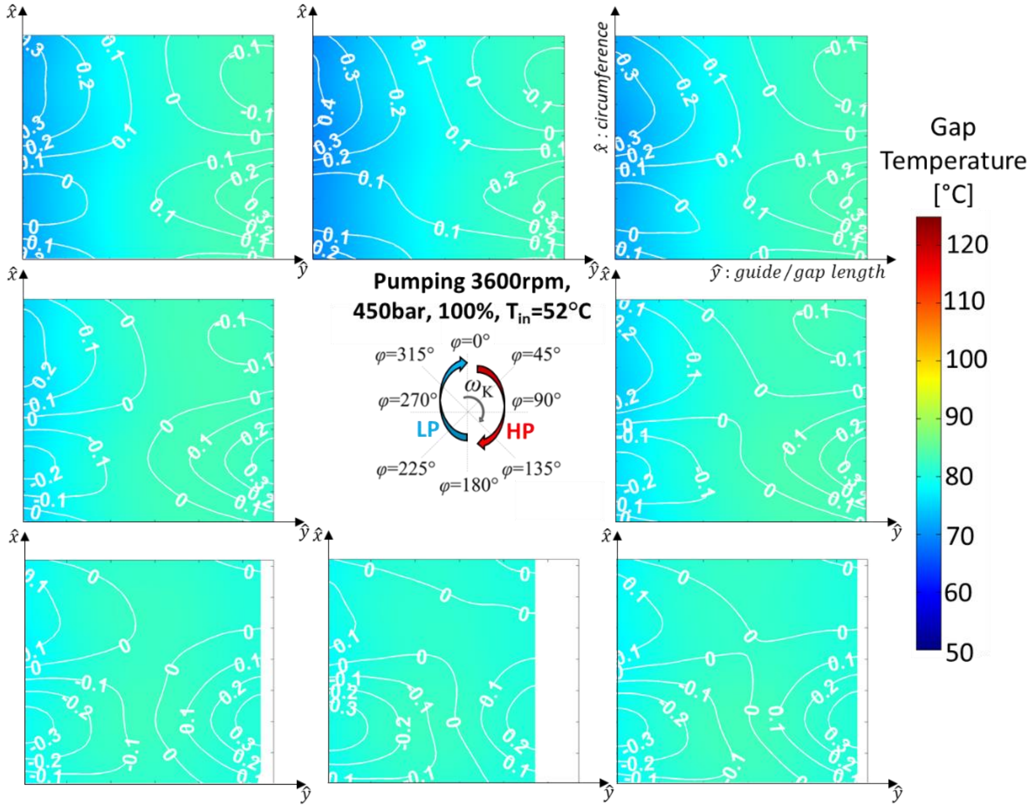

Figure 5.49. Baseline simulated thermal deformations for pumping mode 3600rpm, 450bar, 100%, T_{in}=52°C.

On the contrary, the deformations of the solid bodies due to internal thermal stresses, Figure 5.49, have a minimal effect on the fluid film thickness. The expansion of both solid bodies counteract the impact on the resulting fluid film thickness between the piston and the cylinder; a maximum of 0.3µm. As for the temperature distribution, the case fluid is hotter than that of the fluid in the displacement chamber that comes from the inlet and is discharged to the outlet in which a distribution between the two follows across the gap. These temperatures are dependent on the set boundary temperatures predicted as shown previously in the operating conditions Section 5.6.

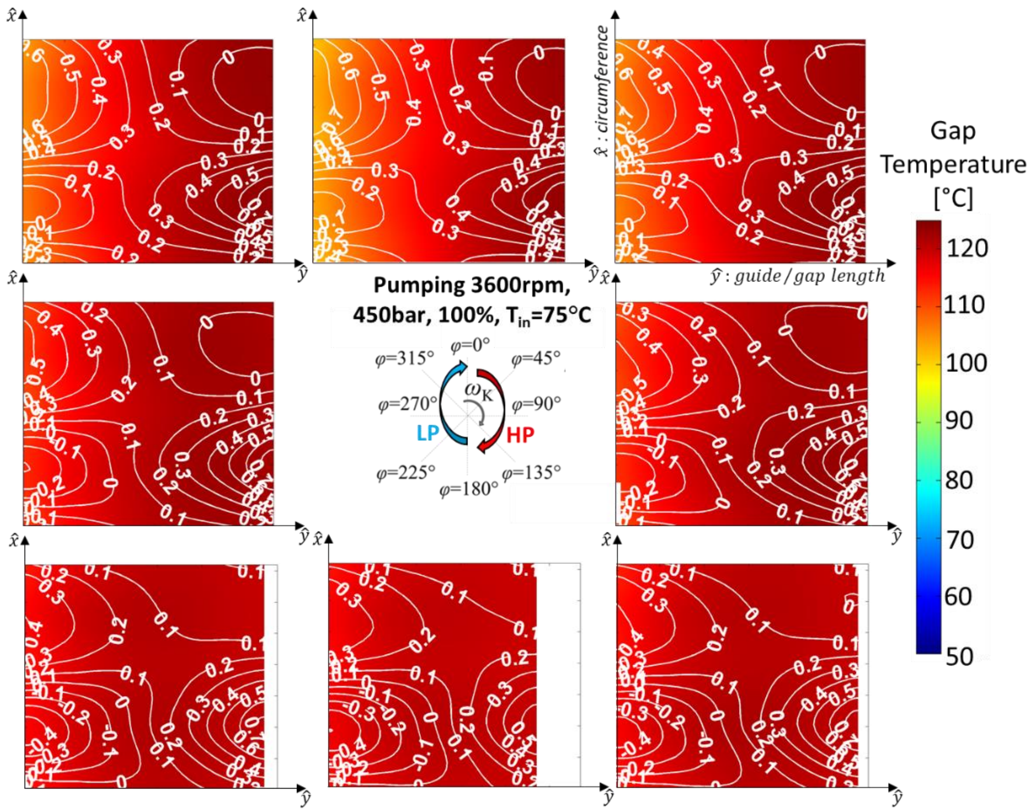

Figure 5.50. Baseline simulated thermal deformations for pumping mode 3600rpm, 450bar, 100%, T_{in}=75°C.

As the inlet temperature increases to 75°C, as shown in Figure 5.50, a large increase in the gap temperature can be observed. It still holds that the resulting expansion of both solid bodies counteract the impact on the resulting fluid film; a maximum of 0.7µm which is an increase of 0.4µm at the increased temperatures.

CHAPTER 6. INVESTIGATION OF PISTON MICRO-SURFACE SHAPING

Once an extensive analysis of the baseline was concluded utilizing an experimentally verified simulation tool, a broad investigation of the impact of micro-surface shaping of the piston/cylinder interface on the performance had been conducted. The goal of this research study was to comprehensively investigate the effects of micro-surface shaping on the piston through virtual prototyping over a wide range of operating conditions. Therefore, to not only understand the effects of the design principles on the lubricating film, but also how it impacts the efficiency, performance, and reliability of the unit.

The following study considers the micro-surface shapes implemented on a nominal piston as detailed in CHAPTER 4 at a reduced clearance of 58.8% of the baseline design studied at the corner operating conditions. In order to quantify the improvements of surface shaping as well as show the trends between the designs, the results are compared to the baseline design as described in CHAPTER 5 considering the measured wear profile as shown in Figure 5.6. It will be established that micro-surface shaping of the piston can provide additional load support that is generated through intentional manipulation of the fluid film at reduced clearances allowing for better efficiencies. The trends detailed will be useful for future design of the piston/cylinder interface.

6.1 Pumping

In order to understand how the surface shaping of the piston effects the phenomenon occurring within the gap, various examples are shown of the resulting fluid film thickness and the pressure field for the various designs at the corner operating conditions. The following multi-plots show the fluid film thickness in white contour lines and the corresponding fluid film pressure in the colored contour for an unwrapped gap of a single shaft angle.

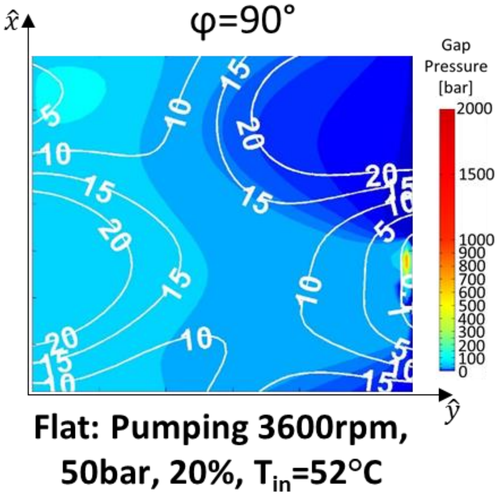

Figure 6.1. Sinusoidal wave simulated multi-plot for pumping mode 3600rpm, 50bar, 20%, T_{in}=52°C; φ=90°.

Regarding the sinusoidal piston micro-surface wave, this design tends have slight issues at partial displacement operating conditions. According to Figure 6.1, there is a small area of critical fluid film that occurs on the case end in the high pressure stroke at the peak of the sine wave, but the fluid pressure is built up in that area in order to aid in the fluid support. This pressure build up is possible at partial displacements as the piston is not as tilted within the bore.

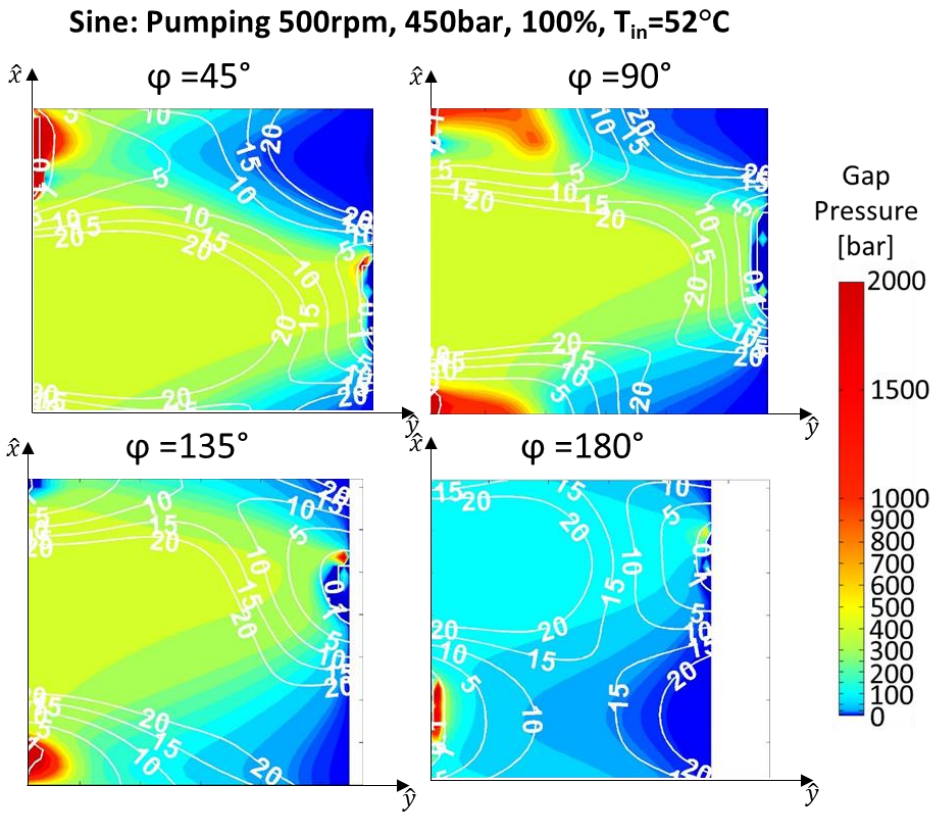

Figure 6.2. Sinusoidal wave simulated multi-plot for pumping mode 500rpm, 450bar, 100%, T_{in}=52°C; φ=90°(left), φ=180°(right).

Problems also tend to arise at full displacement operating conditions with the sinusoidal wave design, especially so at low speed and high pressure, the most challenging operating condition in terms of fluid support, as the external loads are no longer supported by the build-up of pressure in the fluid film as can be seen in Figure 6.2. Areas of minimum fluid film are occurring on both the case end of the gap and DC end of the gap, however the pressure build-up is nonexistent. This is due to the peaks of the sine wave developing concentrated areas of minimal fluid film blocking off the fluid to the gap resulting in the inability to produce additional fluid load support.

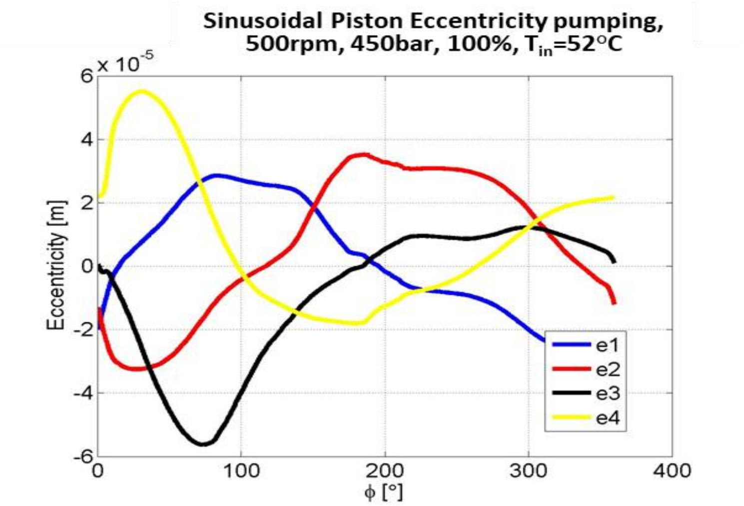

Figure 6.3. Sinusoidal wave simulated eccentric position for pumping mode 500rpm, 450bar, 100%, T_{in}=52°C.

Further support of this phenomenon is shown in the eccentric position of the piston within the bore in Figure 6.3 (eccentric positions as shown in Figure 2.4). Eccentricity 3 and 4, on the case end, go to the limit of the clearance since the fluid support is not present to counteract the external forces.

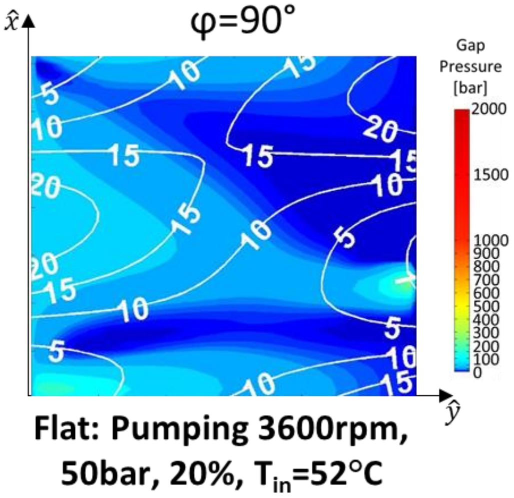

Figure 6.4. Flat simulated multi-plot for pumping mode 3600rpm, 50bar, 20%, T_{in}=52°C; φ=90°.

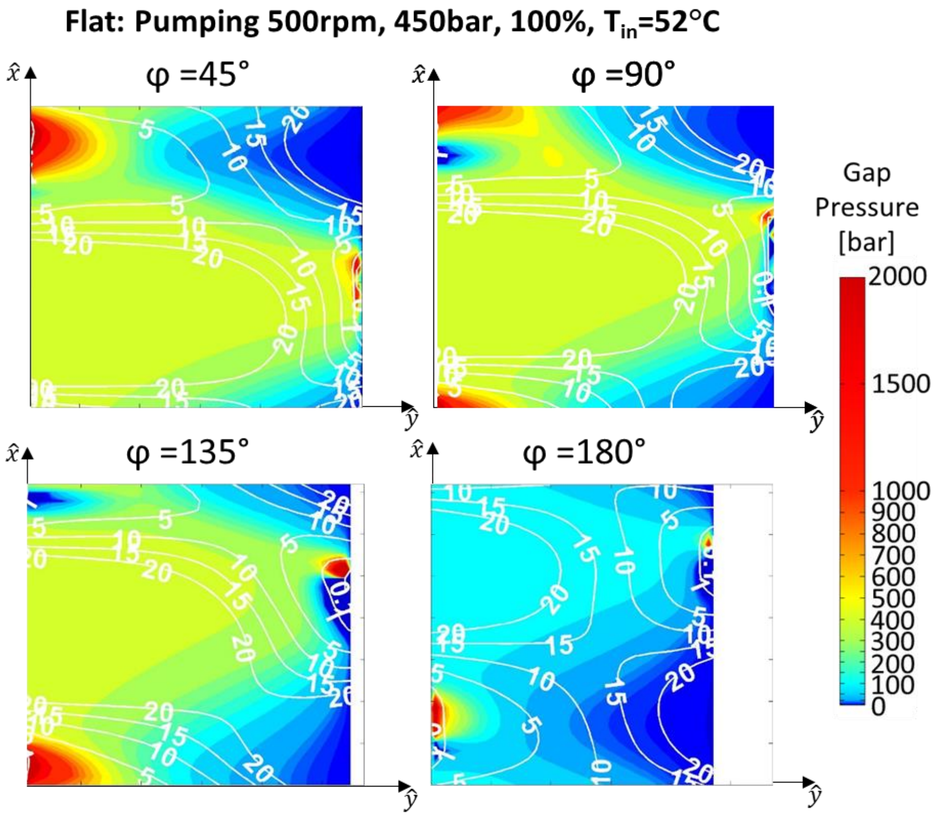

Figure 6.5. Flat simulated multi-plot for pumping mode 500rpm, 450bar, 100%, T_{in}=52°C; φ=90°(left), φ=180°(right).

On the contrary, the flat micro-surface shape of the piston results in superior load support over the range of operating condition in comparison. An example is again shown for both partial displacements, Figure 6.4 and full displacements, Figure 6.5.At partial displacements, the piston is more centered in the bore in which critical areas do not occur. As for full displacement condition, some critical areas still occur, but the pressure build up behind the piston aids in the fluid support, especially so on the case end. Fluid support is achieved as the small deviation at ends allows piston to tilt enough within the bore while the cylindrical length of the piston aids in the pressure build-up required to balance the external loads subjected on the piston.

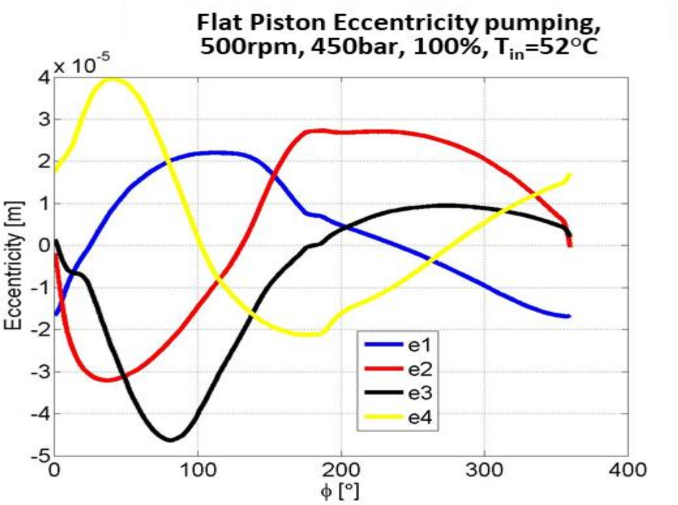

Figure 6.6. Flat simulated eccentric position for pumping mode 500rpm, 450bar, 100%, T_{in}=52°C.

Again, further support of this phenomenon is shown in the eccentric position of the piston within the bore in Figure 6.6 (eccentric positions as shown in Figure 2.4). Eccentricity 3 and 4, on the case end, are much lower at the beginning of the high pressure stroke. So although the piston still tilts within the bore due to the higher external forces at the higher pressure operating condition, the piston is supported by the pressure build up within the fluid.

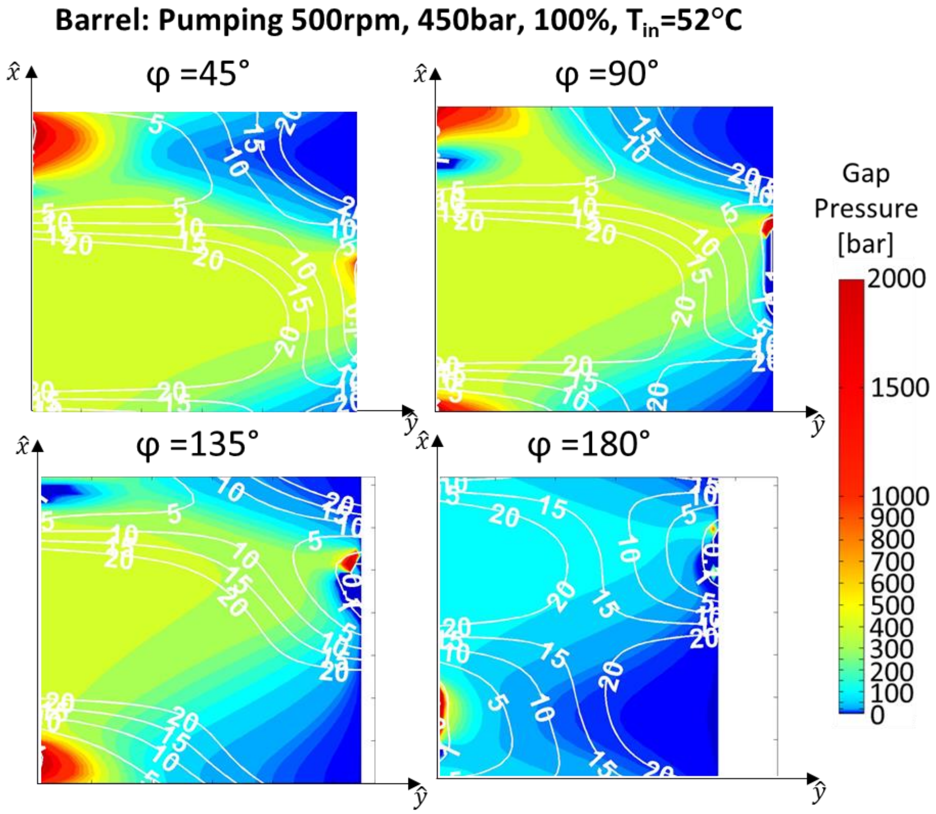

Figure 6.7. Barrel simulated multi-plot for pumping mode 500rpm, 450bar, 100%, T_{in}=52°C; φ=90°(left), φ=180°(right).

Likewise for the barrel surface profile, fluid support is rather sufficient for the range of operating conditions investigated in pumping mode. Partial displacement behaves very similarly to that shown for the flat profile in which is it not shown as the piston is more centered in the bore not requiring major fluid support. As for full displacements, the fluid support is even better, Figure 6.7. The pressure build up on the case end is slightly larger resulting in an even smaller area of critical film thickness. The benefit to this design is that at the reduced clearance the gradual deviation along the length of the piston allows for the ability of the piston to gradually incline as it axially reciprocates in bore building up fluid support through a squeeze effect especially when needed at full displacements and high pressure operating conditions.

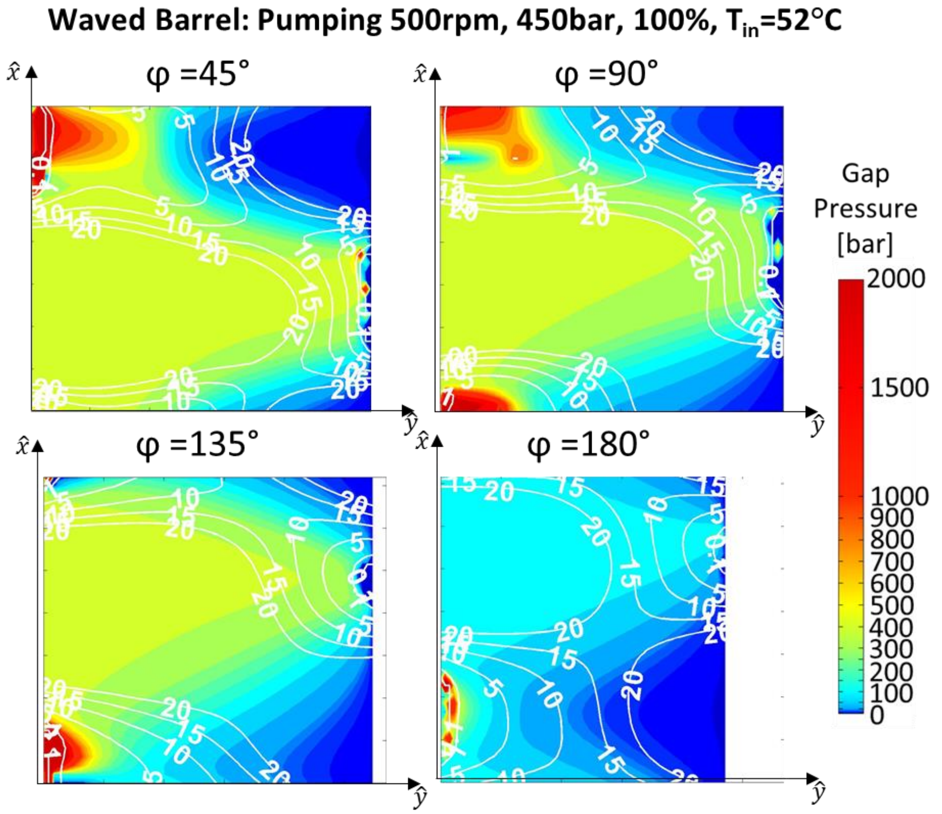

Figure 6.8. Waved barrel simulated multi-plot for pumping mode 500rpm, 450bar, 100%, T_{in}=52°C; φ=90°(left), φ=180°(right).

The combination of the sinusoidal wave and the barrel surface profile, the waved barrel has similar complications to that of the sinusoidal wave design. As the barrel aspect allows the piston to tilt within bore, the peaks of the sine wave result in concentrated areas of critical film thickness, Figure 6.8, which in turn cuts off the fluid to the gap not allowing for the build-up of the required fluid film pressure to support the load.

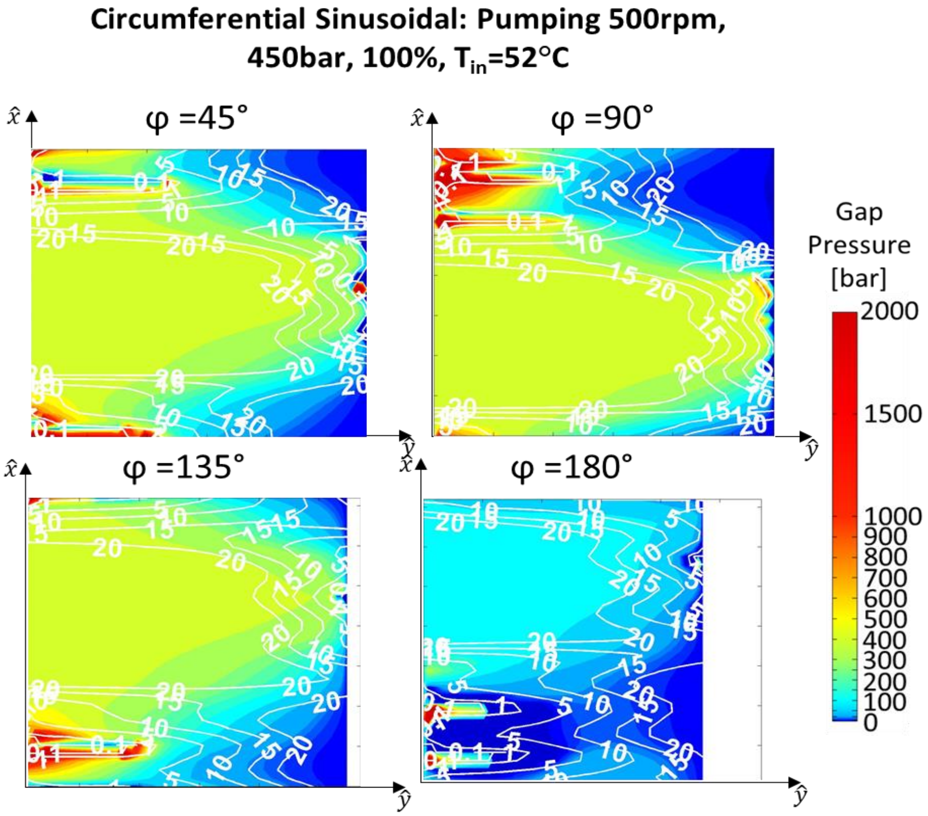

Figure 6.9. Circumferential sinusoidal wave simulated multi-plot for pumping mode 500rpm, 450bar, 100%, T$_{in}$=52°C; φ=90°(left), φ=180°(right).

The final design, the circumferential sinusoidal wave, tends to perform the worst in terms of fluid support and minimal areas of critical fluid film thickness, Figure 6.9. Similarly to the designs with an axial sinusoidal wave, the peaks of the wave result in concentrated areas of critical film thickness at full displacements where the side load on the piston is higher. However, with this design, these areas of critical film thickness appear along the length of the peak. This results in the most critical film areas throughout the high pressure stroke among the designs, especially so on the DC end of the gap. Furthermore, this design lacks a deviation at the ends of the piston in which the piston cannot tilt as much within the bore as it reciprocates in and out of the bore.

A comprehensive fluid film support analysis over the wide range of corner operating conditions studied is shown below. The correction forces, Figure 6.10, along with the maximum percent area of the gap below a minimum fluid film thickness of 0.1μm, Figure 6.11, are shown as supporting evidence. The maximum percent area of the gap below minimum fluid film thickness is simply the maximum number of cells at any given shaft position throughout an entire revolution below the defined minimum film thickness divided by the number of cells defining the fluid grid. Ideally, this percentage should be zero such that areas of critical film thickness do not occur over an entire revolution in which the fluid film will support the external loads acting on the piston to prevent any contact from occurring between the solid bodies signifying full film lubrication. The correction forces are defined as the forces required additional to that of the fluid pressure in order to prevent the piston from penetrating below minimum film thickness; shown as an average over a revolution on both the case and the DC end of the gap. These forces should be very minimal, but are occasionally required in simulation since the fluid grid is coarse in the interest of time; a better design will still reduce these forces as the pressure distribution in the fluid is sufficient to support the load.

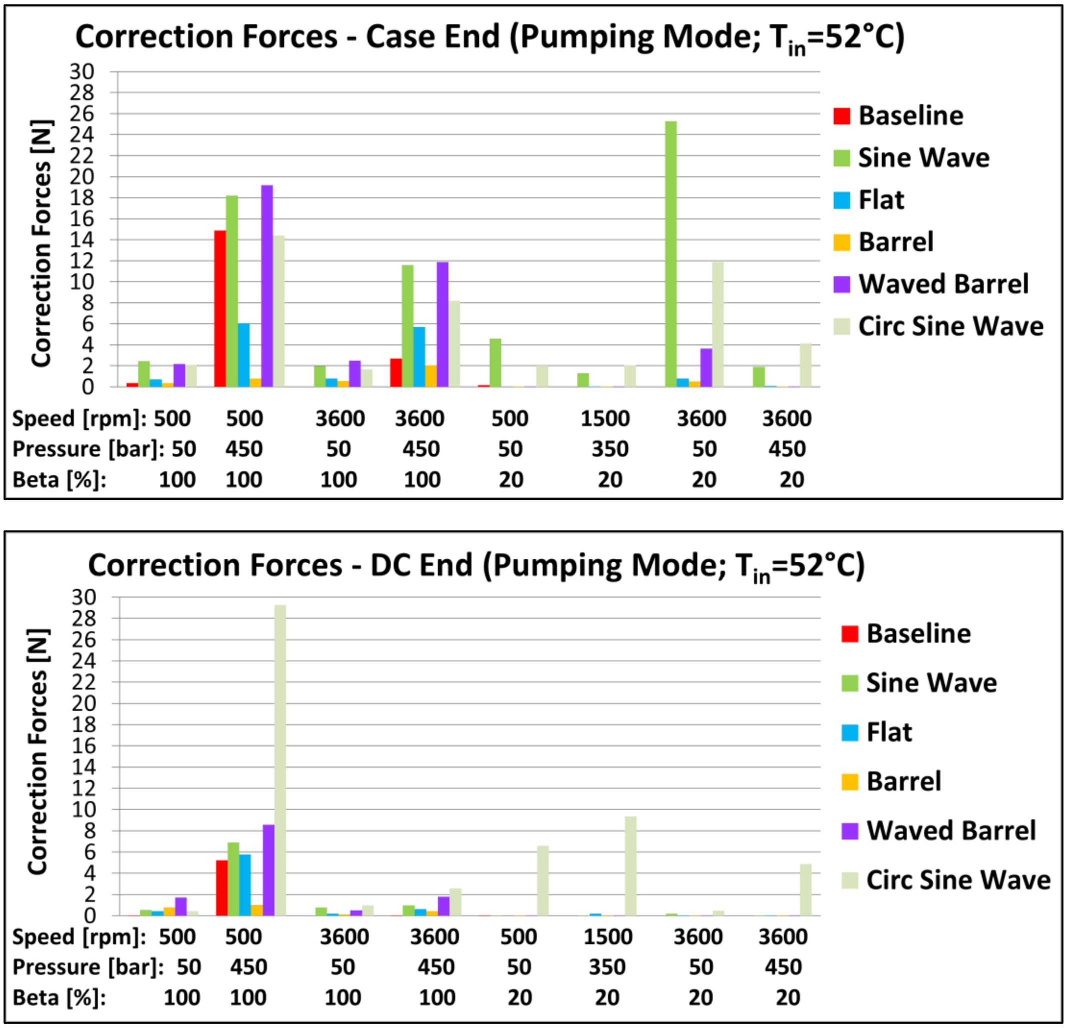

Figure 6.10. Correction forces for case end (top) and DC end (bottom); pumping mode, T_{in}=52°C.

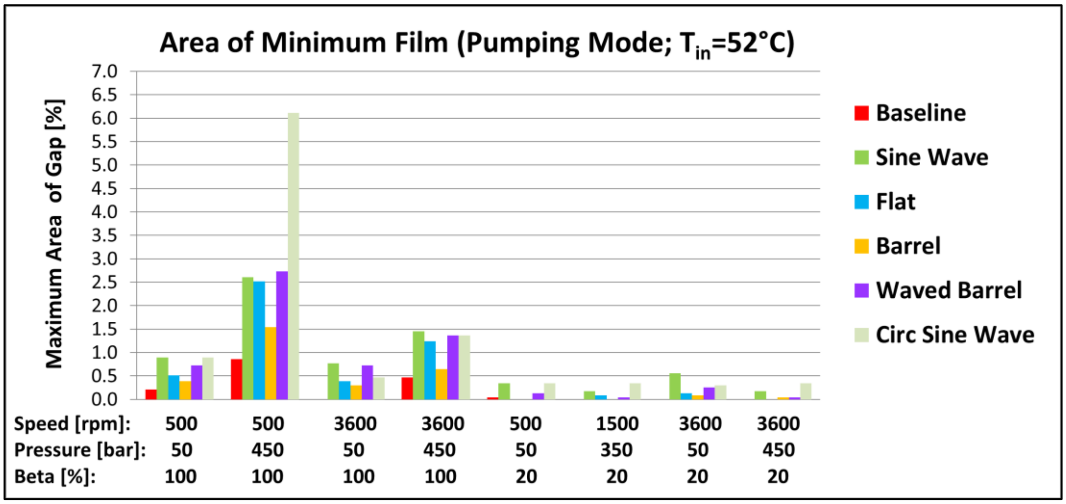

Figure 6.11. Maximum percent area of the gap below the minimum fluid film thickness over an entire revolution; pumping mode, T_{in}=52°C.

According to the fluid support criteria as shown in Figure 6.10 and Figure 6.11, there is minimal complication of load support at partial displacement operating conditions due to the reduced side loads. Nevertheless, the sinusoidal wave, waved barrel, and circumferential sinusoidal waves still have some trouble that occurs at the peaks of the sine waves. In terms of low pressure conditions, it seems that although the correction forces are minimal, slight areas of critical fluid film still tend to occur as the piston lightly slides along the bushing, not tilting. As for the high pressure operating conditions at full displacement, the fluid support required increases. Overall the flat piston at a reduced clearance is relatively comparable to the baseline while the barrel profile performs even better in terms of the correction forces.

Once the phenomenon occurring within the fluid film is understood due to the various designs of piston surface shaping, the effect on the overall efficiency can be evaluated. Based on the resulting fluid film between the piston and the cylinder, the decrease in energy dissipation and corresponding leakage due to micro-surface shaping of the piston at a reduced clearance in comparison to the baseline, wear-in design (Figure 5.6) for the corner operating conditions in pumping mode are shown in Figure 6.12 and Figure 6.13 respectively.

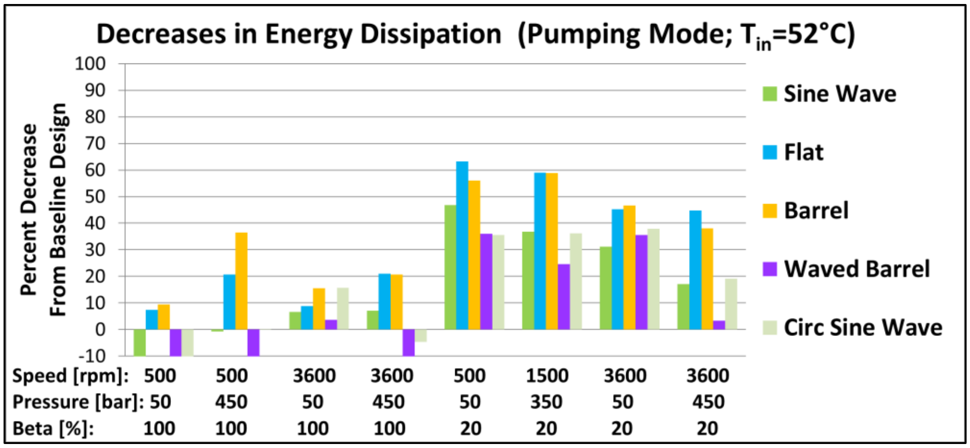

Figure 6.12. Decrease in energy dissipation due to micro-surface shaping of the piston; pumping mode, T_{in}=52°C.

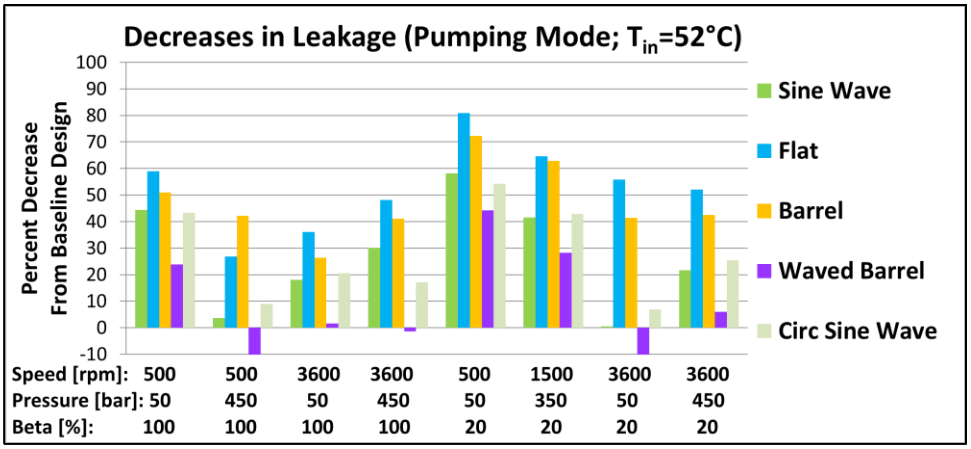

Figure 6.13. Decrease in leakage due to micro-surface shaping of the piston; pumping mode, T_{in}=52°C.

Surface shaping of the piston can result in over a 60% decrease in overall energy dissipation due to a corresponding 80% decrease in leakages. The tremendous reduction in leakage is mainly due to the reduction in the relative clearance between the piston and the bushing; 58.8% of the nominal baseline. The micro-surface shaping of the piston for the five various designs investigated is shown to have a much larger impact at partial displacements due to the significant reduction in leakages without greatly increasing the torque losses. In the case of full displacement especially at low pressures, the leakages are also greatly reduced, but this is not as reflected in the energy dissipation since the torque losses are in turn increased at the reduced clearance in which the fluid pressure does not balance the load as well.

As for the designs with a sinusoidal wave, on top of insufficient fluid support resulting in areas of critical film thickness leading to the generation of torque losses, the troughs of the wave traps fluid and pulls it out of gap with the reciprocating motion of piston. Therefore, the leakages are not as greatly decreased and in turn reflected in the energy dissipation. Additionally, for the combination of the waved barrel the reduced radii at both ends adds to the leakage from the gap. On the other hand, the flat surface profile not only supports the load better, but also results in a considerable reduction in leakages significantly impacting the reduction in overall energy dissipation, over a 60% reduction. The reason for this is due to the smallest minimum radial clearance along the cylindrical length of the gap at the reduced clearance among the designs studied. Finally, the barrel design results in the best fluid support among the designs however, the larger surface deviation along the axial direction of the piston allows for more leakage than that of the flat design, leading to a slightly less reduction in energy dissipation of up to 55%. Overall the reduction in the energy dissipation for the barrel design highly depends on the reduction in leakages at the reduced clearance while not greatly increasing torque as fluid support is still developed.

Conclusively, the addition of a micro-surface profile on the piston can allow for the reduction in clearance, but this reduction must be balanced between the decrease in leakage and the increase in torque loss while still balancing the external loads acting on the piston by generating fluid pressure.

6.2 Motoring

The decrease in energy dissipation and corresponding leakage due to micro-surface shaping of the piston at a reduced clearance in comparison to the baseline, cylindrical design for the corner operating conditions in motoring mode are shown in Figure 6.14 and Figure 6.15 respectively.

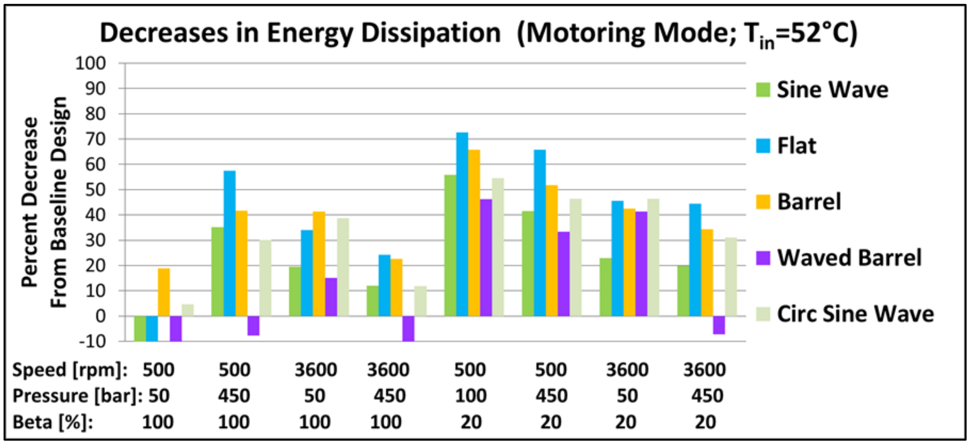

Figure 6.14. Decrease in energy dissipation due to micro-surface shaping of the piston; motoring mode, T_{in}=52°C.

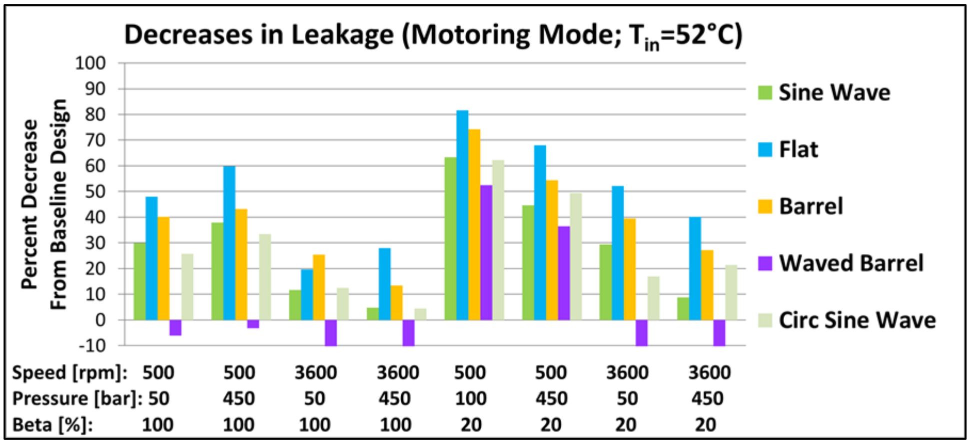

Figure 6.15. Decrease in leakage due to micro-surface shaping of the piston; motoring mode, T_{in}=52°C.

For motoring mode, similar trends to those shown in pumping mode between the surface profiles at the corner operating are apparent. This is expected since the forces acting on the piston are similar, only differing as the motion of the piston is reversed. Since in motoring mode, the piston moves out of the bore in the high pressure stroke the Couette component opposes this motion in which the Poiseuille component then aids in reducing the overall friction forces. Under such conditions, the flat surface profile still greatly reduces the energy dissipation of the interface by up to 70% correspondingly due to the large reduction in leakages as the clearance is reduced. However, it again follows that the flat surface profile does not develop as much fluid support at full displacements as can be seen in Figure 6.16 and Figure 6.17. Consequently, it follows that the barrel is the best profile as it reduces the energy dissipation up to 65% while still supporting the loads as it tilts within the bore. Likewise, it can be observed in motoring mode that the overall reduction in energy dissipation strongly relies on the large reduction in leakage considering fluid support is still generated due to the piston surface shaping at the reduced clearance.

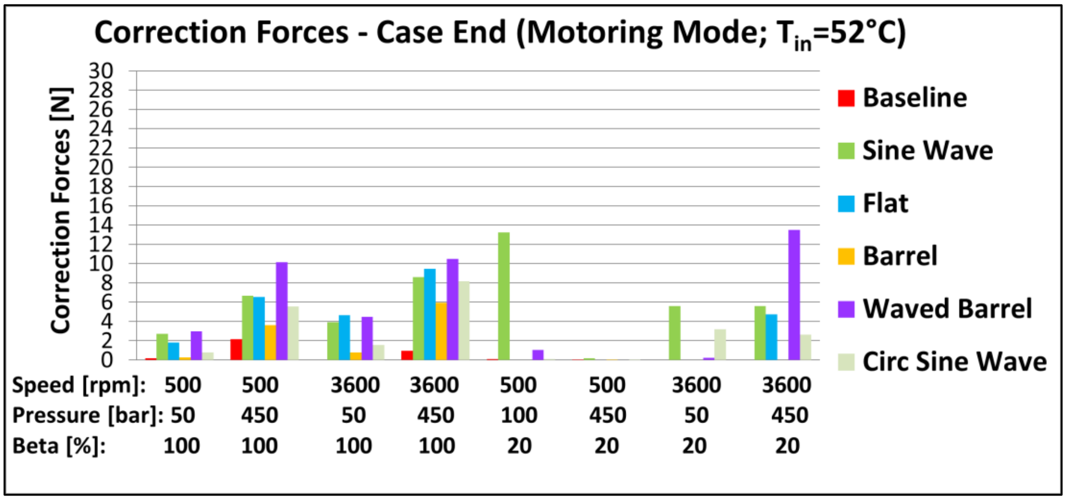

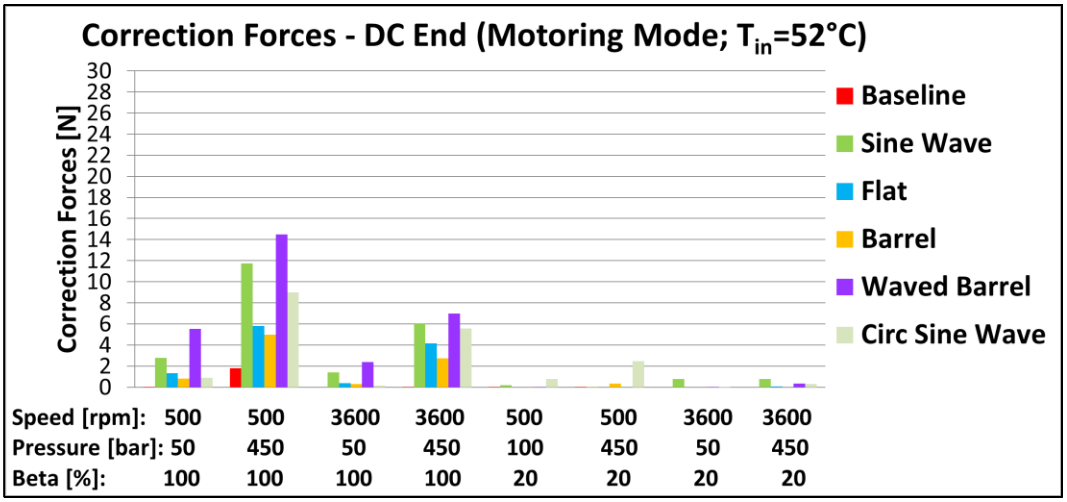

Figure 6.16. Correction forces for case end (top) and DC end (bottom); motoring mode, T_{in}=52°C.

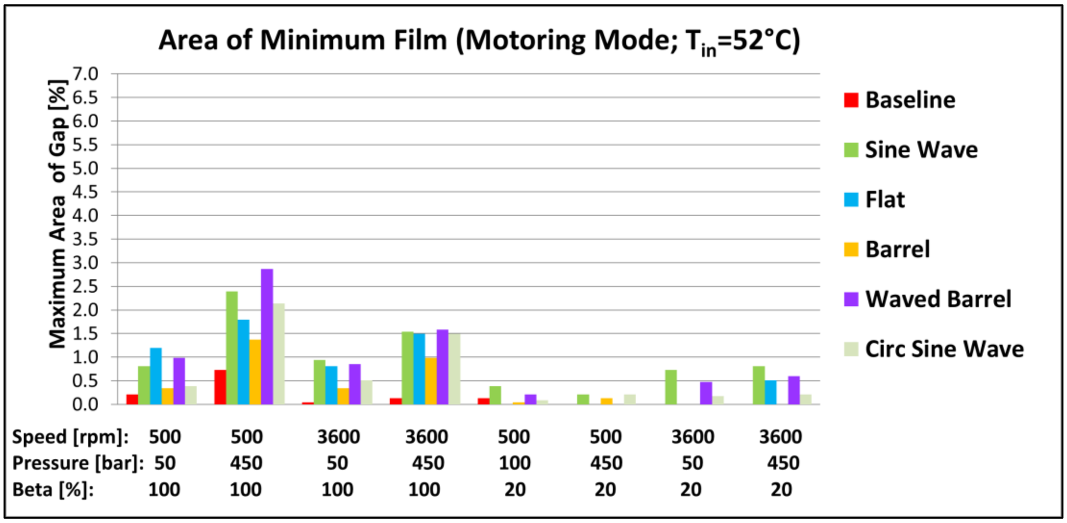

Figure 6.17. Maximum percent area of the gap below the minimum fluid film thickness over an entire revolution; motoring mode, T_{in}=52°C.

Similar trends in the fluid support criteria as shown in Figure 6.16 and Figure 6.17 are noted among the operating conditions between the surface profiles for motoring mode as was demonstrated for pumping mode. Although, for motoring mode the correction forces tend to be slightly shifted to the DC end from the case end for high pressure operating conditions. Also, the profiles incorporating a sinusoidal wave do not result in such depreciated fluid support for some cases as was shown in pumping mode.

6.3 Clearance Study of Piston Surface Shaping

Not only does the micro-surface shape on the piston play a role on the performance of the interface, but the clearance between the piston and the cylinder also has a major impact. In the initial study, a constant reduced clearance of 55.8% of the nominal design was considered. It was established that a reduction in the clearance was possible due to the surface shaping on the piston in which a balance between the sealing and bearing function of the interface must be maintained. Therefore, it was then necessary to investigate the influence of the clearance parameter. In this study a range of clearances, 88.2%, 73.5%, 58.8%, 44.1%, and 29.4% of the nominal design were observed.

The resulting simulated losses of all nine piston/cylinder segments will be presented as a consequent of the micro-surface shaping on the piston over a range of reduced clearances at the corner operating conditions in both pumping and motoring mode. In the plots, each surface profile investigated, from CHAPTER 4, is denoted by line color: sinusoidal wave - green, flat – blue, barrel – orange, waved barrel – purple, circumferential sinusoidal wave – teal. The operating conditions are then denoted by the marker symbols: ● - 500rpm 50bar, ■ - 500rpm 450bar ♦ - 3600rpm 50bar, ▲ - 3600rpm 450bar. The clearance is varied for each design at each operating condition across the x-axis of the plots.

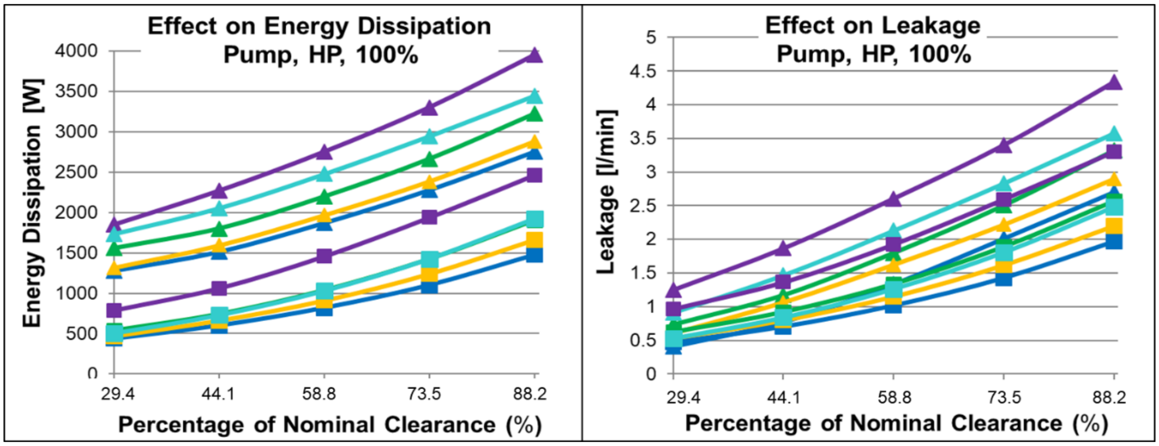

Figure 6.18. Energy dissipation (left) and corresponding leakage (right) due to micro-surface shaping of the piston at reduced clearances for pumping mode, high pressure, full displacement, T_{in}=52°C.

Figure 6.18 displays the energy dissipation on the left and the corresponding leakages on the right for high pressure operating conditions at full displacement in pumping mode at an inlet temperature of 52°C. At high pressure operating conditions (■ and ▲ markers) the energy dissipation decreases as the clearance is further reduced following the large reduction in leakages since in turn, the torque is not largely increasing.

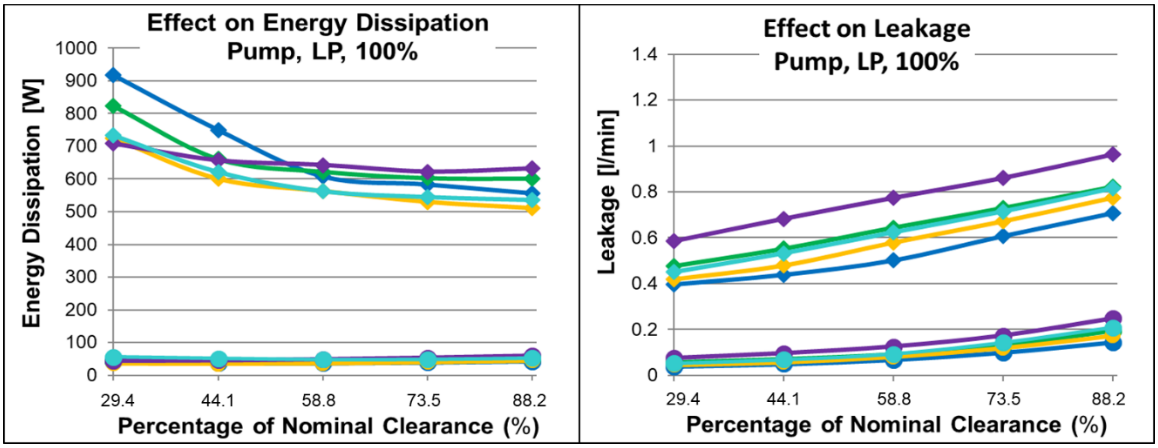

Figure 6.19. Energy dissipation (left) and corresponding leakage (right) due to micro-surface shaping of the piston at reduced clearances for pumping mode, low pressure, full displacement, T_{in}=52°C.

However, the trend is reversed at low pressure operating conditions (● and ♦ markers). Under low pressure conditions, the energy dissipation is decreased with larger clearances rather. Despite the fact that the leakages are slightly increased with larger clearances, the torque losses are more so reduced leading to reduction in overall energy dissipation. However, at the larger clearances, the surface profiles tend to no longer have a notable effect. This is especially true at the low speed and low pressure conditions where the resulting losses are minimal in which the impact then appears imperceptible.

Among the five surface profiles studied, the flat (blue line) and the barrel (orange line) surface shaped pistons do best at further reduced clearances, especially so at higher pressure operating conditions. Although a large reduction in energy dissipation is observed due to the reduction in leakages at high pressure, the torque losses start to have a significant effect at low pressure operating conditions as the clearance is further reduced with the flat piston. Therefore, a compromise at 58.8% reduced clearance is best overall with this profile. On the other hand, the barrel piston does not generate this increase in torque losses so drastically at a further reduced clearance for low pressure operating conditions in which it performs best overall at a 44.1% reduced clearance. Since the barrel allows for a slightly further reduced clearance of 44.1%, the leakages are even further reduced reflecting in the overall energy dissipation becoming less than that of the flat design at 58.8% of the clearance. The sinusoidal wave (green line), waved barrel (purple line), and circumferential sinusoidal wave (teal line) result in much higher leakage and torque losses in comparison leading to the lowest reduction in energy dissipation at the reduced clearances. For this reason, these designs are not feasible in comparison to the alternative designs.

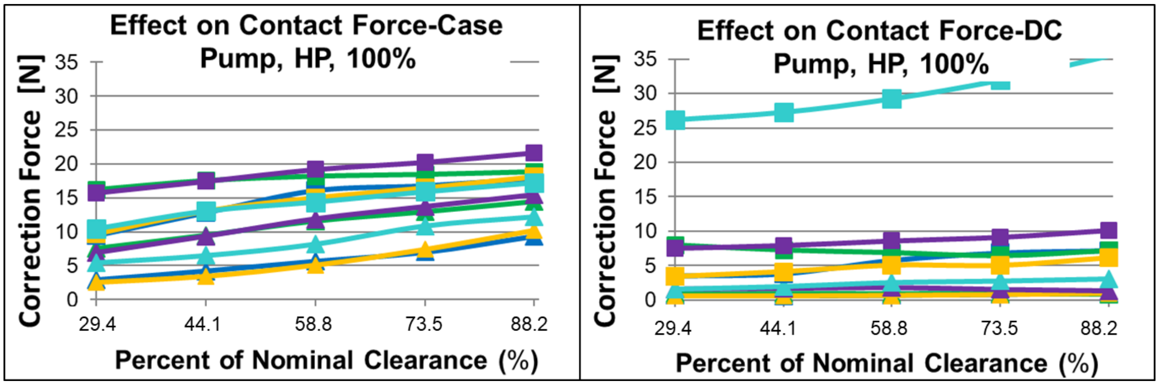

Figure 6.20. Correction forces for case end (left) and DC end (right); pumping mode, high pressure, full displacement, T_{in}=52°C.

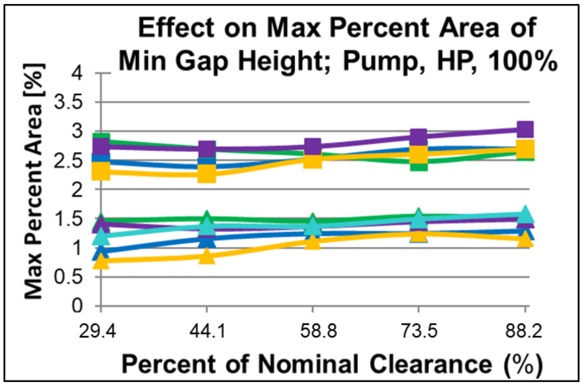

Figure 6.21. Maximum percent area of the gap below the minimum fluid film thickness over an entire revolution; pumping mode, high pressure, full displacement, T_{in}=52°C.

Analyzing the fluid support criteria, Figure 6.20 and Figure 6.21 for high pressure operating conditions (■ and ▲ markers), the required additional correction forces to support the load decline as the clearance is reduced, especially so on the case end where the majority of the aid is needed. However, the clearance does not tend to have a large effect on the areas of critical film thickness occurrence. Over the length of the gap, the barrel tends to be slightly better at generating fluid support than that of the flat profile while the profiles incorporating a sinusoidal wave result in the least fluid support. The benefit of the barrel piston is that the gradual deviation to the ends allows the piston to tilt within the bore, manipulating the fluid film geometry at the reduced clearance generating a sufficient fluid support.

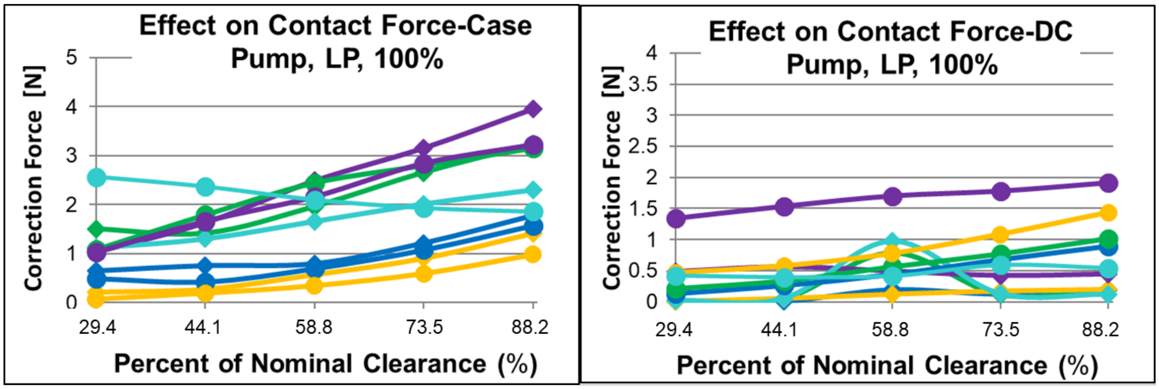

Figure 6.22. Correction forces for case end (left) and DC end (right); pumping mode, low pressure, full displacement, T_{in}=52°C.

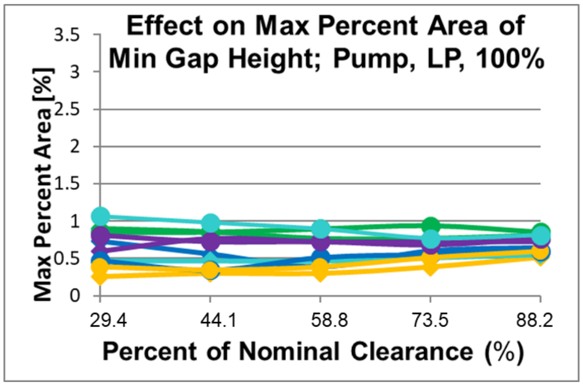

Figure 6.23. Maximum percent area of the gap below the minimum fluid film thickness over an entire revolution; pumping mode, low pressure, full displacement, T_{in}=52°C.

At low pressure operating conditions (● and ♦ markers) there are minimal issues that arise, Figure 6.22 and Figure 6.23, as the load support required is less due to the lower external side loading of the piston. The magnitude of the correction forces as well as the area of minimum gap height are much less under such conditions. The same trend follows that the correction forces on the case end are reduced with the reduction in clearance with the flat doing well and the barrel performing even better in terms of reliability.

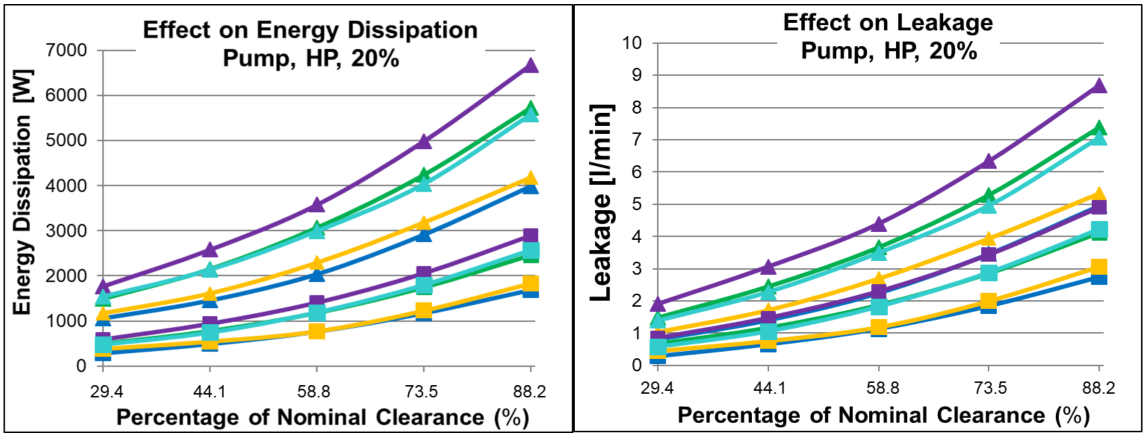

Figure 6.24. Energy dissipation (left) and corresponding leakage (right) due to micro-surface shaping of the piston at reduced clearances for pumping mode, high pressure, partial displacement, T_{in}=52°C.

Figure 6.24 displays the energy dissipation on the left and the corresponding leakages on the right for high pressure operating conditions at partial displacements in pumping mode at an inlet temperature of 52°C. At partial displacements, the external forces acting on the piston are not as pronounced in which the piston then does not tilt as much in the bore which compromises the sealing function in turn for lower forces to support. By reducing the clearance at high pressures (■ and ▲ markers), the leakages can be greatly reduced and is strongly reflected in the overall energy dissipation as the torque loss is rather unaffected at high pressures.

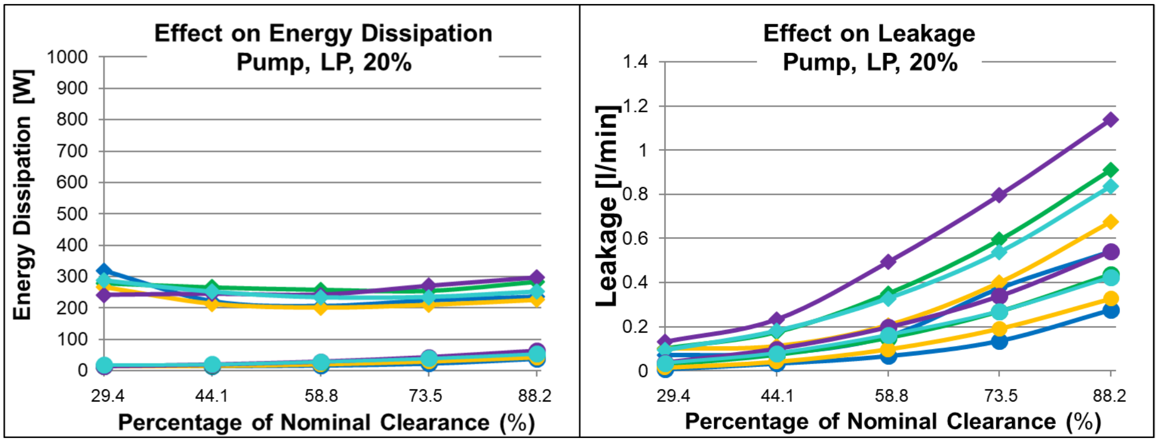

Figure 6.25. Energy dissipation (left) and corresponding leakage (right) due to micro-surface shaping of the piston at reduced clearances for pumping mode, low pressure, partial displacement, T_{in}=52°C.

At lower pressures (● and ♦ markers), Figure 6.25, the reduced clearance among the various surface shape has little effect on the energy dissipation due to the correlation between the reduced leakages and increased torque losses. The trends among the surface profiles still holds for the partial displacement conditions as was detailed for full displacement conditions.

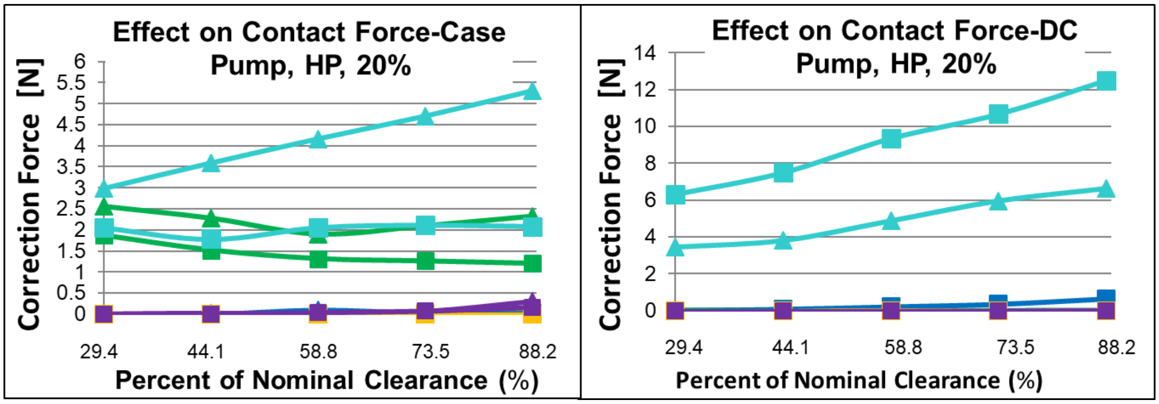

Figure 6.26. Correction forces for case end (left) and DC end (right); pumping mode, high pressure, partial displacement, T_{in}=52°C.

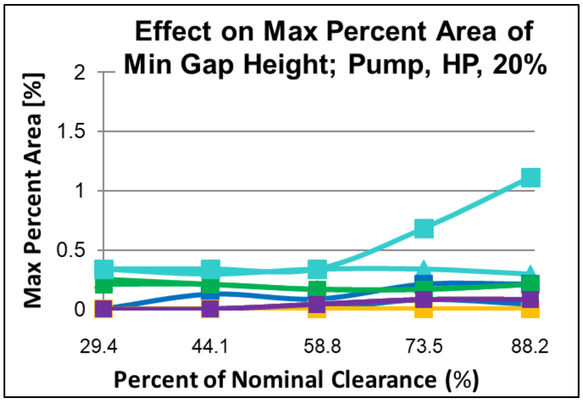

Figure 6.27. Maximum percent area of the gap below the minimum fluid film thickness over an entire revolution; pumping mode, high pressure, partial displacement, T_{in}=52°C.

Analyzing the fluid support criteria, Figure 6.26 and Figure 6.27, for high pressure operating conditions (■ and ▲ markers), the piston is more centered within the bore as the side load is reduced in which only the sinusoidal wave and circumferential sinusoidal wave require correction forces resulting in very minimal areas of minimum critical gap height.

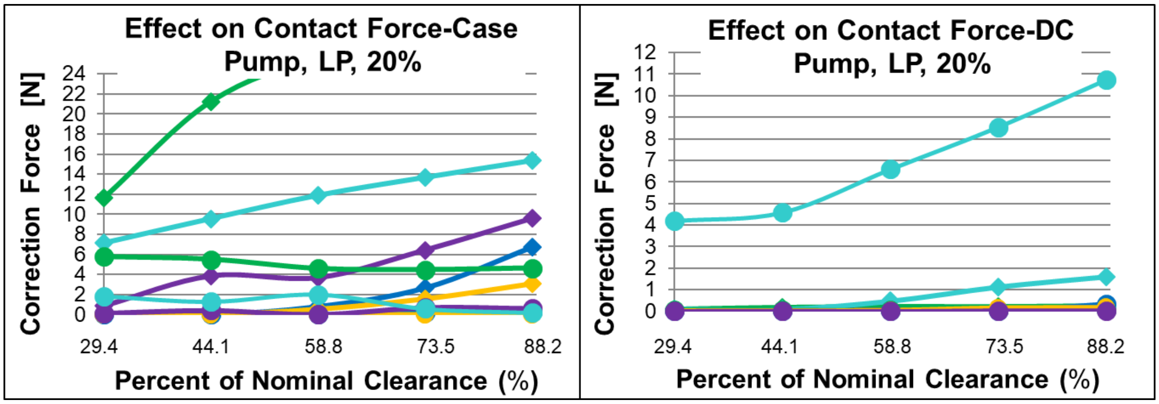

Figure 6.28. Correction forces for case end (left) and DC end (right); pumping mode, low pressure, partial displacement, T_{in}=52°C.

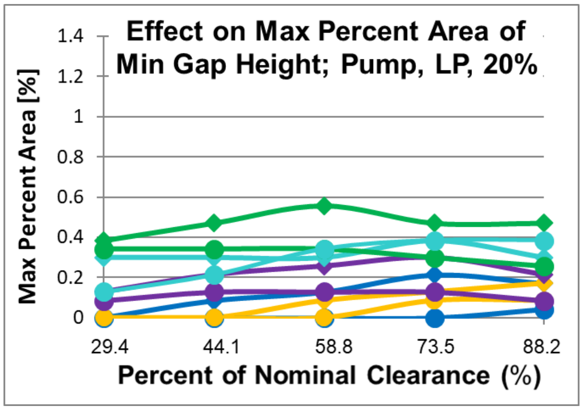

Figure 6.29. Maximum percent area of the gap below the minimum fluid film thickness over an entire revolution; pumping mode, low pressure, partial displacement, T_{in}=52°C.

As the displacement is decreased for the low pressure operating conditions (● and ♦ markers), Figure 6.28 and Figure 6.29, the sinusoidal wave designs become even more problematic in terms of fluid support. As the side forces are reduced, the sine surface profiles tend to slide along a small area of the case end of the bushing increasing the required correction forces. Under such conditions, the piston is no longer forced to tilt building up the fluid support required in which correction forces are in turn not required on the DC end. Again, the barrel and the flat pistons are again the best designs as the clearance is further reduced forcing the slight tilt of the piston to create a wedge effect building up the required fluid support. Yet again, the sinusoidal wave peaks cut off the fluid required to support the external loads leading to the highest correction forces. Additionally, correction forces are even required on the DC end for the circumferential sinusoidal wave as it lacks deviation at the ends to create such a wedge effect.

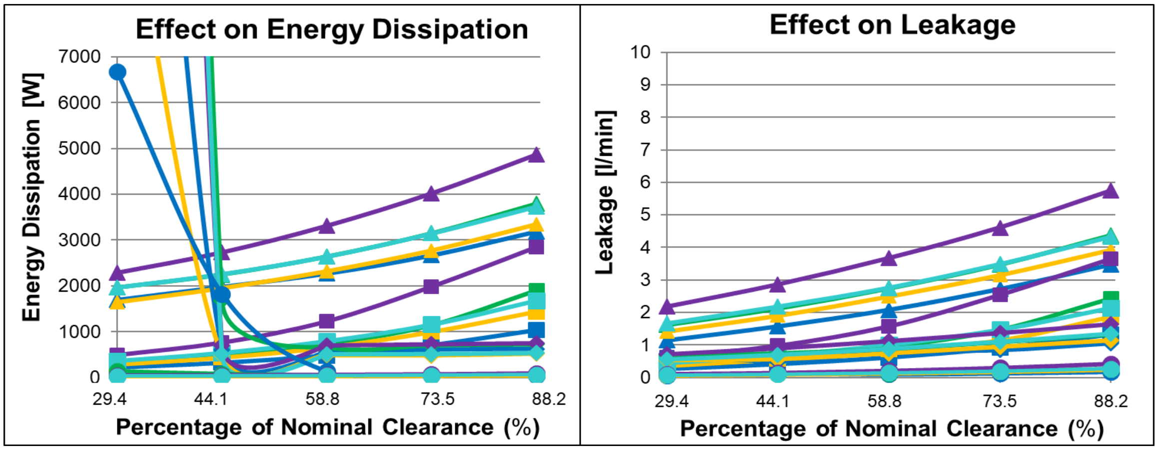

Figure 6.30. Energy dissipation (left) and corresponding leakage (right) due to micro-surface shaping of the piston at reduced clearances; motoring mode, full displacement, T_{in}=52°C.

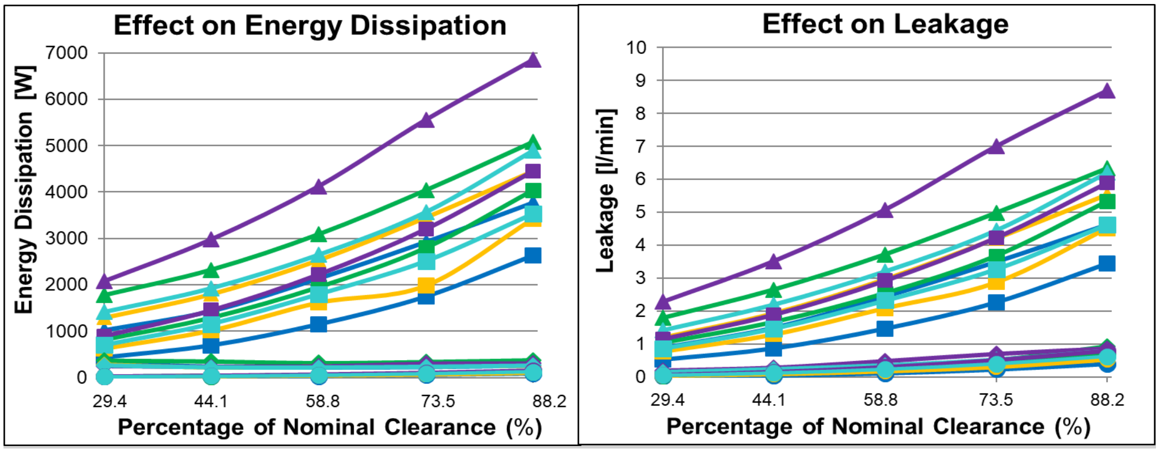

Figure 6.31. Energy dissipation (left) and corresponding leakage (right) due to micro-surface shaping of the piston at reduced clearances; motoring mode, partial displacement, T_{in}=52°C.

Figure 6.30 and Figure 6.31 display the energy dissipation on the left and the corresponding leakages on the right for full and partial displacements respectively in motoring mode. The trends among the surface profiles at the varying clearances for the high pressure and low pressure operating conditions are very similar to the evaluation given for pumping mode. At higher pressures the surface profiles are better with lower clearances as the leakage is largely reduced while for low pressures higher clearances are better due to the decrease in torque losses especially at full displacements. However, at the low pressure operating conditions at full displacements, spikes in the energy dissipation occur as the piston fails to generate fluid support at a reduced clearance as the delivery stroke transitions into the suction stroke around φ=180° resulting in a large spike in the torque losses. It still holds true that the significant decrease in leakages dominates the decrease in overall energy dissipation due to the lower side forces under such conditions at partial displacements. Therefore, not only is a compromise between the high pressure and low pressure operating conditions in pumping mode made when selecting the best design and clearance, but due to spike at low pressure and reduced clearance at full displacement in motoring mode, the barrel is again shown to be best at 44.1% while the flat is best at 58.8%. It still holds in motoring mode that the barrel generates superior fluid support with the flat piston following closely behind whereas the sinusoidal profiles are inferior.

As an overall comparison, the percent improvement in energy dissipation from the baseline, cylindrical design to that of the two best designs of this study, the barrel at a reduced clearance of 44.1% and the flat at 55.8% are shown in Figure 6.32 for pumping mode and Figure 6.34 for motoring mode with supporting evidence of load support for pumping mode in Figure 6.33.

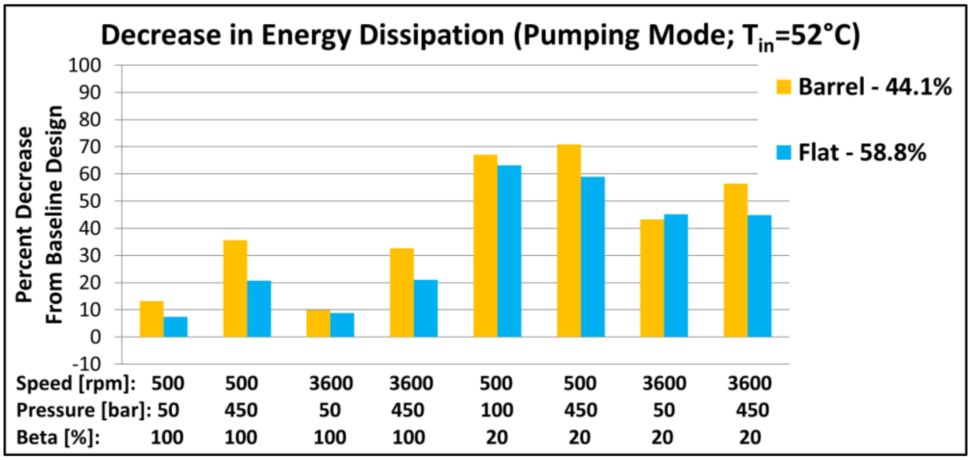

Figure 6.32. Decrease in energy dissipation due to barrel surface profile at 44.1% (orange) in comparison to flat at 55.8% (blue) for pumping mode, T_{in}=52°C.

Comparing the two designs in pumping mode at an inlet temperature of 52°C, Figure 6.32, the barrel piston design at 44.1% (orange) tends to reduce the energy dissipation more so especially at higher pressure operating conditions. This design results in up to a 35% decrease at full displacements and up to 70% at partial displacements, due to the large reduction in leakages at the further reduced clearance.

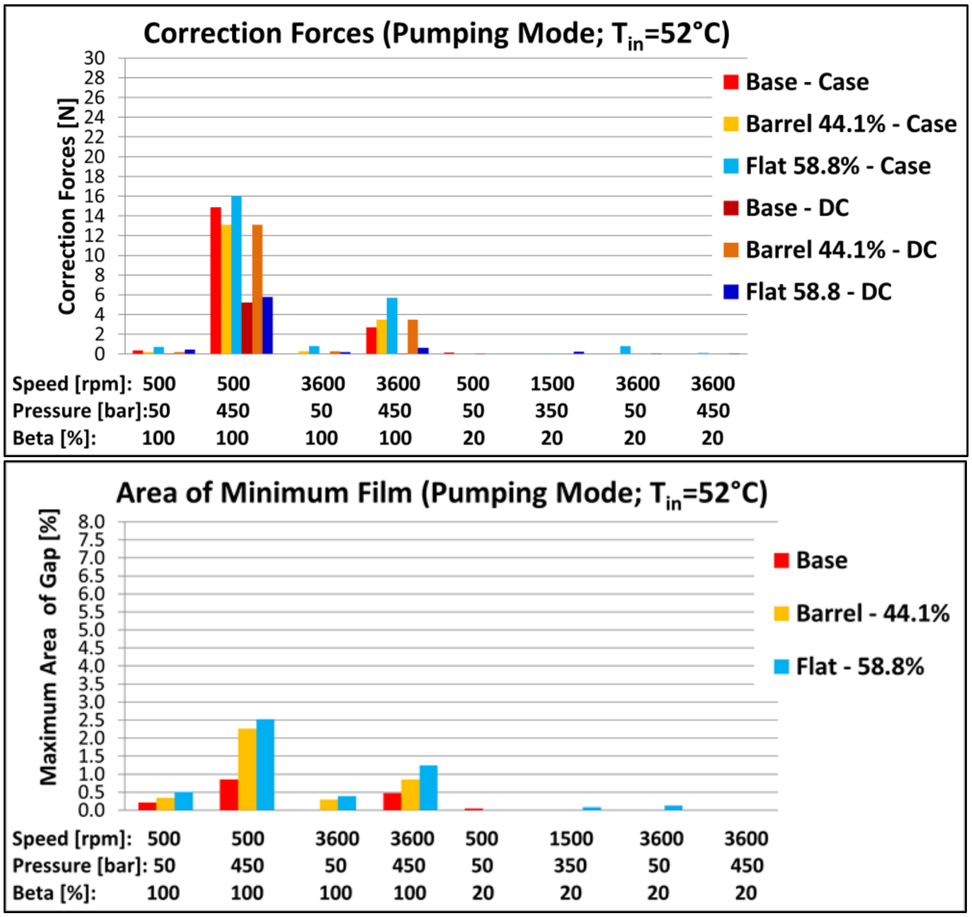

Figure 6.33. Correction forces for case end and DC end (top) and maximum percent area of the gap below the minimum fluid film thickness (bottom) for the barrel surface profile at 44.1% (orange) in comparison to flat at 55.8% (blue) for pumping mode, T$_{in}$=52°C.

According to the fluid support criteria in Figure 6.33, the barrel at the further reduced clearance slightly reduces the correction forces on the case end in comparison to the flat design while averaging out with a slight larger correction force required on the DC end over a marginally smaller area. Overall the fluid support at the corresponding clearances for the barrel and flat designs is comparable to the baseline design implying a similarly reliable design while reducing the energy dissipation across the corner operating conditions of the unit.

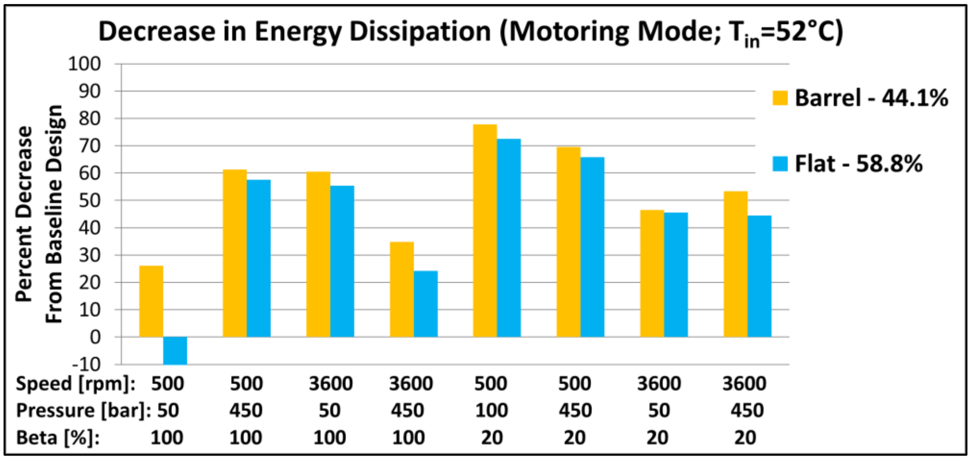

Figure 6.34. Decrease in energy dissipation due to barrel surface profile at 44.1% (orange) in comparison to flat at 55.8% (blue) for motoring mode, T_{in}=52°C.

As for motoring mode, Figure 6.34, both the barrel at a further reduced clearance of 44.1% and the flat at 55.8% perform well and are comparable at the corresponding clearances. The trends are very similar to that shown for pumping mode as both designs can reduced the energy dissipation from the baseline, balancing the decrease in leakage without greatly increasing the torque losses, resulting in a more efficient design. The one exception to this is at 500rpm, 50bar, and full displacement. Under such conditions, the flat surface profile does not build up the required fluid support, sliding across the bushing and in turn generating torque losses leading to a decrease in the energy dissipation. Otherwise, both profiles allow for the corresponding reduction in clearances while maintaining load support resulting in a reliable machine as well.

6.4 Combinations of Piston and Cylinder Surface Shaping

A study was performed to investigate the possible benefits of additional surface shaping on the bushing in combination with the piston. This study combines the surface shapes on the piston, as defined in CHAPTER 4, with similar reflected shapes on the bushing as described below. Note that in the following figures, the clearance and surface deviations are exaggerated. Given that in previous studies, the sinusoidal wave showed points of detrimental minimum fluid film thickness in which the supporting fluid in the gap was blocked off, this study neglects combinations of sinusoidal surface shapes on both the piston and the cylinder as well as a waved barrel bore design.

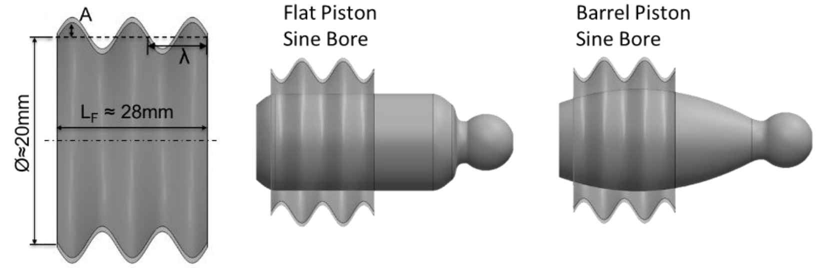

Figure 6.35. Combinations of piston surface shaping with sinusoidal cylinder bore surface shape.

The sinusoidal wave along the axial length of the bore, Figure 6.35, was studied in combination with the flat and barrel pistons. The design parameters of the sinusoidal bore included the amplitude, A:

$$\frac{A\ [\mu m]}{R_Z\ [mm]} = 0.29‰ \tag{6.1}$$

As well as the wavelength, λ:

$$\frac{\lambda\ [mm]}{L_f\ [mm]} = 0.4 \tag{6.2}$$

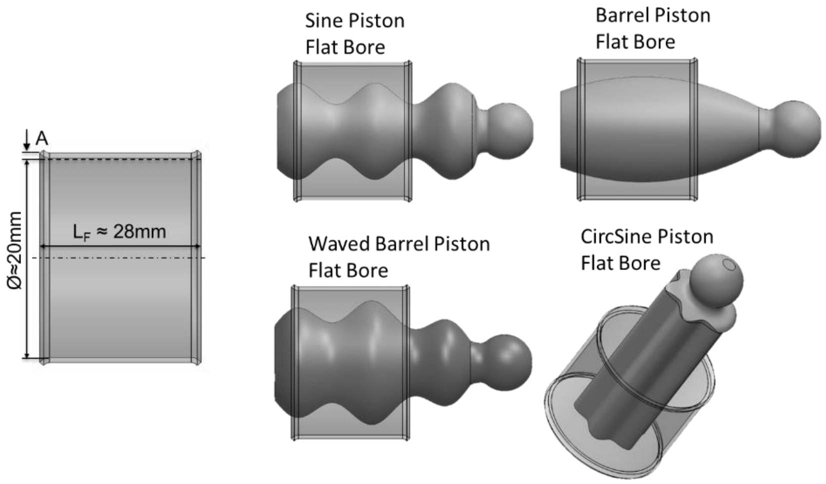

Figure 6.36. Combinations of piston surface shaping with flat cylinder bore surface shape.

The flat design along the axial length of the bore, Figure 6.36, was studied in combination with the sine, barrel, waved barrel, and circumferential sine pistons. The design parameters of the flat bore was defined by the amplitude, A:

$$\frac{A\ [\mu m]}{R_Z\ [mm]} = 0.29‰ \tag{6.3}$$

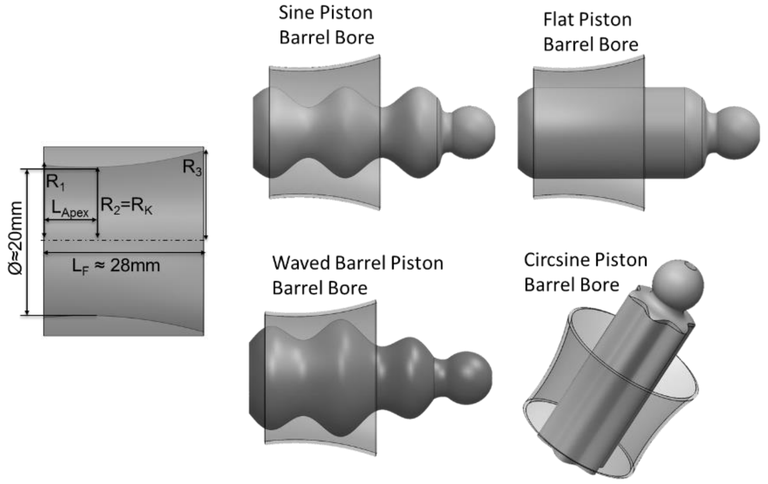

Figure 6.37. Combinations of piston surface shaping with barrel cylinder bore surface shape.

The barrel along the axial length of the bore, Figure 6.37, was studied in combination with the sine, flat, waved barrel, and circumferential sine pistons. The design parameters of the barrel bore included the radius on the DC end, R_1:

$$\frac{R_{1}[mm]}{R_z\,[mm]} = 1.0000 \tag{6.4}$$

The radius on the case end, R_3:

$$\frac{R_{3}[mm]}{R_z\,[mm]} = 1.0004 \tag{6.5}$$

And the location of the apex:

$$\frac{L_{Apex}\,[mm]}{L_f\,[mm]} = 0.4167 \tag{6.6}$$

Note that the radius is still measured from the center of the bore to the surface of the profile.

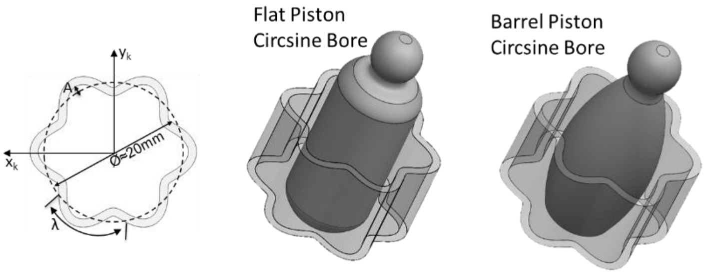

Figure 6.38. Combinations of piston surface shaping with circumferential sinusoidal wave cylinder bore surface shape.

Finally, the sinusoidal wave around the circumference of the bore, Figure 6.38, was studied in combination with the flat and barrel pistons. . The design parameters of the circumferential sinusoidal bore again included the amplitude, A:

$$\frac{A\ [\mu m]}{R_Z\ [mm]} = 0.29‰ \tag{6.7}$$

And the wavelength, λ:

$$\lambda_N = \frac{\lambda\ [mm]}{C_z\ [mm]} = 0.167 \tag{6.8}$$

Throughout this study, the minimum relative clearance between the peak point of the profile on the piston and the peak point of the profile on the bushing remained as:

$$MRC = \frac{h\ [\mu m]}{R_K\ [mm]} = 0.96‰ \tag{6.9}$$

The decrease in energy dissipation and corresponding leakage due to micro-surface shaping of the piston and bushing at reduced clearance in comparison to the baseline design for the corner operating conditions in pumping mode are shown for high pressure in Figure 6.39 and Figure 6.41 and the low pressure in Figure 6.40 and Figure 6.42 respectively. As supporting evidence of machine reliability, the fluid support criteria is subsequently shown in Figure 6.43 and Figure 6.44 for full displacement only since fluid support is not as much of an issue among the better designs at partial displacements.

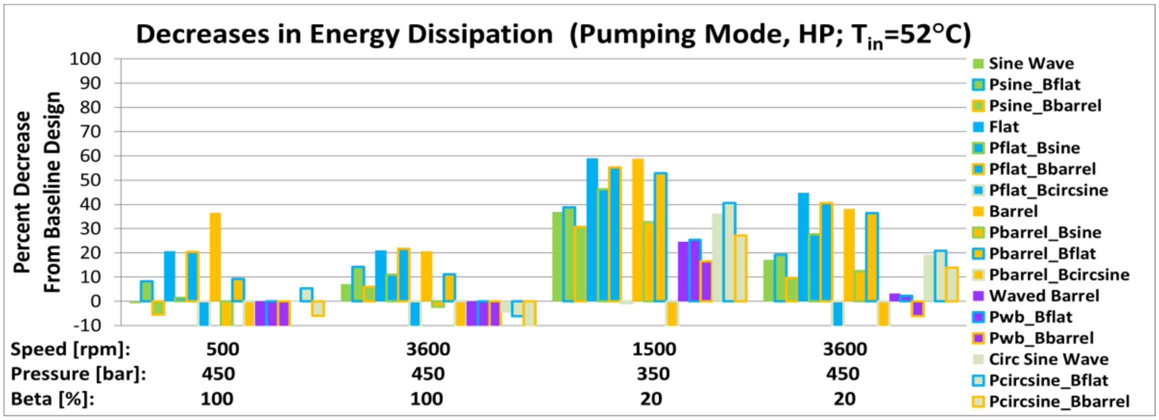

Figure 6.39. Decrease in energy dissipation due to micro-surface shaping of the piston and cylinder; pumping mode, high pressure, T_{in}=52°C.

For high pressure operating conditions, the combination of micro-surface shaping on both the piston and the bushing is worse in reducing the overall energy dissipation in most cases, Figure 6.39, than that of solely on the piston. The exception to this statement is the combination of any of the waved pistons with the flat bore. At high pressures, a bore with deviation at ends due to the additional surface shaping allows for more leakage, Figure 6.41, out of the gap under high pressure.

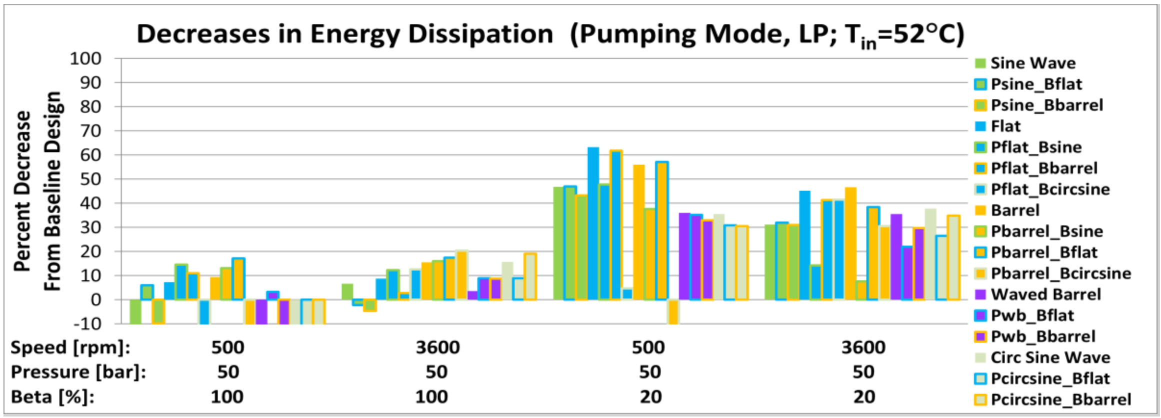

Figure 6.40. Decrease in energy dissipation due to micro-surface shaping of the piston and cylinder; pumping mode, low pressure, T_{in}=52°C.

On the contrary, for low pressure operating conditions, especially so at high speeds, the combination of surface shaping tends to do better although are still mostly outperformed by the surface shaping on the piston alone. At lower pressures, the combinations tend to do slightly better as opposed to the high pressure operating conditions due to the additional fluid support while not largely pushing fluid from the gap, Figure 6.42.

For the sinusoidal wave piston, it performs best in combination with a flat bushing. By adding the deviation at the ends of the gap, the concentrated areas of critical fluid film thickness at the peaks of the profile is reduced, shown in Figure 6.43 and Figure 6.44, allowing fluid into the gap to aid in the support of the external forces acting on the piston. With the barrel profile, the larger deviation at the ends of the gap allows the piston to tilt too much still resulting in insufficient fluid support as well as larger leakages.

Implementing a surface profile on the bushing in combination with the flat piston profile has no additional benefits overall. Although the combination with a sine bushing does show improvements at low pressure operating conditions, a barrel bushing is better at high pressures and partial displacements; none of the combinations showing improvements over the entire range of operating conditions. Additionally, the flat piston does well as the clearance is most reduced across the gap. By removing more material from the gap, the leakages are increased.

Likewise, for the barrel piston, in combination with a flat or sinusoidal bushing can aid at low pressure operating conditions due to the additional deviation at the ends, but at high pressures, this deviation increases the leakages in which overall the decrease in energy dissipation is not superior. Combining this design with a circumferential sinusoidal bushing is far inferior in leakage and fluid support and consequently the overall energy dissipation.

As for the waved barrel piston along with the circumferential sinusoidal wave piston, the additional deviation at the ends of the gap due to a barrel or flat bushing can slightly aid in fluid support, but not such that these designs can become beneficial in comparison.

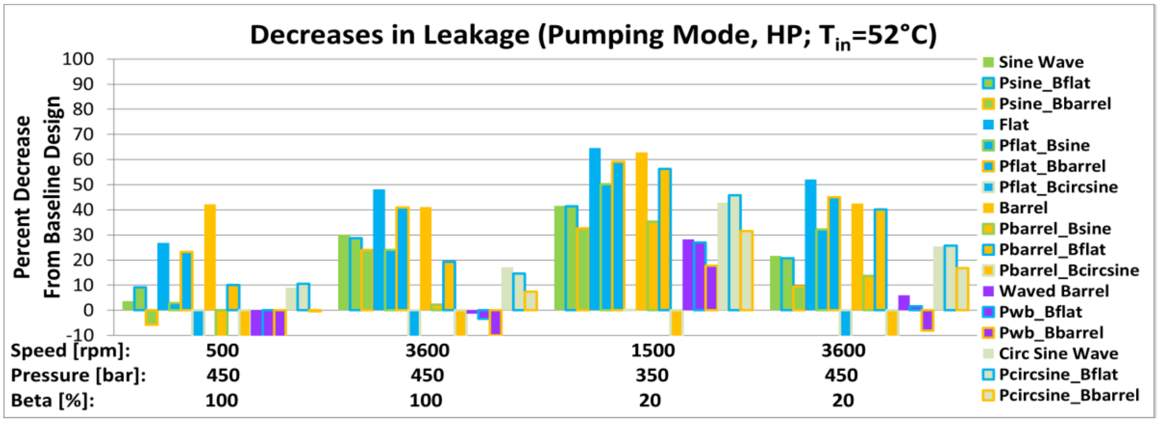

Figure 6.41. Decrease in leakage due to micro-surface shaping of the piston and cylinder; pumping mode, high pressure, T_{in}=52°C.

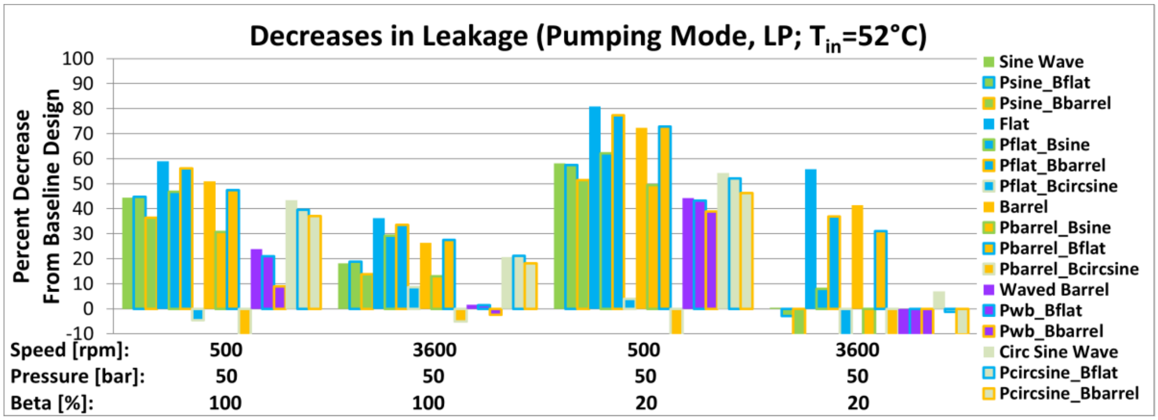

Figure 6.42. Decrease in leakage due to micro-surface shaping of the piston and cylinder; pumping mode, low pressure, T_{in}=52°C.

It still holds in this study that the majority of the reduction in leakage, Figure 6.41 and Figure 6.42, is due to the reduced clearance of 58.8% of the nominal clearance. By adding a surface profile to the bushing in combination to the piston, there is additional deviation of the gap allowing for more fluid to flow from the gap resulting in a lower decrease in leakage in comparison to surface shaping solely on the piston.

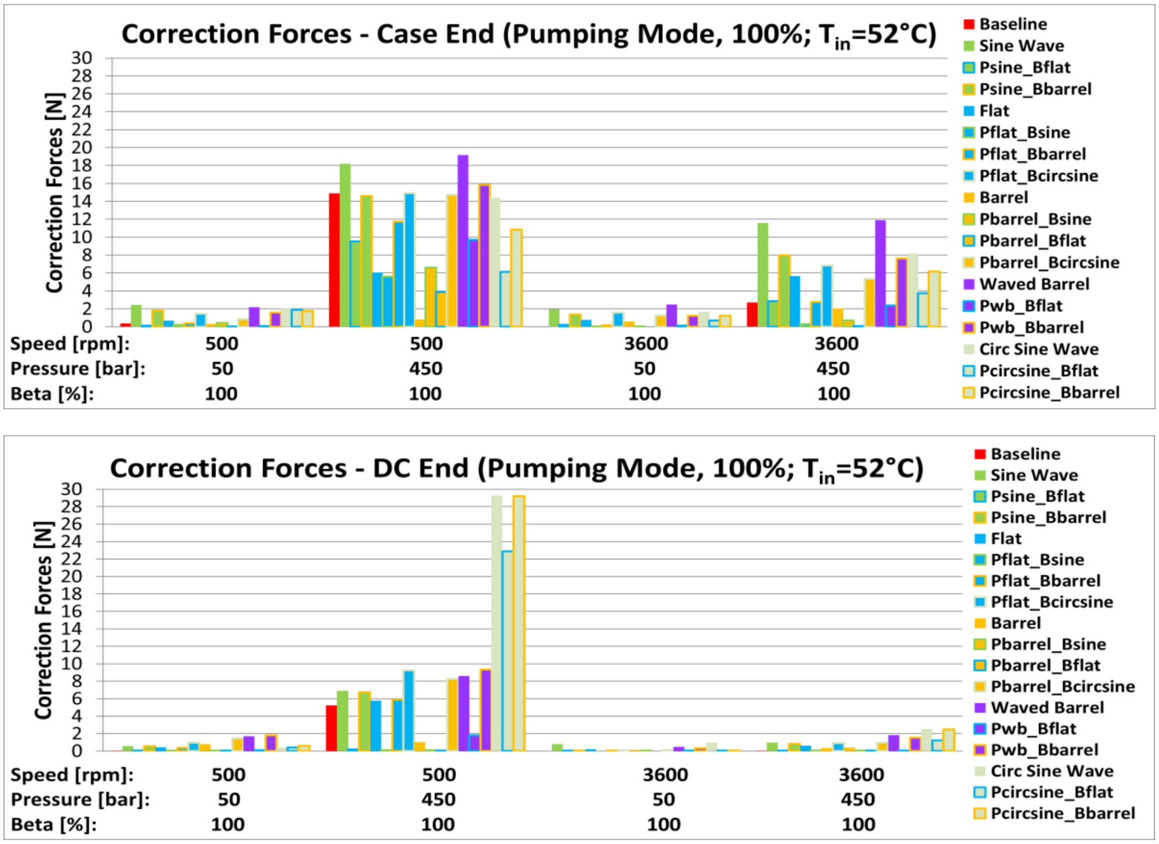

Figure 6.43. Correction forces for case end (top) and DC end (bottom); pumping mode, full displacement, T_{in}=52°C.

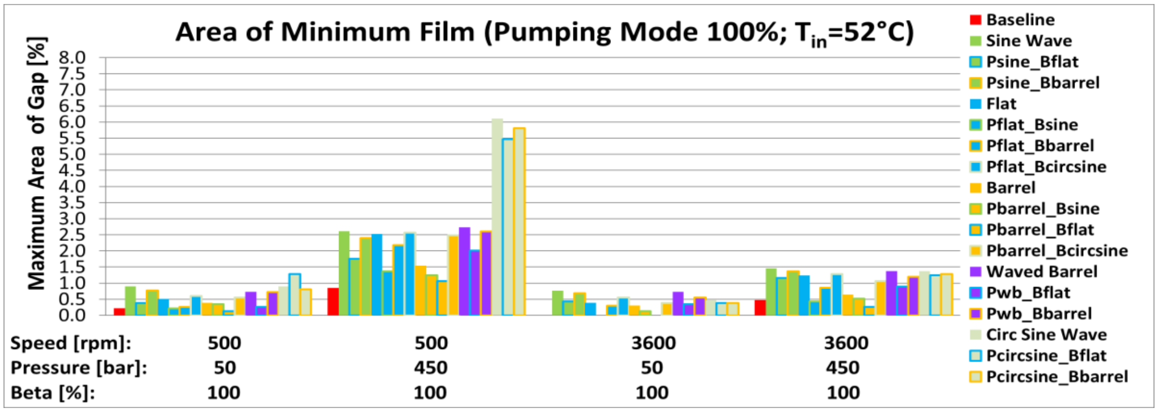

Figure 6.44. Maximum percent area of the gap below the minimum fluid film thickness over an entire revolution; pumping mode, full displacement, T_{in}=52°C.

In terms of fluid support, additional surface shaping on the bushing reduces the contact forces on the case end for the sinusoidal pistons in combination with a flat or barrel bore shaping, Figure 6.43 (top). On the DC end, Figure 6.43 (bottom), the flat and sine bushing reduce the contact forces.

The small deviation at ends mitigates the need for additional external force to support the load at these locations, especially so at 500rpm, 450bar, 100% where fluid support issues arise. With additional shaping on the bushing, the removal of the material at the ends of the bushing reduces the area where critical film thickness, Figure 6.44 , tends to occur.

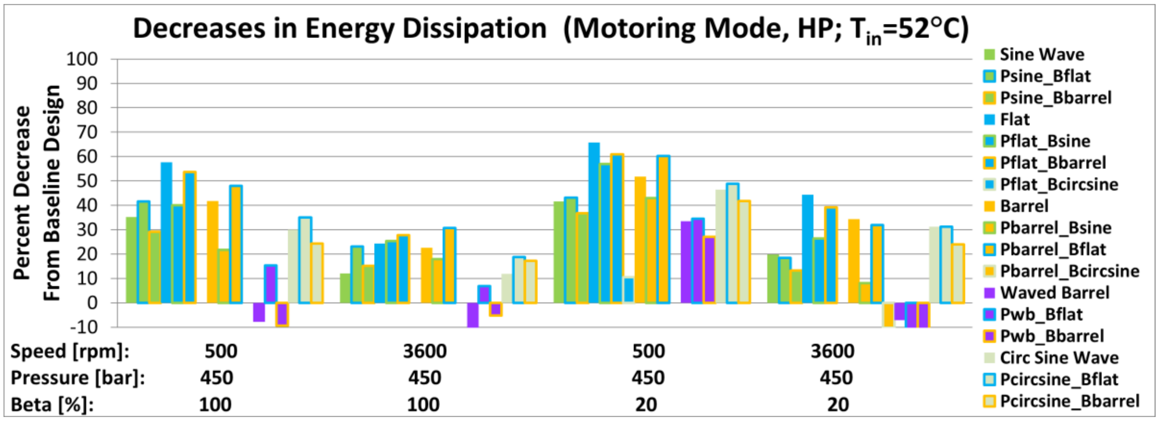

Figure 6.45. Decrease in energy dissipation due to micro-surface shaping of the piston and cylinder; motoring mode, high pressure T_{in}=52°C.

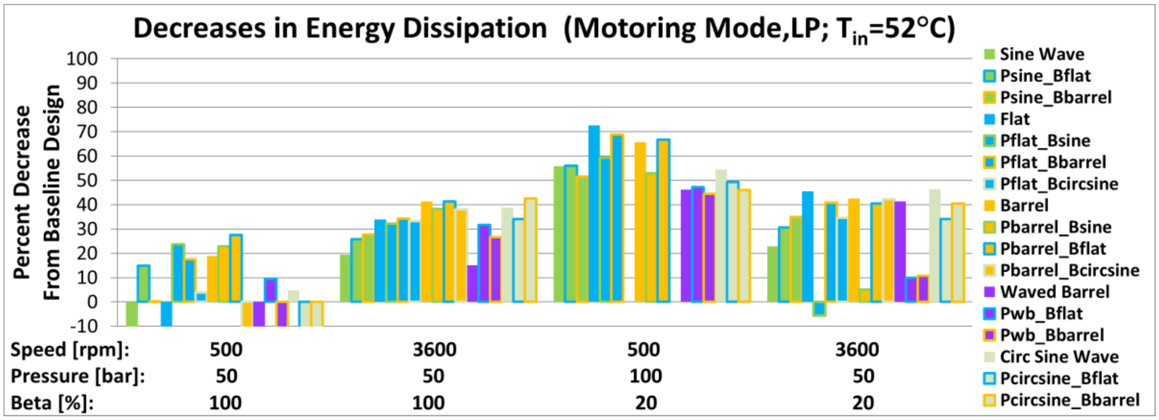

Figure 6.46. Decrease in leakage due to micro-surface shaping of the piston and cylinder; motoring mode, low pressure T_{in}=52°C.

For motoring mode, Figure 6.45 and Figure 6.46, the reduction in losses are again very similar to the results of pumping mode. The difference between the baseline design and the combination of surface shapes is maintained among the corner operating conditions investigated.

In conclusion to this study, the combinations of surface shaping between the bushing and the piston does not present a comprehensive benefit. Although there is a slight benefit in fluid support with the combination designs, the efficiency of the machine is not improved overall. Therefore, the increase in manufacturing costs would outweigh the benefits of additional surface shaping of the bushing; micro-surface shaping of the piston alone is sufficient.

6.5 Effects of Fluid Properties

All of the previous studies were conducted with a constant inlet temperature of 52°C corresponding to a fluid viscosity of 20cSt. To further test the capabilities of piston micro-surface shaping, the piston/cylinder interface was simulated at an increased constant inlet temperature of 75°C correlating to a decrease in fluid viscosity of 10cSt. For correct boundary conditions, the thermal model was utilized to predict the corresponding case and outlet temperatures.

The resulting behavior of piston micro-surface shaping in comparison to the baseline, wear-in design with reduced viscosity fluid at the corner operating conditions is shown below. The decrease in energy dissipation and leakages from the baseline for pumping mode are presented in Figure 6.47 and Figure 6.48 as well as for motoring mode in Figure 6.52 and Figure 6.53 respectively. In order to quantify fluid film support, the percentage of the gap below a fluid film thickness, Figure 6.49, as well as the correction forces, Figure 6.50, are shown for the corner power operating condition.

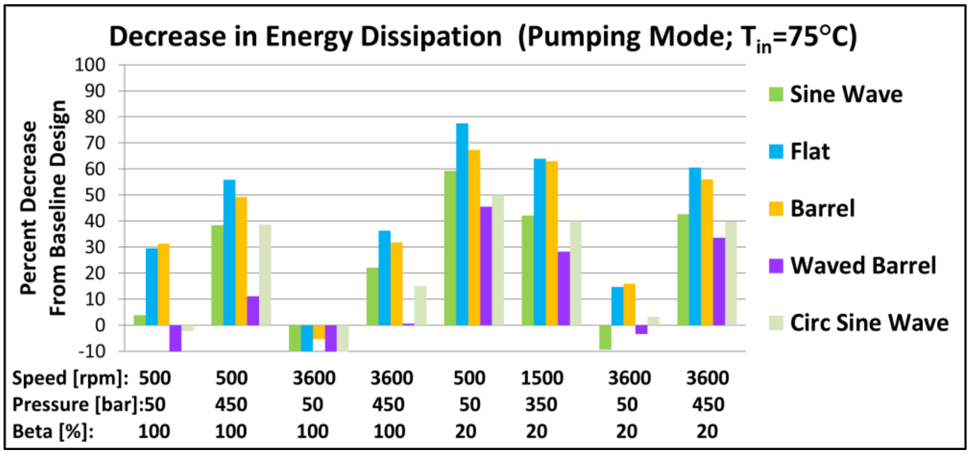

Figure 6.47. Decrease in energy dissipation due to micro-surface shaping of the piston; pumping mode, T_{in}=75°C.

The decrease in energy dissipation, Figure 6.47, is very similar for the various surface shapes operating with a less viscous fluid as was shown in the previous sections. Not only do similar trends across the operating conditions follow, but trends between the surface profiles are also very comparable. Note that designs are compared to the baseline design at the increased temperature as well. The resulting reduction in energy dissipation is slightly more, almost 80%, due to large reduction in leakages. Since the fluid is less viscous, it flows more easily from the gap hence a reduction in clearance has a larger effect on the reduction in leakages, shown in Figure 6.48. The exception to this is at high speed, 3600rpm, and low pressure, 50 bar, where fluid support is not generated and shearing of the fluid occurs.

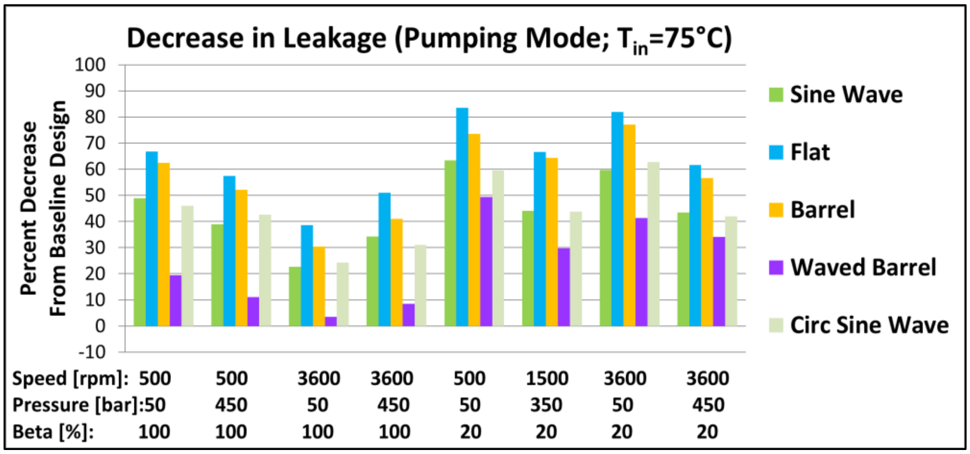

Figure 6.48. Decrease in leakage due to micro-surface shaping of the piston; pumping mode, T_{in}=75°C.

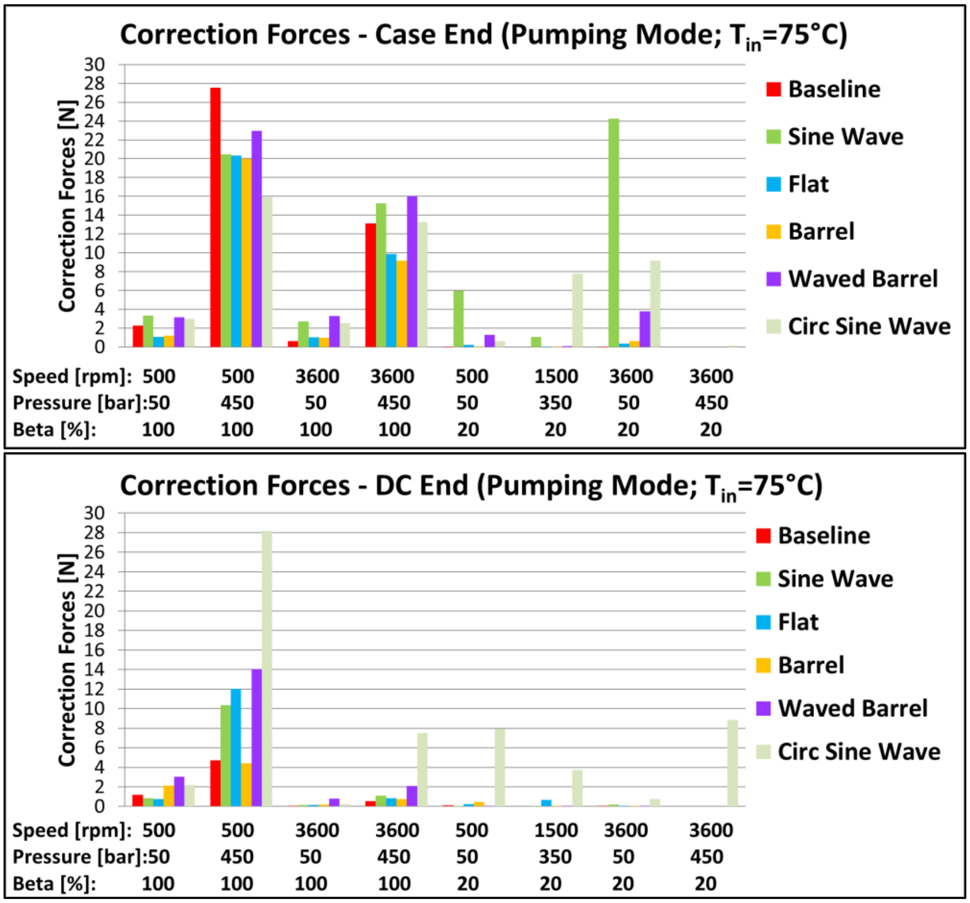

Figure 6.49. Correction forces for case end (top) and DC end (bottom); pumping mode, T_{in}=75°C.

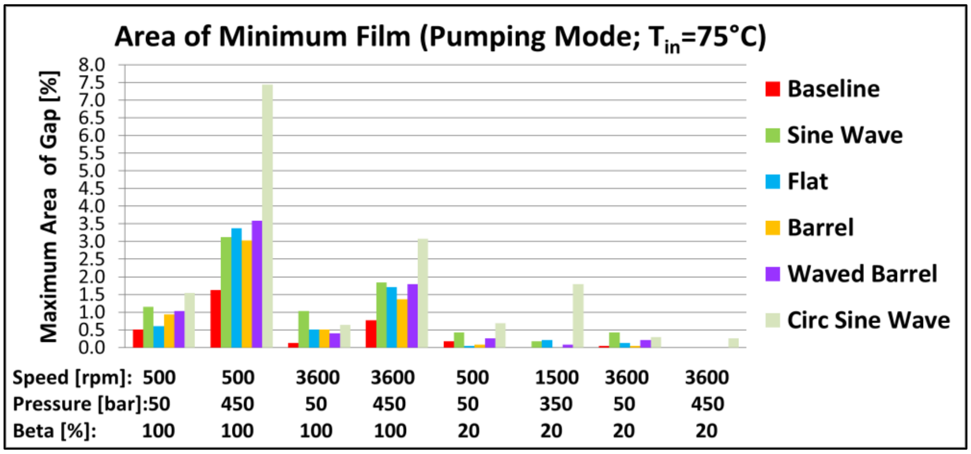

Figure 6.50. Maximum percent area of the gap below the minimum fluid film thickness over an entire revolution; pumping mode, T_{in}=75°C.

As the viscosity of the fluid is reduced, the correction forces required to fully support the external forces along with the critical areas are increased. This signifies that the support of the fluid film is degraded with the viscosity in which additional external force is required to balance the load. Nevertheless, the trend between the various surface profiles still remains. The barrel continues to be the best in which the percentage of critical areas and the correction forces are minimal signifying superior fluid support among the designs studied in comparison the baseline design.

In further support of this claim as the temperature increases, the difference between the fluid film thickness and pressure field at T_{in}=52°C and T_{in}=75°C is shown in a multi-plot in Figure 6.51. Note that a positive value correlates to larger value at T_{in}=52°C.

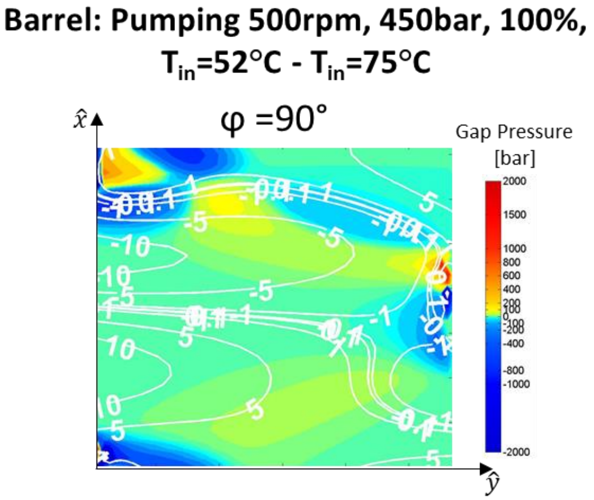

Figure 6.51. Barrel simulated difference multi-plot for pumping mode 500rpm, 450bar, 100%, T_{in}=52°C - T_{in}=75°C; φ=90°.

At the increased temperature, larger areas of critical fluid film thickness occur on the DC and case end, signified by the -0.1micron difference on each end. In these areas, the fluid film pressure is larger directly in front of the piston, in the positive $\hat{x}$-axis. This aids in the fluid support at the lower inlet temperature

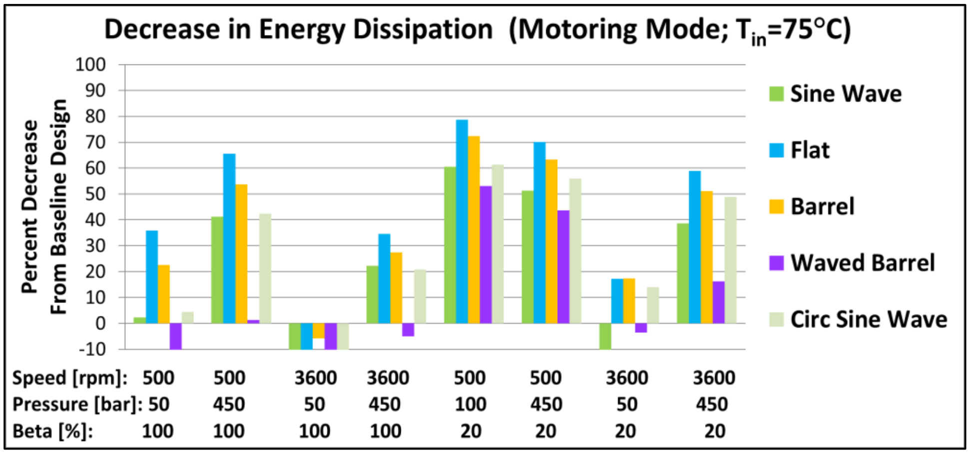

Figure 6.52. Decrease in energy dissipation due to micro-surface shaping of the piston; motoring mode, T_{in}=75°C.

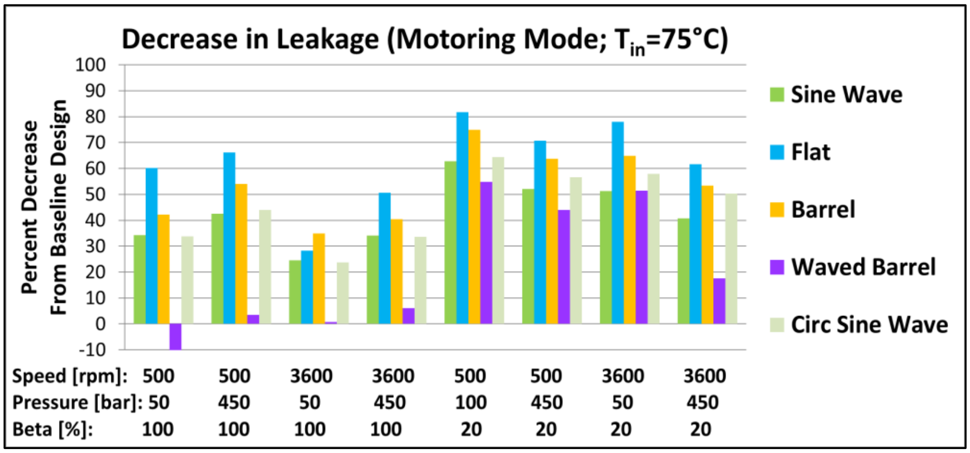

Figure 6.53. Decrease in leakage due to micro-surface shaping of the piston; motoring mode, T_{in}=75°C.

The results of motoring mode at the corner operating conditions are again very similar to that as was demonstrated for pumping mode. Likewise, with the decrease in viscosity, the improvements from the baseline to the surface shaped pistons at a reduced clearance remains comparable.

6.6 Effects of Surface Shaping on Unit Thermal Behavior

As has been shown throughout the investigation of surface shaping of the piston at reduced clearances, the leakages are largely reduced. The concern that arises is that by drastically reducing the leakages, less cooling action of the lubricating film is present even as the energy dissipation is reduced as well. An increase in the temperatures within the gap could affect the operating temperatures and in turn the viscosity of the working fluid resulting in a change in the performance of the machine. This increase in temperature could also possibly lead to piston stick due to the effects on the solid body deformations leading to catastrophic failure. Specifically, since the barrel supports the load at all corner operating conditions while largely decreasing the leakages as well as the overall energy dissipation at reduced clearances from the baseline, this case will be further analyzed.

The reduction in the losses from the baseline unit (considering all three interfaces) as well the difference in the resulting temperatures are shown in Figure 6.54 and Figure 6.55 for pumping and motoring mode respectively at an inlet temperature of 52°C. The updated operating temperatures are calculated utilizing a thermal model (Shang, 2015) considering the losses resulting from the simulation of the barrel micro-surface piston with the baseline slipper/swashplate and cylinder block/valve plate interfaces. The difference in the resulting maximum temperature occurring in the gap between the piston and cylinder is also shown. Note that a positive difference in temperatures signifies an increase due to barrel surface shaping of the piston.

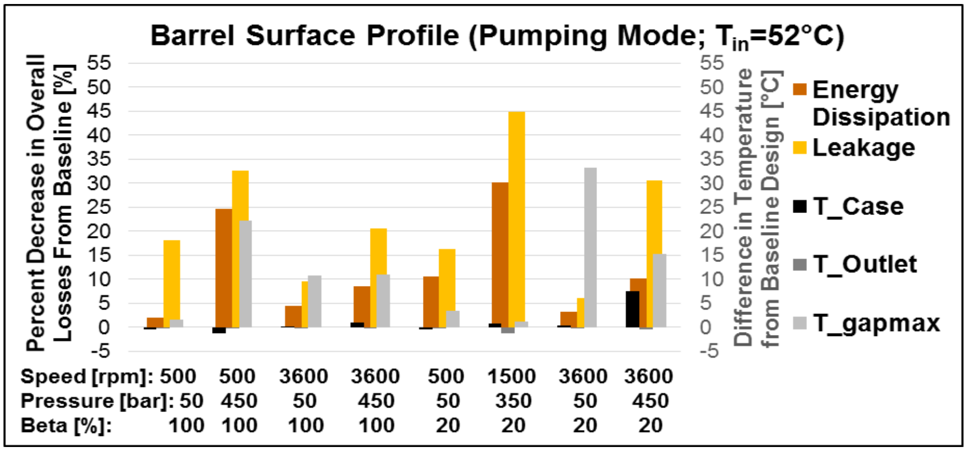

Figure 6.54. Decrease in losses and temperature due to barrel surface shaping of the piston; pumping mode, T_{in}=52°C.

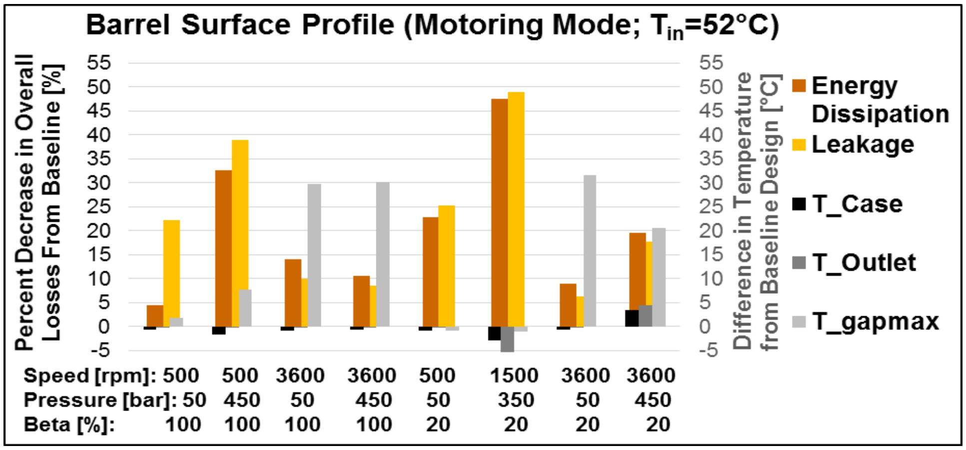

Figure 6.55. Decrease in losses and temperature due to barrel surface shaping of the piston; motoring mode, T_{in}=52°C.

Although there is a large reduction in energy dissipation and leakages from the baseline through the introduction of a barrel surface profile on the piston at a reduced clearance for both pumping and motoring mode, there is a minimal effect on the overall operating temperatures. The largest increase in the case temperature is 7°C over the range of corner operating conditions in which the case temperature is actually predominantly reduced. The reason for this is that as the leakage is reduced, the fluid from the piston/cylinder interface contributes a lower proportion of fluid in comparison to the other interfaces on the total case fluid and therefore has less effect on overall temperature. The outlet temperature is also relatively unaffected, changing by less than 1°C for all operating conditions. This determines that the performance of the machine should be insignificantly affected by the changes in temperatures.

On the other hand, the temperature in the gap is largely increased from the baseline design; up to a 35°C. This increase in gap temperature occurs due to mitigating the cooling effect of the oil as it flows through the gap. In other words, since the leakage is largely reduced as the clearance is reduced, the fluid has a longer time to heat up within the gap. Furthermore, as the clearance is reduced, the torque losses are compromised, adding to the heating effect. This leads to the concern of the possibility of piston stick. Thus, the lubricating film temperature and resulting thermal deformations of the solid bodies are analyzed. The multi-plots in Figure 6.56 portrays the fluid film temperature in the gap between the piston and cylinder in colored contour with the combined deformations of solid bodies overlaid in white line contour at φ = 90° in the high pressure stroke. The combined deformations signify the change in the fluid film thickness, a positive number reflecting an increase in thickness. The plots are displayed for the corner power operating condition, 3600rpm, 50bar, 20% in pumping mode considering the largest increase in the gap temperature occurred under such conditions.

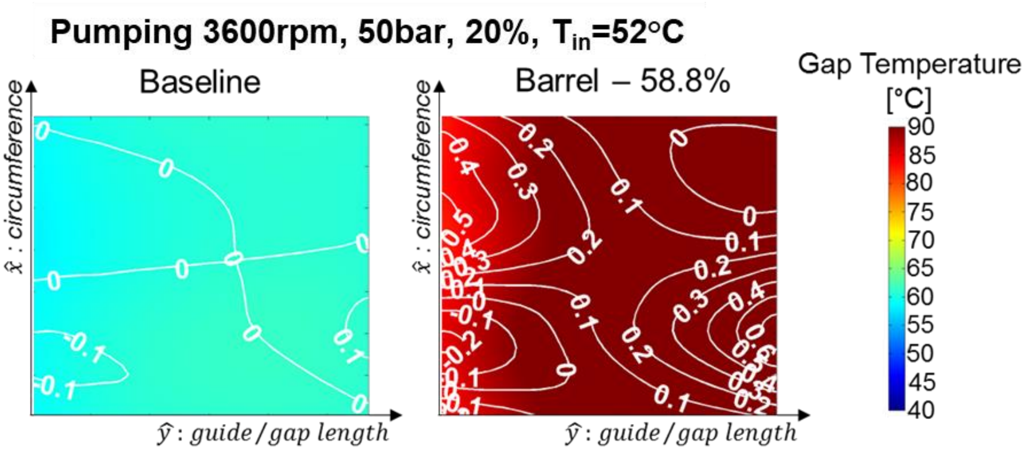

Figure 6.56. Thermal multi-plots at φ=90° for pumping mode 3600rpm, 50bar, 20%; T_{in}=52°C; Baseline (left), Barrel (right).

Comparing the baseline, Figure 6.56 left, to the barrel at 58.8% clearance, right, it can be seen that the fluid temperature in the lubricating gap does increase by about 35°C. This increase in temperature leads to an increase in gap height of about 0.6μm near the case end as the bushing expands at a faster rate than the piston. On the DC end, although there is a 0.2μm decrease in the fluid film, a 0.5μm increase occurs circumferentially opposite simply creating a shift in the fluid film and an overall increase of 0.3μm.Overall, it can be determined that the combination of thermal deformations between the piston and cylinder has little effect on the lubricating fluid film geometry despite the increase in temperature as both solid bodies expand with the additional heat. This means that there is no additional risk for piston stick due to the increase in gap temperature at reduced clearances.

Since this unit also operates at higher inlet temperatures as analyzed in Section 6.5, this case must also be considered. Similarly, the reduction in the losses for the barrel piston from the baseline unit (considering all three interfaces) as well the difference in the resulting operating temperatures are shown in Figure 6.57 and Figure 6.58 for pumping and motoring mode respectively at an inlet temperature of 75°C corresponding to a fluid viscosity of 10cSt.

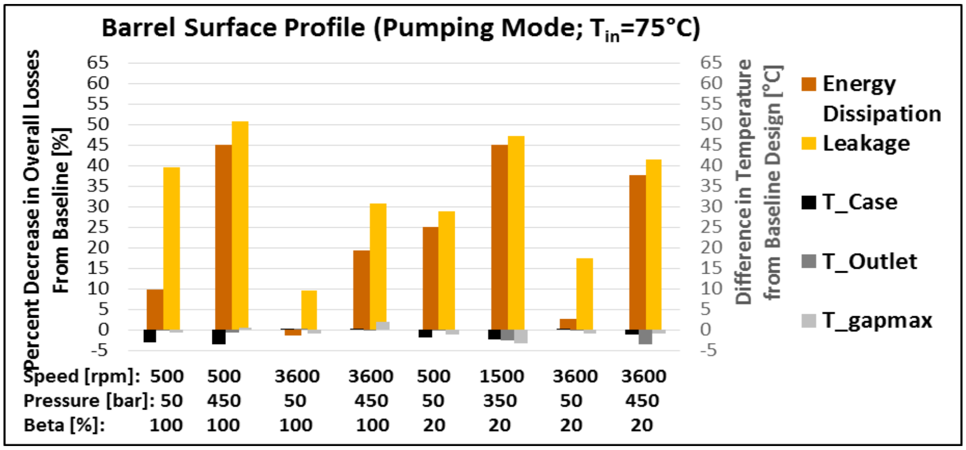

Figure 6.57. Decrease in losses and temperature due to barrel surface shaping of the piston; pumping mode, T_{in}=75°C.

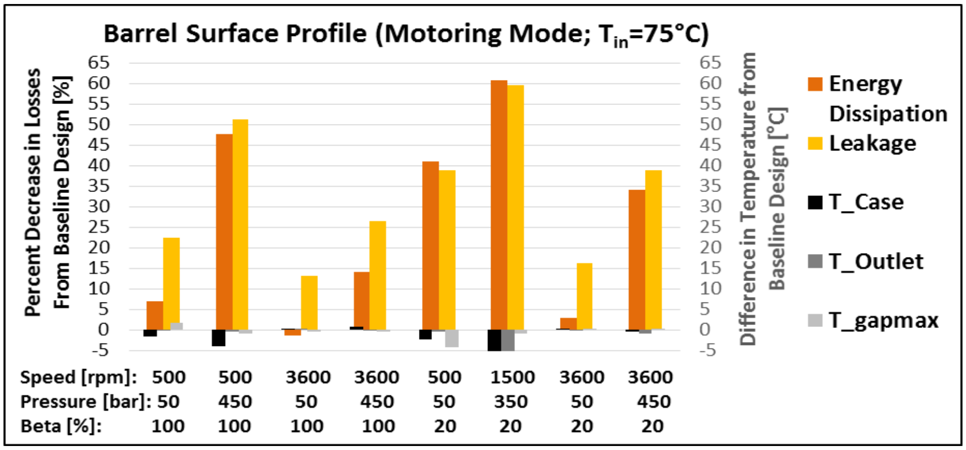

Figure 6.58. Decrease in losses and temperature due to barrel surface shaping of the piston; motoring mode at an increased inlet temperature of 75°C.

Similarly for the increased inlet temperature, i.e. reduced viscosity, for both pumping and motoring mode, Figure 6.57 and Figure 6.58, there is less than a 3°C decrease in the case and outlet temperature. Again, the reason for this is that as the leakage is reduced due to a reduced clearance, the fluid from the piston/cylinder interface contributes a lower proportion of fluid in comparison to the other interfaces and therefore has less of an effect on the overall temperatures. This determines that the performance of the machine should be insignificantly effected by the minimal changes in temperatures.

Likewise, the possibility of piston stick is of concern. However, since the fluid viscosity is decreased at the increased inlet temperature, the leakages are higher and the torque losses are lower leading to a minimal effect on the gap temperature. In further support of this claim, the lubricating film temperature and resulting thermal deformations of the solid bodies are analyzed as shown in Figure 6.59 for 3600rpm, 50bar, 20% in pumping mode at an increased inlet temperature of 75°C.

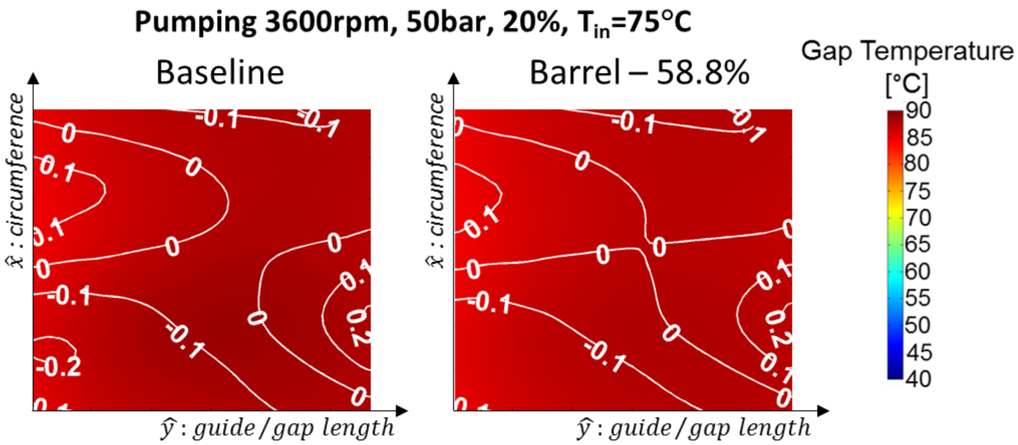

Figure 6.59. Thermal multi-plots at φ=90° for pumping mode 3600rpm, 50bar, 20%; T_{in}=75°C; Baseline (left), Barrel (right).

Comparing the baseline, Figure 6.56 left, to the barrel at 58.8% clearance, right, it can be seen that the fluid temperature in the lubricating gap changes very little. Accordingly, the overall effect of the thermal deformations of the solid bodies on the fluid film thickness is minuscule. Therefore it can be further concluded that piston stick at increased operating temperatures will be of minimal concern with surface shaping of the piston at reduced clearances.

6.7 Summary

In conclusion to the extensive investigation of the piston micro-surface shaping for the 75cc unit, the barrel piston at a reduced clearance of 44.1% clearance tends to perform best in terms of efficiency and reliability. This design not only reduces the energy dissipation, up to a 35% decrease at full displacements and 70% at partial displacements, by largely reducing the leakages without increasing the torque losses at a reduced clearance, but also generates the required fluid film support at even the most demanding operating conditions in both pumping and motoring mode. The barrel shape allows for the piston to tilt manipulating the fluid film in order to develop the build-up of the pressure in the fluid.

The flat surface profile is also similar in reducing the energy dissipation of the interface at a 58.8% reduced clearance; although an even further reduced clearance results in less leakage, the torque losses become compromised as well as the fluid support. The benefit of this design is that the small deviations at the ends allow the piston to tilt while the cylindrical center maintains the pressure build-up required to support the external loads along the gap.

The designs incorporating a sinusoidal wave are infeasible at the reduced clearances studied. Issues tend to arise as the external loads are no longer supported as a result of the peaks of the sine wave develop concentrated areas of critical film in turn blocking off the fluid to the gap leading to the inability to generate the fluid support required to balance the external forces.

Additional surface shaping on the bushing in combination to the surface shaping of the piston was shown to not create an overall advantage. Although the fluid support was slightly more developed, the efficiency was not further improved. Therefore, the additional manufacturing costs outweigh the minimal benefit of a combined design.

Decreasing the fluid viscosity by increasing the inlet temperature had little effect on the outcome among the surface profiles in comparison to the baseline over the range of corner operating conditions. The difference arises as the correction forces are increased signifying a degrade in fluid film support as additional support is required to prevent the occurrence of minimum film thickness with a lower viscosity operating fluid.

As for the thermal behavior of the unit as a result of decreasing the energy dissipation and leakages from the piston/cylinder interface due to piston micro-surface shaping, it was demonstrated that the effect on the other interfaces would be minimal and that piston stick would not become a greater risk as the gap temperature is increased. By reducing the fluid flow from the piston/cylinder gap into the case there is less of an impact on the operating temperatures in comparison to other interfaces, resulting in less than a 7°C change. However, this reduction in fluid flow allows for more time to heat the fluid within the gap although the resulting effect of the thermal deformations is minimal, actually slightly increasing the overall fluid film thickness as the solid bodies expand, mitigating possible piston stick.

CHAPTER 7. PISTON MICRO-SURFACE SHAPING OPTIMIZATION

Once the beneficial influences of surface shaping were thoroughly understood and proven through simulation of an existing unit, the ideology can was then applied through an optimization process on the piston/cylinder interface designed utilizing the simulation tool. By comparing the behavior of the lubricating film between the piston and cylinder of the initial, standard design to an optimal piston micro-surface shape it was reiterated that not only the efficiency of the unit can be improved, but also the fluid film support resulting in more reliable and longer lasting interface. This design process furthermore proved the capabilities of a modern virtual prototyping approach utilizing the current fluid structure interaction model with the port and case temperature prediction tool to predict the behavior of the fluid film; starting from an initial design that was then optimized rather than the traditional trial and error method.

7.1 Optimization Algorithm: Archived Based Micro Genetic Algorithm (AMGA2)

In the interest of optimizing the surface shape of the piston, an open source archived based micro genetic algorithm (AMGA2) for multi-objective optimization scheme (Tiwari, Fadel, & Deb, 2011) was utilized. Such optimization processes have become readily available with the advancement of computational models as the processing speed of computers has been greatly accelerated in the recent years.

7.1.1 Advantages/Disadvantages

The AMGA2 optimization methodology was chosen to be appropriate in particular to this case based on the many advantages that it possesses when applied to such an engineering problem of optimizing the piston/cylinder interface through surface shaping. This method is resilient to premature convergence and therefore capable of handling nonlinear and multi-modal functions that can be very complex. Furthermore, it is capable of handling the difficulties posed by various search spaces that can be discontinuous, discrete, and even non-convex. The AMGA2 is very advantageous in the aspect of handling any size of optimization problems including rather large ones consisting of many variables, objectives, and/or constraints. Another reason this model is superior is due the minimal number of function evaluations required for convergence resulting in speed. This means that this method works with a small population size storing and utilizing the best solutions in a larger and dominating archive, as well as using the most diverse points further reducing the number of function evaluations by not calculating for similar points. By considering such diversity across the design space, this also results in an avoidance of local minima, ultimately concluding the global minima. Finally, this method begins with an initial population that is random and unbiased over the specified design space leading to reliable convergence.

Among all of the advantages pertaining to the AMGA2, a few disadvantages also arise. This method tends to perform poorly with single-objective optimization problems, although not a concern in the following problem that is multi-objective. Improvements could also be made to the algorithm as it does not currently consider knowledge integration from external sources such as manufacturability of the various designs of the piston. The biggest downfall of this method though, is that the size and choice of the parent population can affect the performance, possibly slowing down the convergence speed.

7.1.2 Procedure

The process of the AMGA2 optimization methodology is shown in the flowchart in Figure 7.1. The first step is to generate the initial population. The initial population is created using Latin Hypercube sampling (Loh, 2005) in which a random solution is found in equally spaced segments to which an unbiased Knuth shuffling is then applied within the variable space. For this specific problem an initial population size, N_i, of 40 was chosen in compliancy to a sufficient size while not extremely computational and time expensive. The next step is to evaluate the initial population utilizing FSTI for the piston/cylinder interface (described in Section 3.2) predicting the behavior of the lubricating film and the resulting losses. The archive is then updated with the results of the initial population; the archive size, N_a, being the same size as the initial population of 40. From the archive, a parent population is created based on domination level and diversity although specifically including the extreme points. The mating pool is then created comprised of a single primary parent and three auxiliary parents selected at random from the archive. By applying a differential evolution crossover (Kukkonen & Lampinen, 2005) to the mating pool the offspring population is created. The size of the offspring population, N_o, starting with the first generation and thereafter is half of the initial population in order to increase the speed while maintaining a larger archive of the best solutions; in this case the size of the corresponding offspring population is 20. By creating the offspring from a mating pool consisting of a majority of the parents selected from the archive, the offspring inherit properties from superior parents resulting in a better offspring. Finally, the resulting offspring population is evaluated using the piston/cylinder interface FSTI model in which the archive is then updated with the results. The archive is updated using a non-dominated sorting procedure across the archive and offspring in which crowded solutions are removed (Kukkonen & Deb, 2007). The resulting archive maintains a pool of good solutions throughout the sequential generations. Steps four through eight are repeated until a global minima is achieved.

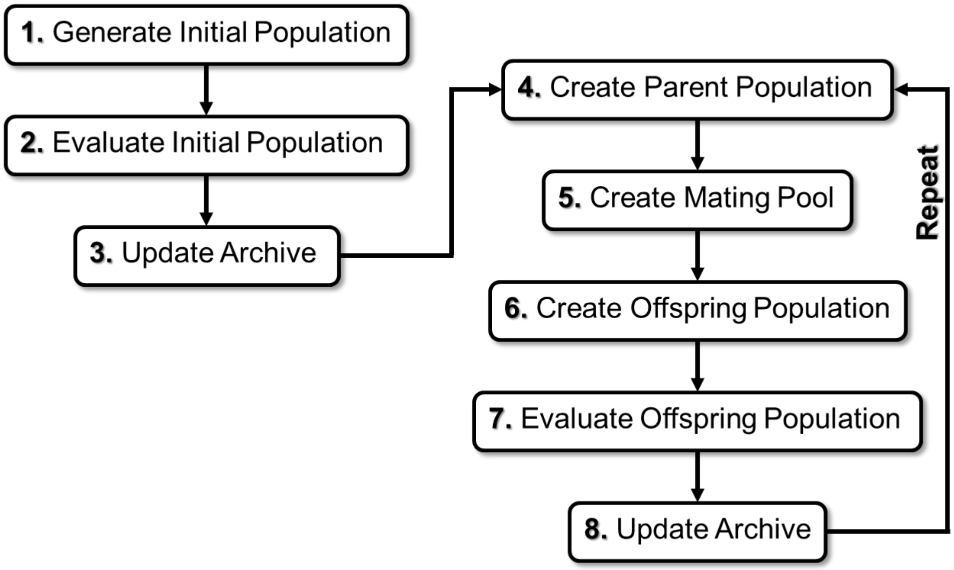

Figure 7.1. AMGA2 optimization procedure.

7.1.3 Optimization Problem

In pursuance of optimizing the surface shape of the piston via virtual prototyping, the optimization problem must be specified through objective functions and constraints that are predicted utilizing FSTI. It is of primary importance to increase the efficiency of the interface by minimizing the energy dissipation, Φ_D. In order to keep the size of the optimization problem reasonable, the energy dissipation is minimized for the three different operating conditions as shown in Eq. (7.1) and listed in Table 7.1. The reliability of the unit then becomes essential to maintain as the configuration of the interface is altered in order to change the behavior of the fluid film resulting in the desired decrease in losses. This is implemented by minimizing the maximum force additional to fluid film support required to correct the piston from contacting the bushing in the model among the five operating conditions being investigated. In this way, it is ensured that detrimental contact is not predicted to occur between the solid bodies that could lead to reduced longevity of the machine.

Minimize:
$$\Phi_D(OC2) \tag{7.1}$$
$$\Phi_D(OC3)$$
$$\Phi_D(OC5)$$
$$\max\{F_{contact}(OC1, OC2, OC3, OC4, OC5)\}$$

Additional constraints are also implemented in this optimization problem. It is first fundamental to require that the simulation completely solve under convergence for the geometry of the fluid film. If the lubrication model cannot solve for the fluid film the design is inept and will not operate in actuality. Secondly a constraint must be met that the critical areas of fluid film thickness as a percentage of the gap area for any single degree of a complete revolution among the five operating conditions under investigation must not exceed that of a machine known to operate, the production, run-in, baseline unit as was shown in CHAPTER 5. The limits presented in Eqn. (7.4) were determine based on experience from the baseline simulations. The concept of this constraint furthermore ensures that the machine will operate and continue to operate over time preventing the occurrence of detrimental contact between the solid bodies leading to failure.

Subject to:
$$Completion\{Oc1, OC2, OC3, OC4, OC5\} = 0 \tag{7.2}$$
$$\frac{\text{Critical areas}}{\text{Gap area}}(\varphi)\ (\text{OpCon1}) \leq 4.0\%$$
$$\frac{\text{Critical areas}}{\text{Gap area}}(\varphi)\ (\text{OpCon2}) \leq 0.25\%$$
$$\frac{\text{Critical areas}}{\text{Gap area}}(\varphi)\ (\text{OpCon3}) \leq 1.0\%$$
$$\frac{\text{Critical areas}}{\text{Gap area}}(\varphi)\ (\text{OpCon4}) \leq 0.15\%$$

$$\frac{\text{Critical areas}}{\text{Gap area}}(\varphi)\ (\text{OpCon5}) \leq 1.75\%$$

Table 7.1. Operating conditions considered for the optimization problem.

Operating Conditions				
OC	**Mode**	**n [rpm]**	**Δp [bar]**	**β [%]**
1	Pump	500	450	100
2	Pump	2000	300	20
3	Pump	2000	300	100
4	Pump	3600	450	20
5	Pump	3600	450	100

The operating conditions (OC) as shown in Table 7.1 were chosen for the optimization problem in order to represent a range of the unit; including some of the most troublesome operating conditions as well as the most common operating conditions. The low speed, high pressure condition, OC1 can present difficulties in supporting the external loads with the high pressure resulting in a larger side load on a slower moving piston. OC2 and OC3 are a median speed and pressure at both partial and full displacement and are included due to the frequency at which the unit will run under these conditions. The last two operating conditions, OC4 and OC5, are at a corner high speed and high pressure operating condition at partial and full displacement. These are considered due to the high power and extreme conditions in which piston is subject to resulting in large external forces that must be balanced by the fluid film. Additionally at partial displacements, the high pressure results in significant leakages in which many units are not optimized for. In the concern of evaluation time, only pumping mode was considered since it is assumed from previous results that motoring mode will have similar trends resulting in a comparable optimized design.

7.2 Barrel Surface Profile

The barrel surface profile was selected to optimize as it was shown to be the superior shape among those investigated. This barrel piston was not only shown to increase efficiency but was additionally beneficial in manipulating the geometry of the lubricating film, generating improved support at a reduced clearance to balance the external forces acting on the piston. Additionally included in this study was the optimization of the barrel surface profile on the bushing surface. This was necessary to get a better understanding of the differences of introducing a surface profile on a moving part, the piston, in comparison to a stationary body, the bushing.

7.2.1 Variable Parameters

The barrel surface shape design is defined by the variables as was shown in Section 4.3: the radius and shift of the curvature of the barrel as well as the diameter at the apex defining the minimum radial clearance between the piston and cylinder bore. These variables are to be optimized according to the above problem, concluding a design that is optimal in not only efficiency, but robustness over a range of operating conditions.

To define the surface shape from the output variables of the AMGA2, first the curvature of the barrel was created using the equation of a circle with the specified radius, r, centered along the set length, l^*, referring to the length of the piston, l_{kG}, or the length of the bushing, l_F, respectively for the two designs:

$$y = \sqrt{r^2 - l^{*2}} \tag{7.3}$$

This initial curvature of the barrel is shown in gray in Figure 7.2 and Figure 7.3 for the respective designs. The corresponding versine, or deviation at the ends due to the barrel shaping, calculated by:

$$v = r - \sqrt{r^2 - \left(\frac{l^*}{2}\right)^2} \quad (7.4)$$

,was bound between 1 micron, ensuring a barrel shape, and 20 microns, limiting the curvature on the higher end to a reasonable value in which the load will still be supported. Note that a larger radius, r, corresponds to a smaller versine, v. The versine is defined as the distance between the horizontal line connecting the points of the circle along the length of the piston, the cord, and the apex as shown in Figure 7.2 and Figure 7.3.

Next, based on the defined shift, the center of the circle was then shifted to the left or right along the length of the piston:

$$y = \sqrt{r^2 - (l^* - shift)^2} \quad (7.5)$$

Resulting in a shift in the apex of the curvature of the barrel surface as shown in black in Figure 7.2 and Figure 7.3. The shift was bound by the gap length of the piston, l_{kG}, or conversely the length of the bushing, l_F, in which a negative shift moved the center of the circle and the resulting apex toward the DC end of the gap, a positive shift toward the case end of the gap.

Once the apex was defined by this shift, the maximum diameter of the piston, d_k, or correspondingly the maximum diameter of the bushing, d_z, at the apex determined the minimum radial clearance, MRC:

$$MRC = \frac{d_z[\mu m] - d_k\ [\mu m]}{d_k\ [mm]} = 0.48‰ \text{ to } 1.64‰ \quad (7.6)$$

This clearance was bound on the upper end by the MRC of the baseline design considering that the clearance study conducted concluded that the barrel performs better with a reduced clearance. It was then bound on the lower end by manufacturability within tolerance.

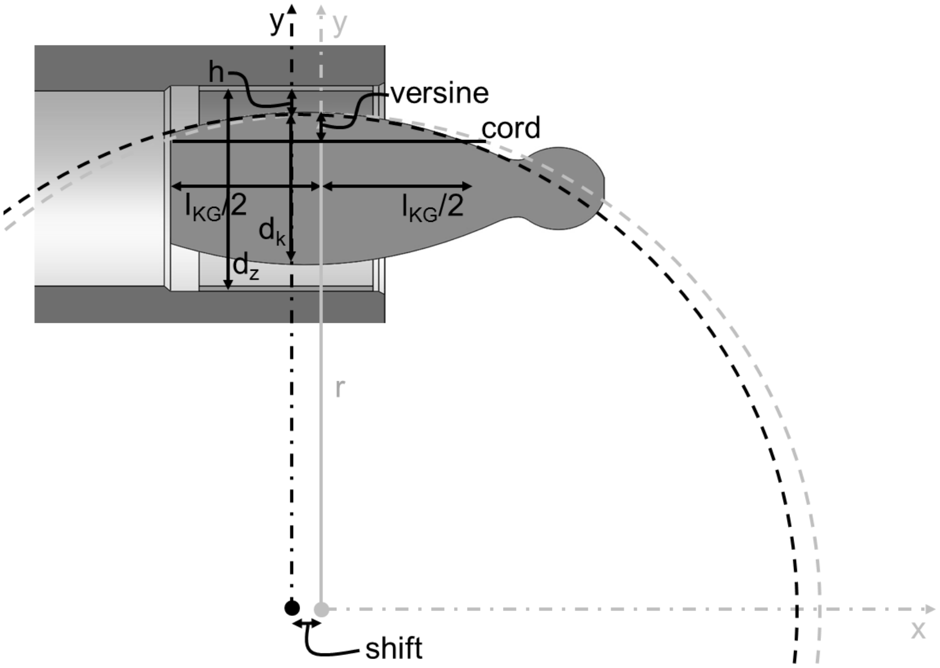

Figure 7.2. Barrel piston surface profile design optimization parameters.

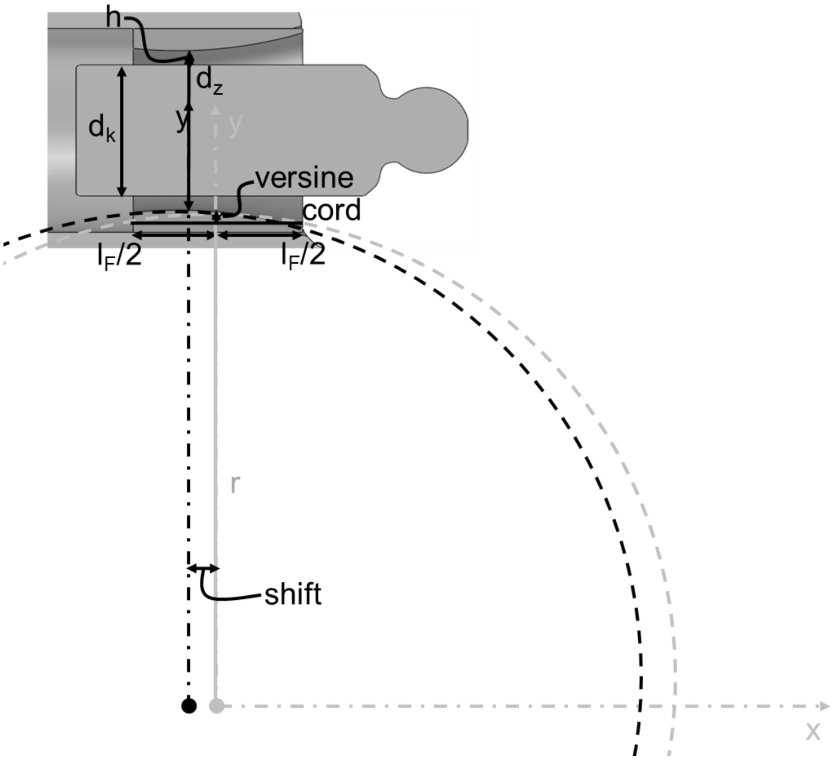

Figure 7.3. Barrel bushing surface profile design optimization parameters.

7.3 Simulation Results

Utilizing the outlined optimization technique, multiple generations of the barrel design with the characterized parameters were carried out on both the piston and the bushing. The 15 best designs for each case among the ten generations are analyzed, the design parameters listed in Table 7.2. The best designs as a result of the optimization are determined to be the designs that furthest reduce the objective functions while meeting the constraints. Note that each design is defined from the generation, G, number followed by the design, D, number in which the initial generation is denoted as 1.

Table 7.2. Best barrel design parameters; piston (left), bushing (right)

Best Barrel Piston				
Design [-]	**Design [-]**	**MRC [‰]**	**R/R_k [-]**	**Shift/l_{kg} [-]**
1	G1D33	1.14	25357	0.48
2	G1D36	1.08	35888	0.24
3	G2D1	1.16	1691	-0.19
4	G2D11	1.08	24565	0.21
5	G2D19	1.14	16480	-0.33
6	G3D1	1.13	2640	0.31
7	G4D6	1.00	13998	-0.23
8	G5D5	0.98	5280	0.01
9	G6D4	1.16	1691	0.25
10	G6D12	1.02	16779	-0.03
11	G8D5	1.13	1691	0.28
12	G8D16	1.15	16673	0.24
13	G10D4	1.25	2360	-0.22
14	G10D17	0.84	1691	0.25
15	G10D19	1.13	1844	0.25

Best Barrel Bushing				
Design [-]	**Design [-]**	**MRC [‰]**	**R/R_k [-]**	**Shift/l_{kg} [-]**
16	G1D35	1.24	1362	-0.20
17	G3D9	1.24	1475	-0.20
18	G4D14	0.89	3999	-0.37
19	G4D18	1.24	1475	-0.13
20	G5D9	1.11	947	-0.06
21	G6D9	1.27	804	-0.25
22	G6D13	1.07	1043	-0.35
23	G7D12	1.08	1043	-0.35
24	G7D15	1.28	589	-0.07
25	G8D13	1.14	1094	-0.17
26	G8D15	1.19	930	-0.07
27	G9D7	1.62	1614	-0.36
28	G9D9	1.27	1491	0.42
29	G9D15	1.28	589	-0.07
30	G10D7	1.15	483	0.02

The majority of the best designs tend to favor a more reduced clearance, a small to mid radius resulting in a larger deviation at the ends, and left shifts resulting in a larger deviation on the case end. Comparing the piston designs to the bushing designs, the ranges among the best design parameters tend to be rather similar. However, the piston design tends to favor slightly smaller clearances while the bushing design tends to favor smaller barrel radii.

For the most desirable designs listed in Table 7.2, the results are shown below in Figure 7.4 and Figure 7.5. The energy dissipation (ED) and corresponding leakages (Leak) are analyzed for the three operating conditions considered in the optimization, OC2, OC3, and OC5 (corresponding to the 2, 3, 5 labels). The results of each of the designs presented are normalized to the wear-in, baseline design; the baseline design being the worst case scenario of 1 while the best designs are less showing an improvement in the operation of the interface. Note that the plots can be read such that a normalized value of 0.6 signifies a 40% decrease from the baseline and so on. The following plots displaying the results are parallel coordinate plots in which the x-axis represents the objective or constraint function for the various operating conditions against the normalized value on the y-axis in which the different color lines signify the different designs as specified in the legend.

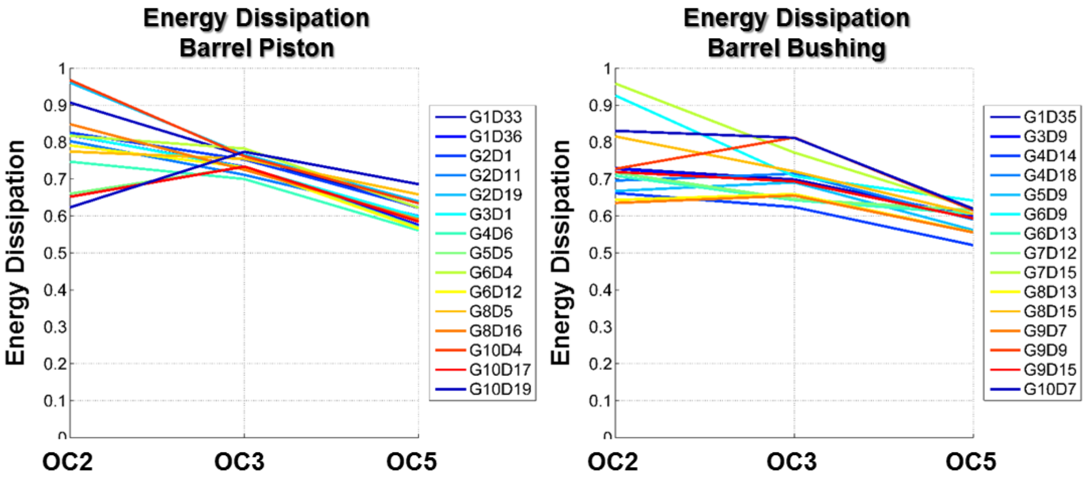

Figure 7.4. Resulting energy dissipation for the best barrel designs; piston (left), bushing (right).

According to Figure 7.4, the best designs for both the piston (left) and bushing (right) reduce the energy dissipation from the baseline for the common operating conditions (OC2 and OC3) as well as the corner power (OC5). In comparison, the barrel bushing tends to slightly reduce the energy dissipation more so than the barrel piston, by about 3-5%. Among the designs, piston G5D5 and G10D17 and bushing G4D14, G8D13, and G8D15 are the best in terms of power loss. These designs for both the piston and the bushing are defined by are largely reduced clearance, a smaller radius, and a rather moderate shift of the apex. Such design parameters allow for a reduced leakage, observed in Figure 7.5, as the tilting piston not only creates a sealing function but builds up fluid support as well.

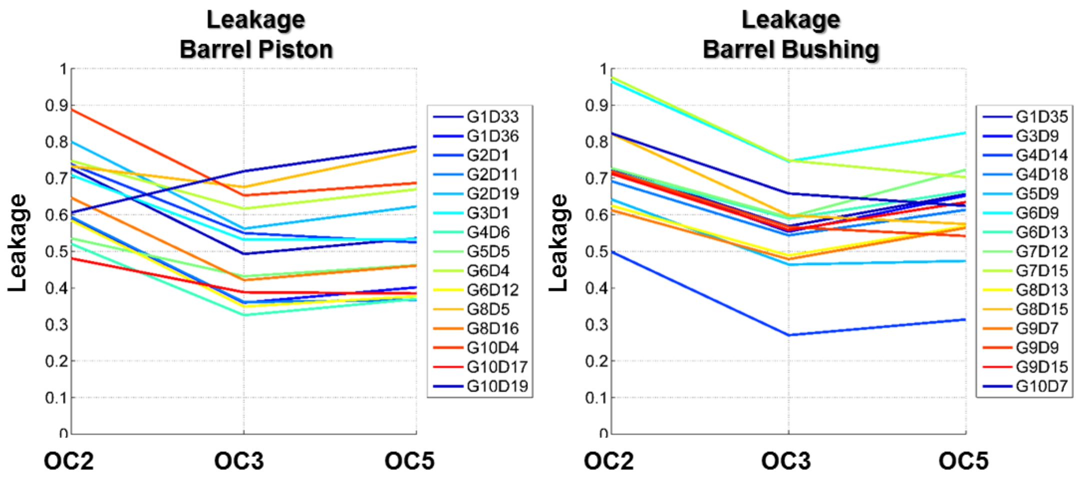

Figure 7.5. Resulting leakage for the best barrel designs; piston (left), bushing (right).

The trends explained for the energy dissipation closely reflect from the leakages, as shown in Figure 7.5. Mainly, the concept is to reduce leakages by reducing the clearance while still maintaining fluid support and in turn not greatly increasing torque losses through surface shaping.

Among the best designs listed in Table 7.2, the constraints concerning the reliability of the machine based on the fluid support were not only met, but exceeded.

7.3.1 Chosen Design

Based on the optimization investigation, the overall best designs were the piston G5D5 and bushing G8D15, shown in Figure 7.6, among the operating conditions studied. These designs have a minimum radial clearance of 0.98‰ and 1.19‰ respectively, slightly larger than the 0.72‰ that was found to be the best for the barrel studied in the design study of CHAPTER 6. Both optimal barrel designs have a very moderate shift with a smaller radii, the optimal barrel bushing having an even smaller radius resulting in an even larger deviation at the ends.

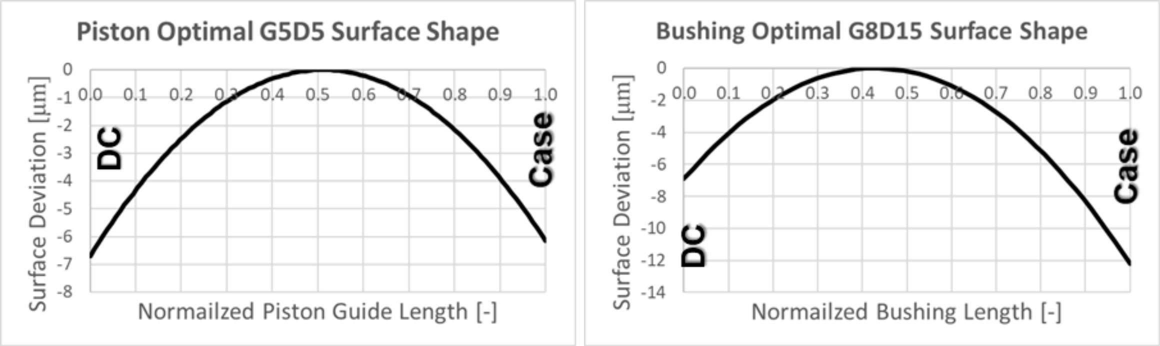

Figure 7.6. Optimal piston design (left) and bushing design (right).

These most optimal designs were chosen based on the greatly decreased losses while still exceeding the constraints of the contact forces and critical areas of fluid film thickness. As long as these specifications of fluid support are improved from an existing, operational design for the operating conditions studied, then the proposed piston/cylinder interface should operate and perform reliably.

Comparing the optimal barrel piston to the optimal barrel bushing, the reduction in energy dissipation mainly based on the reduction in leakage was very similar. The differences arise when it comes to the load support generated from each design. The barrel bushing showed better fluid support in terms of the correction forces necessary to prevent metal to metal contact between the solid bodies. However, both designs did shown a decrease from the baseline design. Therefore, with similar efficiency and evidence to support that each design would perform, the final deciding factor between the two designs becomes the cost and feasibility of manufacturing.

CHAPTER 8. SURFACE SHAPING MEASUREMENT COMPARISON

In order to utilize the fluid structure thermal interaction model (FSTI) for design and optimization of the lubricating interfaces, in turn saving time and money as opposed to the traditional, empirical trial and error method, the model must be validated under such analysis. Using specialized test rigs equipped with sensors to precisely measure the behavior of the fluid film interfaces, comparison of the predicted performance can be made with the measurements to prove the model is capable of accurate replication of real world occurrence.

In the following case, measurements were conducted on a specialized test rig, the EHD, of various dynamic fluid film parameters within the gap of the piston/cylinder interface under normal operating conditions. These parameters specifically include the pressure and temperature fields as well as the leakage isolated to 2 interfaces, the piston/cylinder and slipper/swashplate. Considering this model is being used to improve the piston/cylinder interface via surface shaping, a barrel piston was implemented for the measurements.

8.1 The EHD test rig

The EHD test rig, specialized to measure the elastrohydrodynamics of the piston/cylinder interface was used to validate the capabilities of the model. The single piston pump, displayed in Figure 8.1, utilizes reverse kinematics via a rotating swashplate at a 17° degree angle realizing the reciprocating motion of the piston in and out of a fixed cylinder bore.

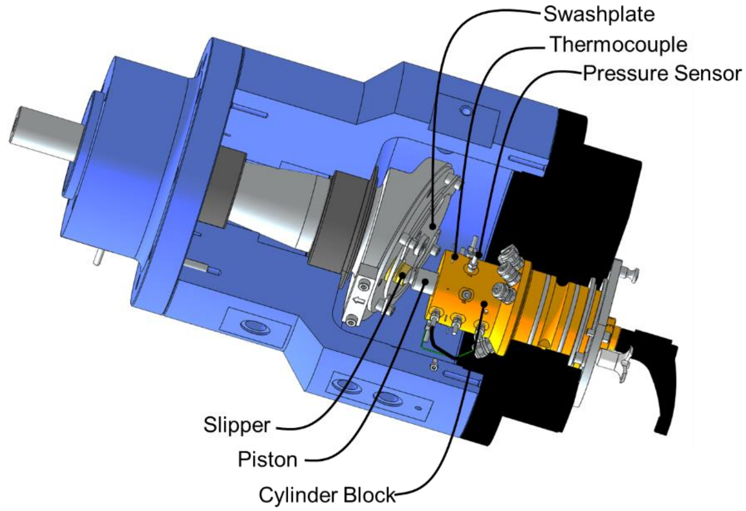

Figure 8.1. EHD test rig pump.

While the reverse kinematics permits normal operating conditions of the piston/cylinder interface, it is essential in equipping the block with sensors in order to measure the pressure and temperature of the fluid film between the piston and cylinder. The specialty block was designed for 9 piezoelectric pressure sensors and 9 thermocouples spaced around the cylinder at variable lengths and circumferences as shown in Figure 8.2. It can be seen that the thermocouples are installed flush with the cylinder bore while the pressure sensors are installed slightly recessed, the fluid reaching the sensor by means of a capillary drilled through the surface. Due to space constraints, the thermocouples are 180° offset in order to measure at the same axial location around the bore i.e. pressure sensor 1 and 9 are on the same circumferential position as thermocouple 5.

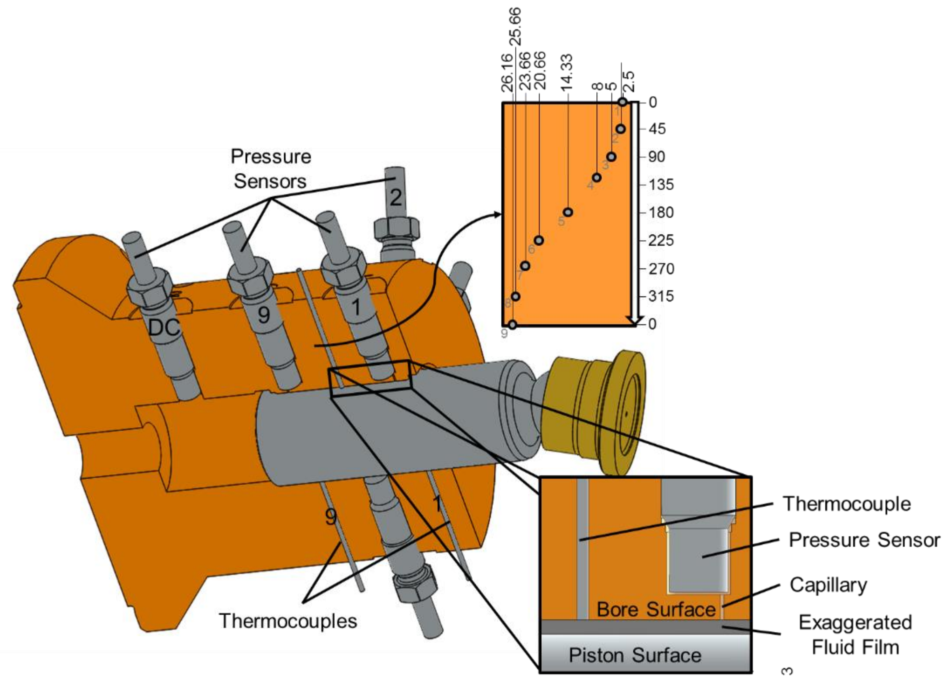

Figure 8.2. Location of sensors within EHD cylinder block.

8.2 Measurement Methodology

The entire purpose of the reverse kinematics of the specialized pump is such that a fixed cylinder block can be equipped with sensors allowing for simple data transfer. Therefore, in order to obtain a complete pressure field in the lubricating fluid film between the piston and the cylinder along with the cylinder surface temperature field around the gap interface, measurements are to be taken as the block is rotated by hand to a possible 180 different angular positions. The block can be rotated to 180 unique angular combinations by utilizing the fixed plate at the end of the cylinder block, having 20 fixed positions (A-T), to lock the block into 9 difference positions with the locking pin as shown in Figure 8.3 in position A1. This results in up to a 2°accuracy around the lubricating gap with a possible 1620 measurement points among the 9 sensors.

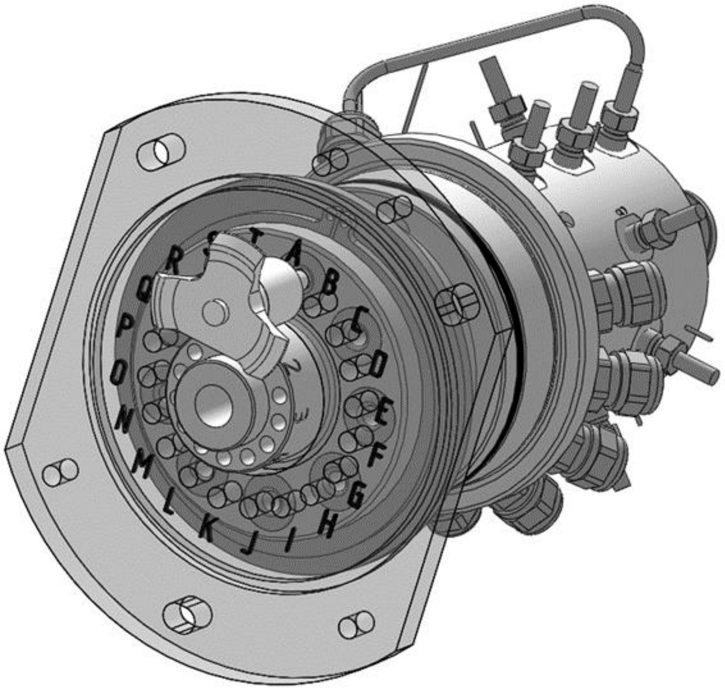

Figure 8.3. Locking device for the EHD cylinder block.

Note that for this particular set of measurements, only 7 thermocouples were able to be measured for 18 measurement positions. The positions were at A and K on the fixed plate for every 9 positions around the cylinder block equating to 20° increments around the circumference of the lubricating gap. On the other hand, it was possible to achieve a finer grid of measurements for the pressure field. In this case, 6 pressure sensors were utilized to measure 36 positions. Not only were A and K measured, but F and P were measured for the pressure field as well at all 9 rotations of the cylinder block generating a grid resolution of every 10° around the piston/cylinder gap.

As can be observed in Figure 8.4, the inlet temperature (T_{LP}) was recorded in order to ensure that the ISO 4409 standard of a constant inlet temperature was maintained. Also recorded were the corresponding case and outlet temperatures (T_C and T_{HP}) to be later used as accurate boundary conditions in simulation. Note that the case temperature was directly measured in the case. The high pressure (p_{HP}) and low pressure (p_{LP}) lines are measured in order to accurately set the desired operating pressure; controlled by relief valves (8) and (9) respectively. The high pressure accumulator (6) was set at 150bar while the low pressure accumulator (7) set to 17 bar in order to reduce the pressure pulsations in the lines. The desired rotational speed (n) was set through the controls of the water cooled 60kW electric motor (2). The motor is connected to the pump (1) and a flywheel (3) via disc type couplings. The flywheel is necessary to increase the mass inertia of the drive shaft, counteracting the oscillating speed. Furthermore, a shaft encoder was also integrated in order to know the exact location of the rotating swashplate triggering the measurements of the temperatures and pressures within the gap. Note that the pressure (p_g) measurements are collected and recorded over three A/D boards PCI DAS4020 while the temperatures (T_g) are collected and recorded using an A/D board PCI DAS 1000. Also recorded on this board is the high pressure (p_{HP}), the low pressure (p_{LP}), and the return flow measured using a gear flow meter. The combined leakages from the gap of the piston/cylinder interface and the slipper/swashplate interface can also be measured using a beaker to collect the flow diverted from the drain through a ball valve (11) over a period of 60 seconds. Although it is also an option to close the ball valve on the return line (10) diverting the flow back into the case, this option was not employed for the following measurement set. The specific sensor used are listed in Table 8.1.

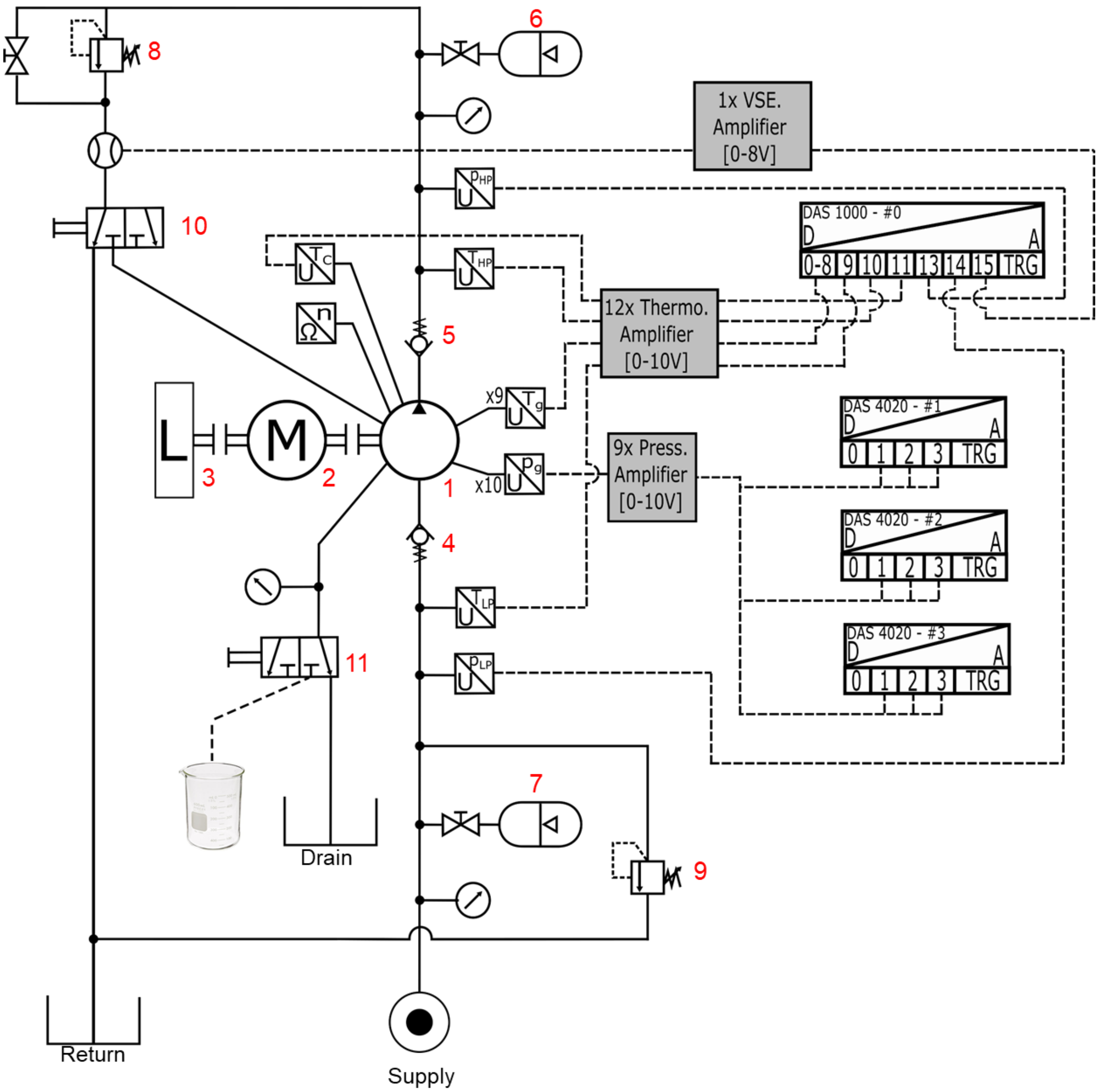

Figure 8.4. Circuit diagram of the EHD test rig (Pelosi, 2012).

Table 8.1. EHD test rig measurement sensors.

Sensor	Measurement	Principle	Range	Output	Accuracy
Heidenhain ERN	Shaft Encoder	Rotary encoder	0-10000rpm		
Keller PA-21-50	Low Pressure	Piezoresistive	0 - 50 [bar]	1-10 VDC	± 0.2 %
Keller PA-21-400	High Pressure	Piezoresistive	0 - 400 [bar]	1-10 VDC	± 0.2 %
Kistler 4065A	DC and Gap Pressures	Piezoresistive	0 - 1000 [bar]	1-10 VDC	± 0.5 %
VS1E	HP Flow	Gear flow meter	0.05 - 80 [l/min]	10-16 VDC	± 0.3 %
Omega Type K	Temperature	Junction end thermoelements	180 - 1300 [°C]	N/A	±1.5 (−40 - 375 °C)

8.3 Numerical Analysis

Since it has been demonstrated that the surface profiles of the solid bodies have a large effect on the fluid film geometry, the barrel piston as well as the run-in wear on the bushing and slipper, Figure 8.5, were measured (measured as explain in Section 5.2) and used as exact inputs to the simulation tool. Note that the bushing in this case is averaged and assumed as circumferentially symmetric as the block is turned 360° while measuring the pressure and temperature field.

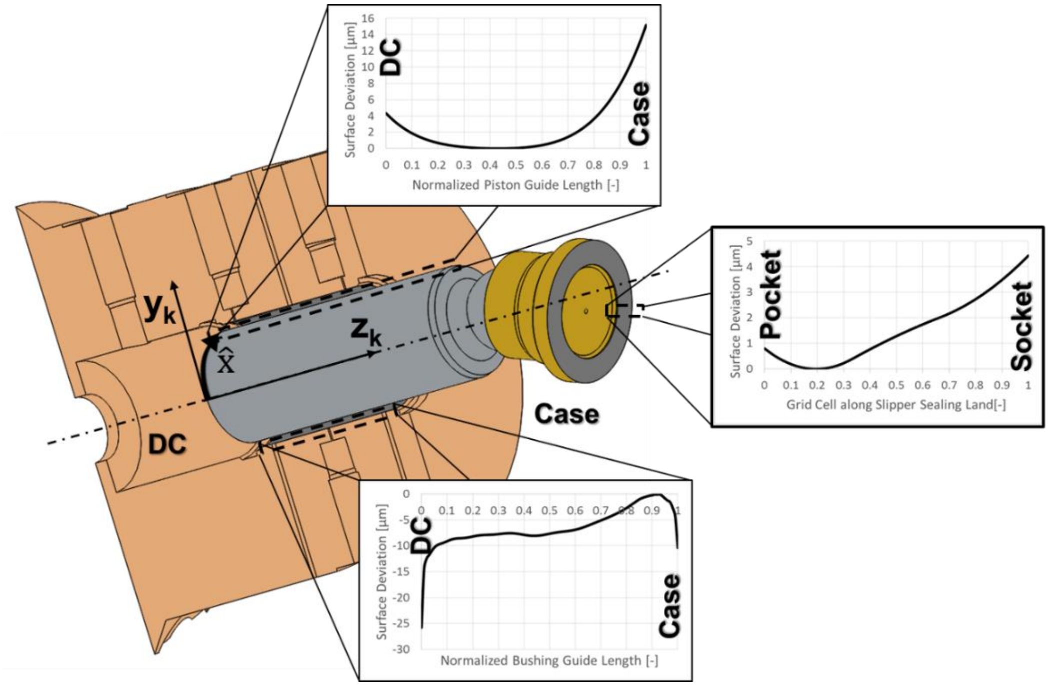

Figure 8.5. Piston, bushing, and slipper measured wear profiles.

The numerical analysis was performed at the one operating condition in which the measurements were conducted. The measured and subsequently simulated measurement parameters are reported in Table 8.2. It is important to note that for this set of measurements, the case temperature was directly measured in the case rather than on the drain line in order to ensure that inaccuracies were not introduced in the temperature.

Table 8.2. EHD operating conditions.

Parameter	Condition	Units
Rotational Speed	1500	rpm
Low Pressure	25	bar
High Pressure	300	bar
Case Temperature	73.5	°C
Temperature at Low Pressure Port	42	°C
Temperature at High Pressure Port	49	°C

The measured displacement chamber pressure, Figure 8.6, must be used as an input parameter to the simulation since the specialized EHD test pump utilizes check valves to control the high and low pressures exceeding the capabilities of FSTI that is limited to predicting typical pressure profile generated based on a the opening and closing of the ports via the valve plate to the displacement chambers.

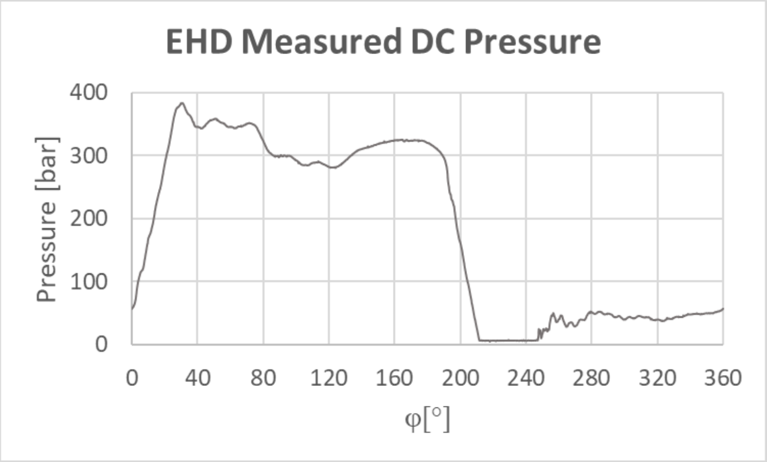

Figure 8.6. Measured DC pressure profile.

In reference to Figure 8.6, between 0° and 180° the pressure rises in the displacement chamber reaching the average pressure setting on the loading relief valve throughout the high pressure stroke. Starting at 180° the displacement chamber transitions into the suction stroke and the pressure falls.

The thermal and pressure mesh for the steel piston, brass cylinder block, and bronze slipper are shown in Figure 8.7 with the labeled boundaries.

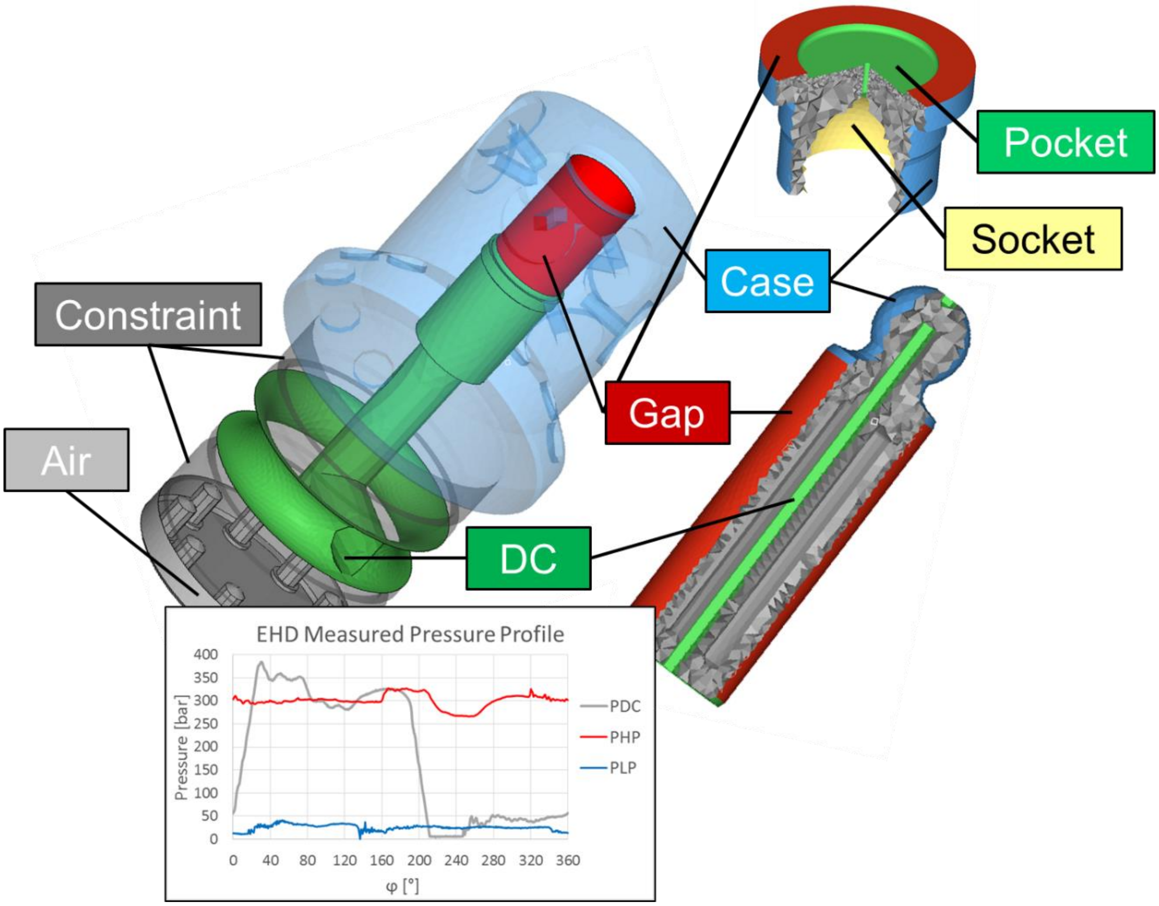

Figure 8.7. Boundary conditions for solid parts.

The piston is constrained using an inertia relief method as the piston is free to move within the bore. However, the cylinder block is constrained as represented in Figure 8.7 since it is physically fixed to the end case of the EHD and does not have a free range of motion during operation. For more in depth information on the boundary conditions refer back to Section 5.3 and 5.4 respectively for the piston/cylinder and slipper/swashplate interfaces.

8.4 Measurement and Simulation Comparison Results

In this section the measured fluid film pressure and temperature field occurring between the piston and the cylinder of the EHD test pump are compared to the results of the numerical model.

Figure 8.8, shows a side by side comparison of the unwrapped gap pressure field at various instances of a shaft revolution in the high pressure stroke, starting at φ=0 where piston is at ODC. Note that the low pressure stroke is not shown as the lower pressure creates a stable, constant fluid film in which the simulation adequately matches the measured data. The unwrapped gap is defined as the x-axis $(\hat{y})$ corresponding to the gap length and the y-axis $(\hat{x})$ corresponding to the circumference around the fluid film of the piston/cylinder interface. The pressure field is represented by 6 working pressure sensors that were measured in 36 positions by rotating block producing a resolution of every 10°.

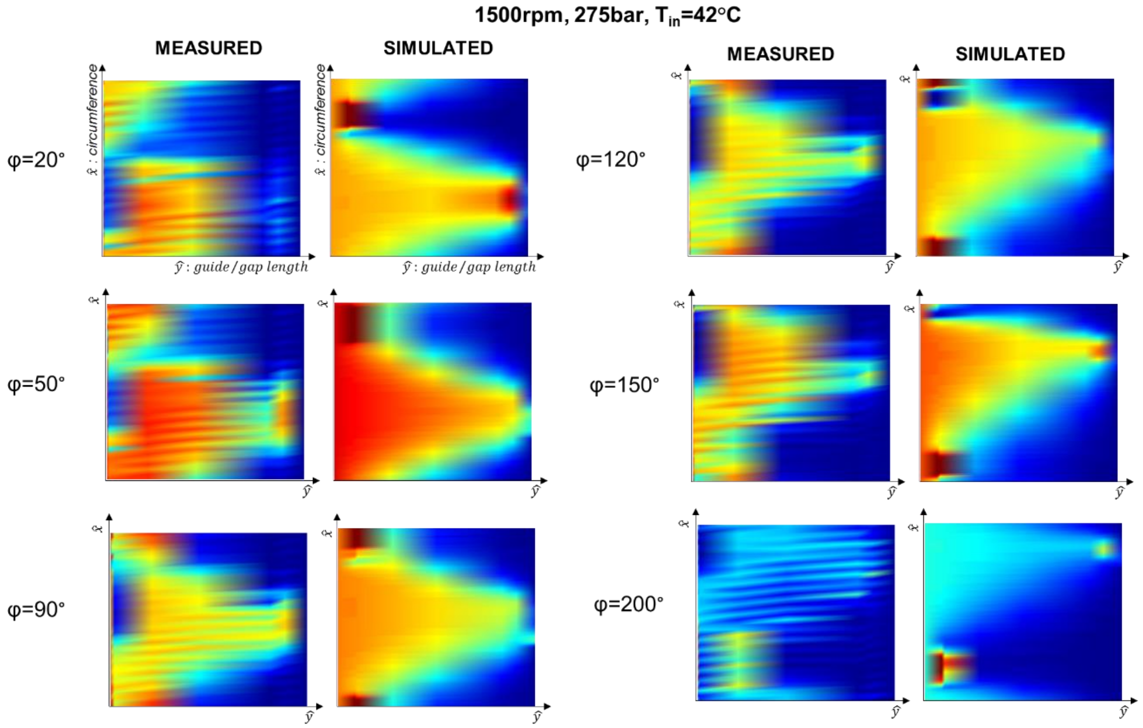

Figure 8.8. EHD barrel piston pressure field at specific instances for 1500rpm, 275bar, T_{in}=42°C; measure (left) vs. simulated (right).

The dynamic trends of pressure over the fluid film within the gap are similar in comparison between the measured and simulated results. Throughout the high pressure stroke, the high pressure from the DC transitions over the length of the gap to the low case pressure as expected. In the case of the EHD test rig, the rotating swashplate is angled resulting in the reciprocation of the piston while this motion then introduces the side load acting on the piston causing it to tilt within the bore. Due to this tilting of the piston, the barrel shape helps to create a squeeze effect in the fluid resulting in spikes in the pressure on the circumferentially opposing sides on the DC and case end of the gap in order to balance the external loads. This phenomenon can also be noted in very similar locations in both the measurement and simulation results. Although the resolution of the simulation is much better and the measurements have a limitation in capturing the pressure spikes due to the 0.3mm fluid capillaries of the pressure sensors, the simulation tool is shown to very closely predict the phenomena occurring within the fluid film between the piston and the cylinder.

A steady state surface temperature distribution field around the cylinder bore was measured utilizing 7 thermocouples measured in 18 positions of the EHD block equating to every 20 degrees increments of the circumference over the length of the gap interface and compared to the result of the simulation, Figure 8.9.

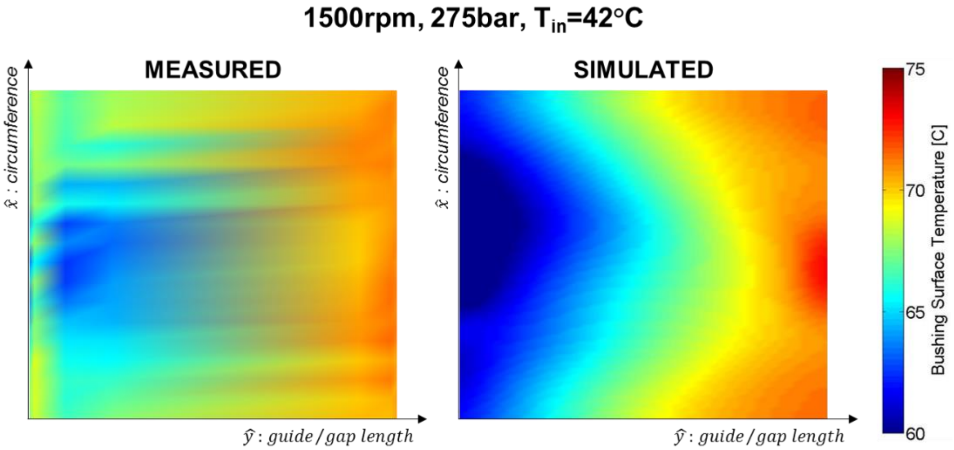

Figure 8.9. EHD barrel piston temperature field for 1500rpm, 275bar, T_{in}=42°C; simulated (left) vs. measured (right).

Utilizing the measured case temperature and measured DC temperature as boundary inputs into the simulation tool, the model is able predict the temperature distribution relatively well; the limitation again being the resolution of the measured data. It can be seen in both cases that over the length of the gap, the temperature tends to increase from the lower DC temperature of 45.5°C to the case temperature of 73.5°C. The absolute values of the increase in temperature over the length of the gap is predicted with a high level of accuracy.

Furthermore, a combined leakage of the piston/cylinder interface and slipper swashplate interface could be measured and compared to simulation results, Table 8.3. The leakage was measured as previously described according to the circuit diagram in Figure 8.4. The drain flow from the piston/cylinder and slipper/swashplate interface was collected in a 500mL beaker (±5% volumetric accuracy) over 60 seconds. The flow over time could then be calculated. An average of multiple measurements was taken to obtain the reported value.

Table 8.3. EHD operating conditions.

Leakage [l/min]		
Simulated		
Piston	**Slipper**	**Total**
0.37	0.01	0.38
Measured		
Total		
0.27		
% Diff		
28.95		

In this case, it can be noted that simulation tool is actually over predicting the leakages between the two interfaces by almost 29%. At this operating condition for a single piston and slipper design, the leakages are quite low and therefore, the difference between the measurement and the predicted leakages are rather reasonable further validating the fluid-structure interaction model.

Based on the comparison of the simulated pressure and temperature fields as well as the leakages of two isolated interfaces to the measured data, it can be concluded that the simulation tool can be used to correctly predict the behavior of the fluid film of the piston/cylinder interface while studying surface shaping of the piston.

CHAPTER 9. CONCLUSIONS

This research began with a comprehensive measurement / simulation study that for the first time compared and validated simulation results obtained with Maha’s newest fluid structure interaction model (FSTI) for a stock unit running in pumping and motoring mode over its entire range of operation. This initial simulation and measurement study opened the way for the first extensive investigation on micro-surface shaping for the piston/cylinder interface considering solid body micro-motion, dynamic loading and surface deformation due to temperature and pressure as well as the impact of the fluid and material properties. Analysis was conducted on the stability of the fluid film, the creation of the elasto-hydrodynamic pressure build up and the resulting load carrying ability as well as the energy dissipation, leakage, and friction, along with the temperature of the fluid film, the temperature of the piston and cylinder surfaces, and the resulting case and port temperatures. Very different surface shapes and their impact on the piston/cylinder interface behavior in general have been studied and analyzed. From this extensive study, a better understanding of the physical phenomena occurring within the lubricating gap was achieved. Thus, through micro-surface shaping of the piston, the fluid film geometry could be strategically manipulated to increase fluid support in which the clearance could then be reduced in order to decrease the leakage without largely increasing the torque losses. Thereby, it was concluded that micro-surface of the piston could improve upon the efficiency and reliability of an axial piston machine. It was found that the barrel surface profile at a reduced clearance can improve the overall performance of an axial piston machine operating in pumping and motoring mode most overall.

Based on the comprehensive surface shaping investigation study~~,~~ a novel virtual prototyping method was proposed and utilized to optimize a piston as well as a bushing design based on the barrel piston shape. The biggest benefit of the barrel surface shape is that it reduces the correction forces along the gap over a full range of operating parameters while increasing the efficiency of the interface.

Based on the comparison of the simulated pressure and temperature fields as well as the leakages of two isolated interfaces to the measured data, it can be concluded that the simulation tool can be used to correctly predict the behavior of the fluid film of the piston/cylinder interface while studying surface shaping of the piston.

In summary the following original contributions were made:

- For the first time, the most up-to-date, novel fully coupled fluid structure interaction model (FSTI) was used to study and compare the three tribological interfaces of a stock axial piston machine with comprehensive steady state measurements over the full range of operating conditions.
- For the first time, a comprehensive simulation study of the influence of piston micro-surface shaping on the energy dissipation, leakage, and friction losses along with the load carrying ability and fluid film stability has been conducted utilizing Maha’s newest FSTI simulation model for the piston/cylinder interface.
- The effect of the clearance between the piston and the cylinder on the performance of the interface has been studied for the first time considering the effect of various novel micro-surface shaped piston designs.
- For the first time, a comprehensive study of the influence of surface shaping of both the piston and the cylinder on the fluid film geometry, load carrying ability, and the resulting energy dissipation of the piston/cylinder interface has been conducted.

- For the first time, a detailed analysis of the temperature distribution across the lubricating gap as well as the thermal behavior of the cylinder and the impact on the port and case temperature of the axial piston unit due to piston surface shaping at reduced clearances has been conducted.
- An optimization algorithm method was proposed and utilized to optimize a barrel micro-surface shaped piston or bushing to achieve the best load carrying ability and highest efficiency over the entire range of operating conditions in pumping and motoring mode.
- The EHD test rig was utilized to measure the temperature and pressure distribution of the lubricating film between the barreled shaped piston and the cylinder as well as the leakage from the piston/cylinder and slipper/swashplate interface at a more demanding operating condition of increased speed and pressure.

A. CORNER OPERATING CONDITIONS

Below is a list of the corner operating conditions of the unit studied. Note that the outlet and case temperatures were predicted utilizing an iterative method between FSTI predicted losses and the predicted temperatures of the thermal model.

Table A.1. Baseline corner operating conditions in pumping mode at T_{in}=52°C.

Operating Conditions						
Mode	**n [rpm]**	**Δp [bar]**	**β [%]**	**T_{in} [°C] (lp)**	**T_{out} [°C] (hp)**	**T_{case} [°C]**
Pumping 100% beta						
Pump	500	50	100	52	52.52	46.56
Pump	500	450	100	52	56.68	59.45
Pump	3600	50	100	52	52.70	60.72
Pump	3600	450	100	52	56.33	72.87
Pumping 20% beta						
Pump	500	50	20	52	55.82	53.51
Pump	1500	350	20	52	61.74	68.44
Pump	3600	50	20	52	53.24	60.09
Pump	3600	450	20	52	62.63	69.34

Table A.2. Baseline corner operating conditions in motoring mode at T_{in}=52°C.

Operating Conditions						
Mode	**n [rpm]**	**Δp [bar]**	**β [%]**	**T_{in} [°C] (hp)**	**T_{out} [°C] (lp)**	**T_{case} [°C]**
Motoring 100% beta						
Motor	500	50	100	52	51.73	47.49
Motor	500	450	100	52	49.31	55.56
Motor	3600	50	100	52	51.86	57.94
Motor	3600	450	100	52	49.24	64.89
Motoring 20% beta						
Motor	500	100	20	52	53.01	53.81
Motor	500	450	20	52	60.32	64.45
Motor	3600	50	20	52	52.41	59.72
Motor	3600	450	20	52	52.26	64.12

Table A.3. Baseline corner operating conditions in pumping mode at T_{in}=75°C.

Operating Conditions						
Mode	**n [rpm]**	**Δp [bar]**	**β [%]**	**T_{in} [°C] (lp)**	**T_{out} [°C] (hp)**	**T_{case} [°C]**
Pumping 100% beta						
Pump	500	50	100	75	75.66	69.43
Pump	500	450	100	75	83.97	100.95
Pump	3600	50	100	75	76.15	92.75
Pump	3600	450	100	75	81.36	126.1
Pumping 20% beta						
Pump	500	50	20	75	80.11	76.67
Pump	1500	350	20	75	84	83.75
Pump	3600	50	20	75	77.03	87.77
Pump	3600	450	20	75	68.59	89.48

Table A.4. Baseline corner operating conditions in motoring mode at T_{in}=75°C.

Operating Conditions						
Mode	**n [rpm]**	**Δp [bar]**	**β [%]**	**T_{in} [°C] (hp)**	**T_{out} [°C] (lp)**	**T_{case} [°C]**
Motoring 100% beta						
Motor	500	50	100	75	74.63	67.67
Motor	500	450	100	75	71.93	73.3
Motor	3600	50	100	75	75.27	108.11
Motor	3600	450	100	75	72.75	99.55
Motoring 20% beta						
Motor	500	100	20	75	74.51	72.37
Motor	500	450	20	75	76.86	81.72
Motor	3600	50	20	75	77.21	103.24
Motor	3600	450	20	75	76.52	95.43

B. BASELINE SIMULATED LEAKAGES

A break-down of the overall simulated leakage for each interface is shown in Table B1.

Table B.1. Predicted leakages of each interface.

Operating Conditions		**Leakage [l/min]**		
n [rpm]	**Δp [bar]**	**Piston**	**Slipper**	**Block**
Pumping 100% beta				
500	5	0.09	0.02	0.001
500	50	0.16	0.15	0.003
500	100	0.26	0.10	0.006
500	200	0.49	0.04	0.021
500	300	0.79	0.05	0.052
1000	5	0.11	0.03	0.001
1000	50	0.20	0.04	0.005
1000	100	0.30	0.08	0.01
1000	200	0.55	0.04	0.05
1000	300	0.85	0.10	0.07
2000	5	0.07	0.56	0.002
2000	50	0.25	0.67	0.01
2000	100	0.39	0.72	0.04
2000	200	0.69	0.33	0.05
2000	300	1.05	0.27	0.11
2600	5	0.07	0.75	0.006
2600	50	0.24	1.01	0.02
2600	100	0.41	1.08	0.06
2600	200	0.75	0.76	0.07
2600	300	1.03	0.48	0.13
3200	5	0.19	0.87	0.01
3200	50	0.51	1.22	0.03
3200	100	0.79	1.20	0.08
3200	200	1.21	1.09	0.09
3200	300	1.73	0.50	0.15

n [rpm]	**Δp [bar]**	**Piston**	**Slipper**	**Block**
Pumping 20% beta				
1000	100	0.67	1.42	0.01
1000	300	2.93	1.02	0.06
2000	100	0.51	2.02	0.03
2000	300	2.34	2.08	0.09
2800	300	2.64	2	0.14

The piston/cylinder interface contributes as a majority of the volumetric losses among the three interfaces, especially so at full displacements. A strong trend is shown that the leakage increases more so with pressure than speed. This develops as the higher pressures force fluid from the gap. At partial displacements, the increase in pressure has an even more drastic effect on leakages whereas speed actually tends to have the reverse effect. Since piston is not as tilted within the bore at the partial displacements, the fluid flows more easily from the gap with the increase in pressure. However, as the speed increases, the piston starts to tilt slightly more resulting in a better sealing function than at the lower speeds.

Adversely, in some instances, the slipper/swashplate interface decreases in contributed leakages with the increase in pressure while mostly increasing with speed. The effects due to pressure occur as the increased pressure in the pocket of the slipper forcing fluid from the gap is counteracted as the increased pressure forces press the slipper toward the swashplate decreasing the fluid film thickness. For partial displacements, the slipper leaks much more, the reduced forces resulting in a more tilted slipper with larger fluid film thickness.

The cylinder block/valve plate has a very minimal contribution to the overall leakages in comparison to the other two interfaces. Although, it does hold that the leakages do tend to increase with both the operating speed and pressure. Unlike the piston/cylinder interface and the slipper/swashplate interface, this interface shows little difference between full and partial displacements.

BIBLIOGRAPHY

Baker, J. (2008). *Power losses in the lubricating gap between cylinder block and valve plate of swash plate type axial piston machines.* Purdue University, MS Thesis.

Baker, J., & Ivantysynova, M. (2009). Advanced surface design for reducing power losses in axial piston machines. *International Conference on Fluid Power, 10*, pp. 15-30. Linköping, Sweeden.

Baker, J., & Ivantysynova, M. (2009). Power loss in the lubricating gap between cylinder block and valve plate of swash plate type axial piston machines. *International Journal of Fluid Power, 10*(2), 29-43.

Bergada, J. M., Davies, D. L., Kumar, S., & Watton, J. (2011). The effect of oil pressure and temperature on barrel film thickness and barrel dynamics of an axial piston pump. *Meccanica*, 639-654.

Bergada, J., Watton, J., & Kumar, S. (2008). Pressure, flow, force, and torque between the barrel and port plate in an axial piston pump. *Journal of Dynamic Systems, Measurement, and Control, 130*(1), 16.

Deeken, M. (2003). Simulation of the tribological contacts in an axial piston machine. *O+ P Ölhydraulik und Pneumatik, 47*, 11-12.

Donders, S. (1998). *Kolbenmaschinen für HFA flüssigkeiten - verlustanteile einer schrägsheibeneinheit.* Dissertation RWTH Aachen, Germany.

Dowd, J. R., & Barwell, F. T. (1975). Tribological interaction between piston and cylinder of a model high pressure pump. *Tribology Transactions*, 21-30.

Franco, N. (1961). Pump design by force balance. *Hydraulic and Pneumatic, 14*(11), 101-107.

Fredrickson, A. (2008). *Study of the piston and cylinder interface of an axial piston pump using an advanced computer model.* Purdue University, MS Thesis.

Garret, R. (2009). *Investigation of reducing energy dissipation in axial piston machines of swashplate type using axially waved pistons.* Purdue University, MS Thesis.

Gels, S., & Murrenhoff, H. (2010). Simulation of the lubrication film between contoured piston and cylinder. *International Journal of Fluid Power, 11*(2), 15-24.

Hargreaves, D. J. (1991). Surface waviness effects on the load-carrying capacity of rectangular slider bearings. *Wear, 145*, 137-151.

Hibbert , G., Lindsay, D. V., Shute, N. A., & Turnbull, D. E. (1971). The balancing of piston and valveplate forces in axial piston pumps and motors. *Technical Report British Hydromechanics Research Association*.

Huang, C., & Ivantysynova, M. (2003). A new approach to predict the load carrying ability of the gap between valve plate and cylinder block. *Proceedings of the Bath Workshop on Power Transmission and Motion Control PTMC*, (pp. 225-239). Bath, UK.

Ivantysyn, J., & Ivantysynova, M. (2002). *Hydrostatic Pumps and Motors* (First English Edition ed.). (S. N. Ali, Trans.) New Delhi, India: Tech Books International.

Ivantysynova (Berge), M. (1983). *An Investigation of Viscous Flow in Lubricating Gaps (Dissertation in Slovak).* Czechoslovakia: SVST Bratislava.

Ivantysynova, M. (2012). The Piston Cylinder Assembly in Piston Machines - a Long Journey of Discovery. *Hidrostaticni Pogoni*, pp. 374-385.

Ivantysynova, M., Huang, C., & Behr, R. (2005). Measurements of elastohydro-dynamic pressure field in the gap between the piston and cylinder. *Bath Workshop on Power Transmissions and Motion Control PTMC 2005*, (pp. 451-465). Bath, UK.

Jacazio, G., & Vatta, F. (1981). The block-lift in axial piston hydraulic motors. *Proceedings of the ASME/ASCE Bioengineering, Fluids Engineering and Applied Mechanics Conference*, (pp. 1-7). Boulder, Colorado, USA.

Jouini, N., & Ivantysynova, M. (2008). Valve plate surface temperature prediction in axial piston machines. *Proceedings of the 5th FPNI PhD Symposium*, (pp. 95-110). Cracow, Poland.

Kim, J. K., & Jung, J. Y. (2003). Measurement of fluid film thickness on the valve plate in oil hydraulic axial piston pumps (Part I- bearing pad effects). *KSME International Journal, 17*(2), 246-253.

Kim, J. K., Kim, H. E., & Oh, S. H. (2005). Measurement of fluid film thickness on the valve plate in oil hydraulic axial piston pumps (Part II- sperical design effects). *Journal of Mechanical Science and Technology, 19*(2), 655-663.

Kleist, A. (1997). Design of hydrostatic bearing and sealing gaps in hydraulic machines - a new simulation tool. *International Conference on Fluid Power (SICFP'97)*, (pp. 157-169). Linkoeping, Sweden.

Kukkonen, S., & Deb, K. (2007). *A fast and effective method for pruning of non-dominated solutions in many-objective problems.* Technical report, Indian Institute of Technology, Kanpur, India.

Kukkonen, S., & Lampinen, J. (2005). GDE3: the third evolution step of generatlized differential evolution. *Proceedings of the IEEE congress on evolutionary computation (CEC 2005)*, (pp. 443-450). Edinburgh, UK.

Lasaar, R. (2003). *Eine untersucung zur mikro- und makro-geometrischen gestaltung der kolben/zylingerbaugruppe von schägscheibenmaschinen.* Dissertation VDI Verlag Düddrldorf, Germany.

Loh, W. L. (2005). On Latin hypercube sampling. *Annals of Statistics, 33*(6), 2058-2080.

Manring, N. D. (2000). Tipping the cylinder block of an axial piston swash-plate type hydrostatic machine. *Journal of Dynamic Systems Measurements and Control*, 216-221.

Manring, N. D., Johnson, R. E., & Cheruki, H. P. (2002). The impact of linear deformations on stationary hydrostatic thrust bearings. *Journal of Tribology, 124*(4), 874-877.

Matsumoto, K., & Ikeya, M. (1991). Friction and leakage characteristics between the valve plate and cylinder for starting and low speed conditions in a swashplate type axial piston motor. *Transactions of the Japan Society of Mechanical Engineers - Part C 57*, 2023-2028.

Oberem, R. (2002). *Unterschung der tribosysteme von schägscheibenmaschinen der HFA-Hydraulik.* Disseration RWTH Aachen, Germany.

Olems, L. (2000). Investigation of the temperature behaviour of the piston cylinder assembly in axial piston pumps. *International Journal of Fluid Power, 1*, 27-38.

Olems, L. (2001). *Ein beitrag zur bestimmung des temperaturverhaltens der kolben-zylinderbaugruppe von axialkolben maschinen der schägscheibenbau-weise.* Dissertation VDI Verlag Düsseldorf, Germany.

Pelosi, M. (2012). *An Investigation of the fluid-structure interaction of piston/cylinder interface.* Ph.D. Thesis, Purdue University.

Pelosi, M., & Ivantysynova, M. (2009). A novel thermal model for the piston/cylinder interface of piston machines. *ASME/Bath Symposium on Fluid Power and Motion Control (FPMC2009),* (pp. 37-44). Hollywood, California, USA.

Pelosi, M., & Ivatysynova, M. (2011). The influence of pressure and thermal deformation on the piston/cylinder interface film thickness. *Proceedings of the 52nd National Conference on Fluid Power 2011, NCFP I11-9.3.*

Pelosi, M., & Ivatysynova, M. (n.d.). Surface deformation enables high pressure operation of axial piston pumps. *ASME/Bath Symposium on Fluid Power and Motion Control.* Arlington, Virginia, USA.

Rasheed, H. (1998). Effect of surface waviness of the hydrodynamic lubrciation of a plain cylindrical sliding element bearing. *Wear, 223*, 1-6.

Renius, K. (1974). *Untersuchung zur reibung zwischen kolben und zylinder bei schägscheiben-axialkolbenmaschinen.* Dissertation VDI Verlag Düddrldorf, Germany.

Schenk, A. (2014). *Predicting the lubricating performance between the slipper and swashplate in axial piston machines.* Ph.D. Thesis, Purdue University.

Shang, L., & Ivantysynova, M. (2015). Port and case flow temperature prediction or axial piston machines. *International Journal of Fluid Power, 16*(1), 35-51.

Shang, L., & Ivantysynova, M. (2017). Thermodynamic analysis on compressible viscous flow and numerical modeling study on piston/cylinder interface in axial piston machine. *The 10th JFPS International Symposium on Fluid Power.* Fukuoka, Japan.

Shang, L., & Ivantysynova, M. (2018). Advances heat tansfer model for piston/cylinder interface. *The 11th International Fluid Power Conference, 11.IFK.* Aachen, Germany.

Shang, L. (2018). *A path toward an effective scaling approach for axial piston machine.* Ph.D. Thesis, Purdue University.

Shin, J. H., & Kim, K. W. (2014). Effect of surface non-flatness on the lubrication characteristics in the valve part of a swash-plate type axial piston pump. *Meccanica, 49*(5), 1275-1295.

Tiwari, S., Fadel, G., & Deb, K. (2011). AMGA2: improving the performance of the archive-based micro-genetic algorithm for multi-objective optimization. *Engineering Optimization, 43*(4), 377-401.

Wieczorek, U., & Ivatysynova, M. (2002). Computer aided optimization of bearing and sealing gaps in hydrostatic machines - the simulation tool CASPAR. *International Journal of Fluid Power, 3*(1), 7-20.

Yamaguchi, A. (1976). Motion of pistons in piston-type hydraulic machines. *Bulletin of JSME, 19*(130), 402-419.

Yamaguchi, A. (1990). Motion of the piston in piston pumps and motors: the case of metalic contact. *JSME International Journal, 33*(4), 627-633.

Zecchi, M. (2013). *A novel fluid structure interaction and thermal model to predict the cylinder block/valve plate interface performance in swash plate type axial piston machines.* PhD Thesis, Purdue University.

Zecchi, M., & Ivantysynova, M. (2012). An investigation of the impact of micro surface shaping on the cylinder block/valve plate interface performance through a novel thermo-elasto-hydrodynamic model. *The 7th FPNI PhD Symposium on Fluid Power.*

Zecchi, M., & Ivantysynova, M. (2012). Cylinder block/valve plate interface - a novel approach to predict thermal surface loads. *Proceedings of the 8th IFK.* Dresden, Germany.

Zecchi, M., & Ivatysynova, M. (n.d.). A novel fluid structure interaction model for the cylinder block / valve plate interface of axial piston machines. *Proceedings of the IFPE 2011.* Las Vegas, Nevada, USA.

VITA

Ashley Busquets (Wondergem) attended Saginaw Valley State University (SVSU) in Saginaw, MI for her BSME and graduated in August 2012. While enrolled at SVSU, she was employed as an undergraduate co-op engineer at Dow Chemical Company in Midland, MI from May 2010 until July 2012 with a fluid mixing group. In August of 2012, Ashley began her graduate research at Maha Fluid Power Research Center at Purdue University in the School of Mechanical Engineering under the supervision of Monika Ivantysynova. Her research focused on micro-surface shaping of the piston/cylinder interface of an axial piston machine utilizing an advanced modeling tool. Throughout her time at Purdue, Ashley was a member of the NSF funded Center of Compact and Efficient Fluid Power Engineering Research Center. In December of 2014, Ashley received her MSME with a thesis entitled “Piston/cylinder interface of axial piston machines – effect of piston micro-surface shaping.” After her Master’s she then transferred to the Department of Agricultural in Biological Engineering with a Fluid Power Specialization. Ashley will receive her Ph.D. in the spring of 2018 with a thesis entitled “An Investigation of Micro-Surface Shaping on the Piston/Cylinder Interface of Axial Piston Machines.”

PUBLICATIONS

Wondergem, A. and Ivantysynova, M. (2014). The impact of the surface shape of the piston on power losses. *Proceedings of the 8th FPNI Ph.D Symposium on Fluid Power*. Lappeenranta, Finland.

Wondergem, A. (2014). *Piston/cylinder interface of axial piston machines – effect of piston micro-surface shaping.* Masters Thesis, Purdue University.

Wondergem, A. and Ivantysynova, M. (2015). The imapct of micro-surface shaping on the piston/cylinder interface of swash plate type machines. *Preceedings of the ASME/Bath 2015 Symposium.* Chicago, IL, USA.

Wondergem, A. and Ivantysynova, M. 2015. The significance of piston/cylinder surface shaping on the performance of axial piston machines. *2015 Fluid Power Innovation & Research Conference.* Chicago, IL, USA.

Wondergem, A. and Ivantysynova, M. (2016). The impact of micro-surface shpaing of the piston on the piston/cylinder interface of an axial piston machine. *Preceedings of the 10th International Fluid Power Conference (10IFK).* Dresden, Germany.